UNIVERSITY OF SOUTHAMPTON

FACULTY OF ENGINEERING, SCIENCE AND MATHEMATICS

School of Chemistry

Tuneable Photonic Crystal Structures as Highly Reproducible Surface Enhanced Raman Spectroscopy (SERS) Substrates.

By

Suzanne Helen Pelfrey

Thesis for the degree of Doctor of Philosophy

Apr 2008

UNIVERSITY OF SOUTHAMPTON

ABSTRACT

FACULTY OF ENGINEERING, SCIENCE AND MATHEMATICS

School of Chemistry

Doctor of Philosophy

TUNEABLE PHOTONIC CRYSTAL STRUCTURES AS HIGHLY REPRODUCIBLE SURFACE ENHANCED RAMAN SPECTROSCOPY (SERS) SUBSTRATES.

By Suzanne Helen Pelfrey

SERS is a very useful analytical technique which was discovered over 30 years ago, however it has never fulfilled its potential due to inherently irreproducible surfaces used to enhance the Raman signals. If a robust and reliable surface was to be produced SERS could have applications in trace drug detection and catalytic reactions amongst others.

Gold nanostructured void surfaces have been produced which yield full control over the enhancement, simply by tuning the surface to the correct laser wavelength. It was discovered that SER signals varied depending on the void size and film thickness, and that a 350 nm void structure gave rise to enhancements in Raman signals of the order 10^8. and the 600 nm structures have a reproducibility of <10% variation, in terms of signal, across a surface. The theory as to why the structures give rise to a strong enhancement comes from the fully controllable plasmon modes within the structures, which are based on molecular orbital fields. The strongest SER signal arose when the laser light and outgoing Raman band were encompassed within a *P* type of plasmon mode. The underlying background in every SERS spectra was also attributed to photoluminescence (PL) from the gold surface, and an excellent correlation between the PL and surface plasmons was observed.

The detection of pyridine and carbon monoxide using in-situ electrochemical experiments have shown that the substrate has widened the (electrochemical) potential window for monitoring reactions, and show excellent promise as future chemical sensors.

TABLE OF CONTENTS

Chapter Six: Applications of sculpted SERS substrates. 130

Chapter Seven: Conclusions and Future Work 150

ACKNOWLEDGEMENTS

I would like to thank my supervisor Prof. Andrea Russell for all her help, advice and enthusiasm over the last few years, plus, I would never have got to do a PhD without her. My industrial supervisor at Renishaw Plc, Dr Ken Williams, along with: Matthew Bloomfield, Alan Brooker, Ian Hayward and Tim Smith for all their help and advice throughout my PhD, and to everyone else for making me feel welcome at Renishaw.

This whole project has been a collaboration between the schools of Chemistry and Physics, so I would also like to thank everyone who has been a part of it: Prof Jeremy Baumberg, Prof Phil Bartlett, Mamdouh Abdelsalam, Tim Kelf, Yoshi Suguwara, Robin Cole, and finally Sumeet Mahajan. The Friday afternoon meetings will certainly stick in my memory for years to come! I would also like to thank Alastair Clarke - who has made every gold slide I have used in this project.

Thanks must also go to the Russell Group members past and present: Colin, who I swear is the male version of me! Dai, who was a pleasure to know, and made ICAVS great fun. Dave – memories of your amazing dancing, and red pineapple inspired hair styles will always make me smile. Dr Fab, who, as his name suggests, is absolutely fabulous, and has been a great friend for the last two years. Gael 'Chocoman', my scrabulous friend – it's quite upsetting to be continually beaten by someone who's first language is French! Helen, who also lived in Lymington and made the commute much more fun. Jon – Speed by name speed by nature, possibly the fastest learning person I have ever met and I am very happy to be handing the SERS baton over to him. Katie, who basically turned her spare room over to me, and helped me through a very tough time in my life - I will always be grateful to you. Piotr, whose quirkiness will never be matched! Praba who is possibly the nicest person in the world, and I take this opportunity to wish her all the best in married life. Steve, who is a new member to the group but has been a pleasure to get to know. Thanks to you all for making the Russell group such a great place to work.

I would also like to thank my wonderful family for the unconditional love and support that they have provided over the past few years, Mum, Dad, Clare, Garry and Carol, I can't express my gratitude enough. Last, but by no means least, my boyfriend Peter who started out as a fellow Russell group member but has become one of the most important people in my life. I can't thank you enough for the help, support and encouragement you have given me over the last few months, and I couldn't have done it without you - you're allowed to read it now!

Chapter One: Introduction.

1 General Introduction.

Raman spectroscopy is a useful analytical technique, which has numerous advantages over other spectroscopic techniques such as Infrared (IR). Spectra can be acquired without destroying a sample, in-situ in a variety of environments, and unlike IR, from aqueous solutions. However Raman spectroscopy is an incredibly weak process, with only 1 in 10^{12} photons being Raman Scattered. There are two primary techniques that have been developed to increase the signal obtained from Raman spectroscopy, namely, Surface Enhanced Raman Spectroscopy (SERS) and Resonance Raman Spectroscopy (RRS).

SERS was discovered in Southampton in 1974 when Martin Fleischmann and co-workers recorded Raman spectra of pyridine which were a million fold more intense than expected [1]. The increase in intensity was due to the electrochemically roughened silver electrode that was used in this experiment. Originally it was thought that the enhancement came from the increased surface area of the electrode, however it was later established that the surface area could only account for a 10 fold increase in signal [2, 3]. Since this discovery SERS has undergone a massive amount of research, with over 4000 papers having been published in the last 30 years, with over half of these being published in the last decade.

The interest in SERS comes from the fact that it could be an incredibly useful analytical technique, with applications in health and safety, road side drug testing and many other areas. However there are only a handful of substrates that are commercially available, namely the general use SERS substrate Klarite that was, until recently, marketed by Mesophotonics, and Nanoplex who have utilised SERS to detect biomarkers in a commercial instrument. The reason for SERS not being used to its full potential, commercially, is due to the slight lack of reproducibility and robustness encountered with some substrates, as well as the cost of substrates to produce.

The resurgence in research in this area over the last decade has been primarily based around the development of new substrates, all of which move towards a more robust system. However, all substrates currently available have certain drawbacks.

This project has been mainly based on the development of a surface that meets the demands of a SERS substrate that could be used commercially. The key to the development was to fully understand the fundamental ideas mechanism of the SERS process at such surfaces. By bringing together information from other substrates that have been influential in SERS research it was also possible to take advantages from each and combine them together. These substrates will be discussed in detail in this chapter, and what advantages and disadvantages have been learnt from each.

2 Surface Enhanced Raman Spectroscopy.

SERS is a mechanism for enhancing the Raman Effect, which is covered in Chapter 2. When SERS was first discovered, Van Duyne and Schatz attributed the enhancement to the large polarisability when the Raman emitting system is taken to be a composite of the molecule and its conjugate charge in the metal. This model is known as the 'image field model' [4].

The image field theory compared the molecule to a point dipole, and the dipole, P, is imaged in the metal, and is given by:

$$P = \alpha_0 (E_0 + E_d)$$

Where

α_0 = polarisability of the free molecule

E_0 = The incident field due to the excitation

E_d = field at the molecule caused by its own image within the metal

This theory therefore put a strong dependence upon the distance between the molecule and the metal. When $R \leq 1.65$ Å, King *et al.* [5, 6] showed that enhancements of 10^6 were possible on a silver surface, however when R was more than 2 Å the enhancement dropped to 10^2. However the model ignored any molecular perturbations and also didn't apply to molecules that were close to, but not adsorbed on the metal surface. For any image theory to be correct the metal surface must be perfectly flat, and no explanation was fully given as to why rough surfaces enhanced signals to a greater extent than flat ones, and why the enhancement seemed to only come from certain metals. To this end the image field model has now been widely discredited and the majority opinion is that image field enhancement is not an important contributor to SERS.

More recently theoretical treatments have identified two effects that are widely accepted as the main contributors to the SERS enhancement. These are the chemical model and electromagnetic theory.

2.1 The Chemical Enhancement model

The chemical enhancement, or charge transfer, model mainly deals with mechanisms that are specifically related to interactions between the molecule and the metal. The model also includes the effects of the orientation and the coverage of the adsorbed molecules, metal surface structures and electrode potential are included.

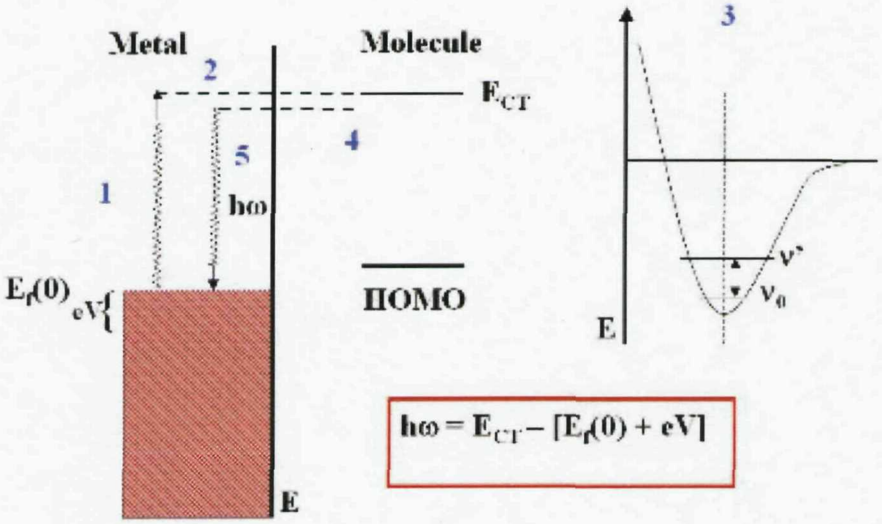

Figure 1 **Schematic diagram showing the chemical enhancement model that contributes to the SERS enhancement.**

A theory for the chemical transfer of energy has been proposed: a weak interaction between the substrate molecule and the metal surface exists, and the molecular energy level (E_{CT}) partially overlaps with the conduction band of the metal ($E_f(0)$). Therefore, a charge transfer can take place, this charge transfer gives the molecule more energy for the molecule to undergo Raman scattering. The chemical model predicts that the enhancement is more effective when the surface is rough, as the peaks in the film provide a route for the hot electrons to the adsorbed molecule. The intensity of the signal observed from the chemical enhancement model depends on the charge transfer state mechanism in action, and usually yields enhancements of around $10^2 – 10^4$.

2.1 The Electromagnetic (EM) Enhancement.

This model considers the change in the local electric field around the adsorbed molecule. Enhancement of the electromagnetic field at the metal surface is caused by the local electric field at the surface, which causes a strong polarisability of the molecule at the surface. A thorough review of the EM model has been written by Campion *et. al.* [7] One mechanism that accounts for the electromagnetic enhancement involves an overlap of the incident radiation wavelength, scattered radiation wavelength, and a surface plasmon resonance characteristic of the substrate.

The simplest definition of a surface plasmon is an oscillation of the free electrons at the surface of a metal at a certain frequency. On a metallic surface plasmons are created because the structuring of the metal causes standing electron waves across the surface when light a photon of light hits the surface. The plasmon cannot be emitted due to the metal surface beneath it so it is therefore reflected away from the surface in the form of coloured light. A more thorough review of surface plasmons and how they influence SERS will be given in Chapter 3.

The EM model has been comprehensively reviewed by Martin Moscovits [8], and it has been widely accepted as the more important contributor to the surface enhanced Raman signals, creating an enhancement around 10^{4}-10^{8}, depending on the substrate.

3 Common SERS Substrates.

SERS substrates have been an area of great interest over the last decade, with numerous groups over the world developing their own design of substrates. These can be grouped into three dominate types of surfaces: roughened, colloids and nanostructures. Each of these will be presented in detail in this section.

3.1 Roughened Surfaces.

SERS was first discovered using an electrochemically roughened silver electrode [1], produced using oxidation and reduction cycles (ORC), which displaces atoms at the surface and redeposit's them in an irregular manner. This technique yields a surface with a random arrangement of peaks and troughs. Figure 2 shows an SEM image of such an electrochemically roughened surface.

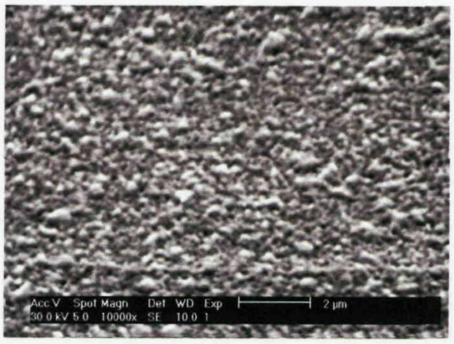

Figure 2 **Scanning Electron Microscope (SEM) image of a silver ORC SERS substrate**

This type of substrate was thought to enhance the Raman scattering due to the peaks on the surface acting as lightening rods. The peaks were thought to be tetrahedral in shape and an example of the peaks is given in Figure 3 [9].

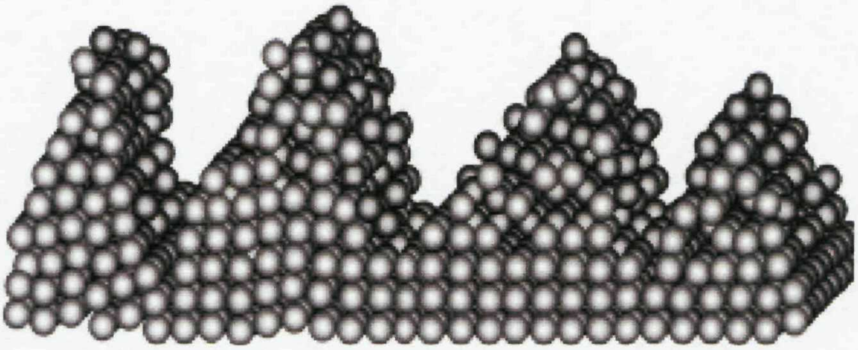

Figure 3 **A randomly rough surface produced through oxidation and reduction cycles [9].**

Tian and his research group have vastly improved the electrochemically roughened surfaces over the last 20 years, extending the technique to other transition metals. There are numerous papers published from his group expanding upon the technique for the production of rough surfaces, and the techniques are summarised in a review paper in the Journal of Physical Chemistry B [9].

There are other ways of producing an atomically rough surface, which have also been used to produce SERS substrate. Chemical etching is the most commonly used method other than the ORC surface. The overall surface morphology produced is very similar to that shown in Figure 2, however the surface of the metal is simply etched with acid. The combination of metal and acid that is used the most is silver with nitric acid.

The use of roughened SERS substrates has been hampered due to the lack of reproducibility in both the enhancement of signal obtained (the signal seen from the ORC substrate varies by up to 100% [10] from spot to spot) and the surface morphology. This has promted the SERS communnity to produce substrates that are more reliable and reproducible.

3.2 Colloids.

In 1983 work was done by Inoue and Ohtaka [11] on the clustering effects and sphere interactions upon SER signals. It was discovered that the maximum enhancement of the Raman intensity was $10^7 - 10^8$ when the distance between spheres was decreased. In this case the sphere cluster was 210 Å, and the maximum intensity was seen when the distance between the spheres was 1.2 Å. This early research into spherical clusters sparked a surge of interest into the area of colloids as SERS substrates. Over the course of the next decade many papers were published on the idea of colloid structures as SERS substrates [12-19], but it wasn't until the early 1990s that there was a resurgence of interest in this area of surface science.

In 1995 Michael Natan *et al.* published a paper in *Science* 'Self – Assembled Metal Colloid Monolayers: An approach to SERS substrates' [20]. This paper was a turning point within SERS research and for colloidal substrates. The substrate preparation was very simple and involved 2 steps: surface modifaction of a microscope slide with a polymer, and immersion into a colloidal Au or Ag solution. This yields spherical particles that are adhered strongly to the surface. The size (diameter) of colloidal particles can be varied, and solutions of different sized gold colloids are shown in Figure 4.

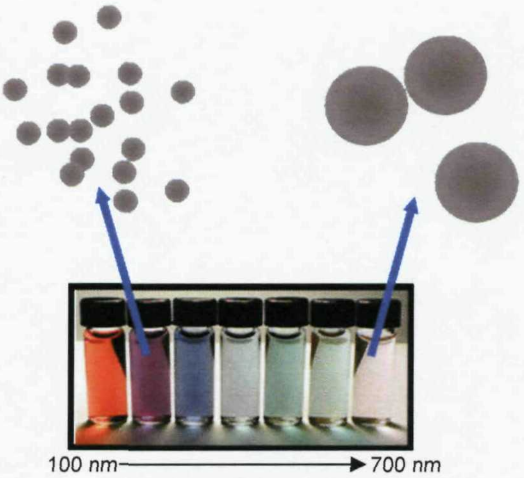

Figure 4 **Gold colloidal solutions, showing different colour solutions depending on the size of the colloid.**

Silver colloids have been used with great success over the last 10 years, including work done by Duncan Graham, Ewen Smith and colleagues involving colloids being attached to biological molecules, and used to enhance the Raman signals of the said molecules [21-23]. Katrin and Harald Kneip have also had great success using silver colloids as SERS substrates, and by tuning the size of the colloid to match the laser wavelength, as well as using Surface Enhanced Resonance Raman Spectroscopy (resonant with the adsorbed molecules), single molecules may be detected [24, 25].

The colloidal substrates have one major drawback: the particles tend to aggregate upon the addition of analytes, which results in variations of SERS intensity [26]. However they have been advanced by looking at producing gold colloids, with multiple layers of silver evaporated over the colloid [27]. This allows the distance between the colloids and the size to be varied to match the excitation wavelength of the laser, and has led the way into designing SERS substrates using nanotechnology.

3.3 Nanostructured Surfaces.

Due to the lack of reproducibility of other SERS substrates, nanotechnology has been used to produce highly reproducible substrates, many of which have been thoroughly discussed within the review paper by Vo-Dinh [28]. There are three groups who have produced the most used and succesful substrates in comparison to the one produced in this project: Van Duyne, Tian and the spin off company from the University of Southampton, Mesophotonics® (The Raman substrate of which was recently purchased by D3). The advantages and disadvantages of each of these surfaces will be discussed in detail and other substrates will also be mentioned.

Richard Van Duyne at Northwestern University has been at the forefront of SERS research since it's initial discovery. Since the late 1990s there have been two popular substrates produced in his group, the metal film over nanosphere (MFON) and the colloidal mask substrate.

3.3.1 Metal Film Over Nanosphere.

The development of the MFON structure was first reported in 1993, when Van Duyne's group developed a substrate based on a rough surface with a thick layer of Ag evaporated over the top. This was quickly developed to an Ag film over a polymer nanosphere [29].

The substrate has since been developed, they are prepared using 542 nm diameter latex spheres and evaporating a known amount of Ag over the top. The methodology improved over 8 years, leading to a surface which improved nanostructure stability and showed an improvement in the irreversible loss in signal [30] (this will be discussed in further detail in following chapters). A high resolution image of a MFON structure, taken from reference [30] is given in Figure 5.

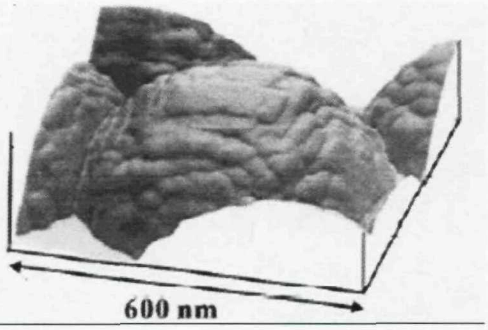

Figure 5 **Metal Film over Nanosphere (MFON) structure produced by Van Duyne. The structure consists of a 200 nm layer of silver evaporated over 542 nm ± 5 nm latex spheres, high resolution image taken from Reference 30.**

The substrate enhances Raman signals because the diameter of the colloid surface is on the same scale as the incident laser wavelength, 532 nm in this case, and the light excites plasmons on the structure, which have been shown to shift with metal thickness (Figure 7). These Raman signal is enhanced by a factor of 10^7.

This structure was one of the first substrates that was able to be produced in a reproducible manner, and showed excellent stability and reproducibility for electrochemical SERS experiments. It also extended the potential window for electrochemical experiments.

However, the substrate also has draw backs. Figure 5 shows that the surfaces are smooth in comparison to the ORC substrate, but they still have a very 'textured' appearance, which is not fully reproducible. The substrate also has a relatively short shelf life, as the silver will oxidise very quickly in air.

3.3.2 Colloidal crystal mask.

The second substrate developed by Van Duyne is also based on the colloid template, however for this substrate Ag is deposited in between the spheres forming the mask, leaving triangular regions of Ag [31], as shown in Figure 6.

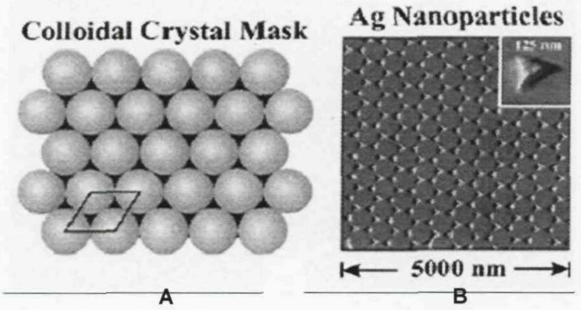

Figure 6 **Colloidal crystal mask template (A), with Ag deposited through the template (B). [31]**

The colloidal mask is produced by nanosphere lithography which is an inexpensive and highly productive way of making monolayer templates [32, 33].

The Ag is deposited through the mask using physical vapour deposition, and the mask is removed by dissolution in a solvent, which leaves a monolayer of evenly spaced, hexagonally arranged, nanoparticles. This method gives full control over the spacing and size of the nanoparticles, simply by altering the size of the original template and the thickness of metal deposited.

The enhancement obtained from this structure is of the order of 10^7 [34]. The regular arrangement of gold triangular structures give rise to controllable 'lightening rods', which were originally thought to give rise to the enhancements from the roughened surfaces.

The properties of both of the Van Duyne structures discussed have led to extensive work on the optical properties of SERS substrates. It has been discovered that the plasmon resonance associated with both structures can be tuned by adjusting the size of the original mask and the thickness of the Ag film deposited on/through the mask,

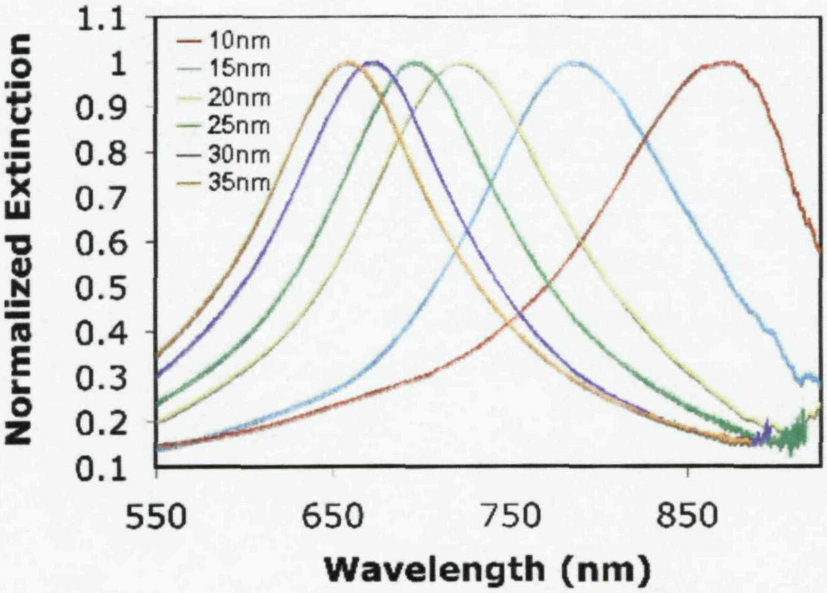

Figure 7 **Shifting localised plasmon resonance (LSPR) with increasing thickness of silver over the top of a 540 nm particle [35].**

The ability to shift the plasmon resonance through the visible region of light has produced the idea of tuning to laser wavelengths, as most lasers used for SERS are between 500 and 800 nm. An excellent review paper on this idea for the silver substrates produced by Van Duyne was published in 2005 [36].

The two substrates mentioned from Van Duyne have been seen as the 'bench mark' for SERS substrates due to the tunability and reproducibility of the production technique, and have been used as biosensors [36], and used for the detection of glucose amoungst other molecules [35]. However there are several substrates that are now competing with these surfaces.

3.3.3 Core-Shell Nanoparticles.

The development of the core shell nanoparticles as SERS substrates originated from of combination of coating roughened Au and Ag surfaces with a atomic layer of transition metal in order to 'borrow' the SERS from the coinage metals [REF] and the colloid structures discussed previously.

Tian *et al.* have been developing SERS substrates since the late 1980s, initially they were using electrochemically roughened surface, and however, in the late 1990s they expanded into nanoparticles. An excellent review paper has been published, citing the structures that have been developed from this group [9].

They have produced a substrate consisting of a Au nanoparticle core with a coating of Pd. A brief schematic is shown in Figure 8.

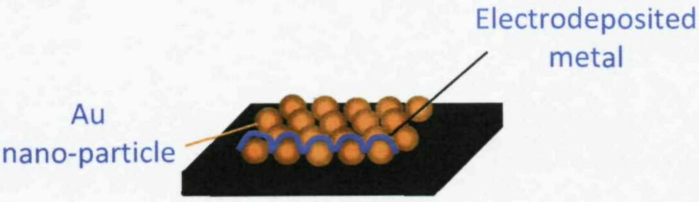

Figure 8 **Schematic showing a representation of the Au – Core shell nanoparticle SERS substrate.**

This substrate allows SERS to be detected from the historically 'non-SERS' active metals by using the enhanced electric field from the gold nanoparticle beneath the thin surface of the transition metal. Work on these substrates has progressed rapidly into pure platinum and palladium nanocubes [37]. However, the way that the nanoparticles are assembled onto an electrode for each experiment means that the substrate varies each time, and therefore the enhancement factors will also vary.

3.3.4 Anisotropically etched Si based Au structures (Mesophotonics/D3)

This substrate consisits of a base made from a silicon wafer, into which inverted pyramidal pits in the surface have been created using anisotropic etching. The substrate is then covered in ~ 80 nm of gold. Figure 9 shows an SEM image and a computer generated image of the substrate.

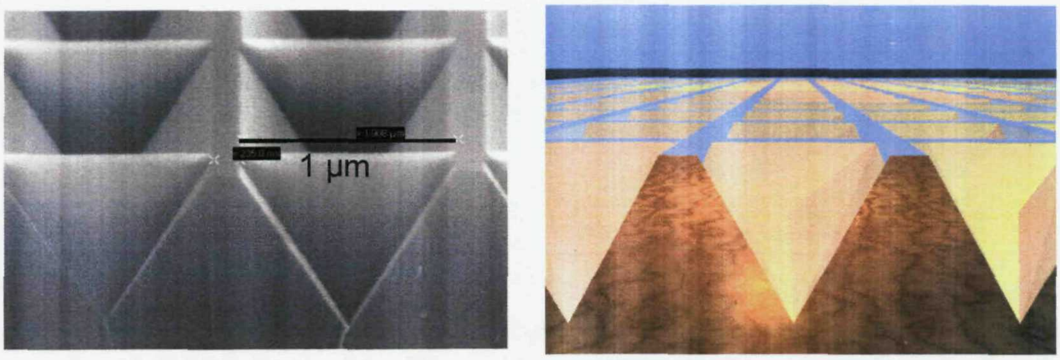

Figure 9 **SEM image and a computer generated image of the Klarite® SERS substrate. Image provided by Mesophotonics.**

The substrate is commonly known as Klarite and it was developed at the Department of Physics, University of Southampton and was commercially produced by the spin off company Mesophotonics. (The technology has now been bought by D3; a company associated with The University of Strathclyde).

Klarite works by trapping light within the pits of the substrate, acting as a photonic crystal. The details Surface Plasmon Polaritons (SPP's) will be discussed in much greater depth in Chapter 3. However, briefly, the idea behind this substrate is to produce a standing wave of light (SPP) within the cavity, which will enhance the Raman scattering of any molecules within the pit. The substrate is very easily manufactured, and the surface structure is highly reproducible due to the preparation procedure. At the point of writing the thesis, there was no information available on the enhancement factors obtained from the surface. Klarite^{TM} is primarily a photonic crystal, which is a crystal structure of size similar to that as the wavelength of light, and there are other substrates that also fall into this category of substrate.

3.3.5 Photonic Crystals.

Nanostructured surfaces tend to focus on photonic crystal structures, using colloidal templates. This type was structure was first published by Imhof and Pine in 1997 [38], however Velev [39] and Braun and Wiltzius [40, 41] also published very similar work shortly afterwards.

The structures are made by assembling a colloidal crystal template, which is then filled with metal (using various different methods), and the the template is then removed, leaving a void in it's place, Figure 10 shows a general schematic.

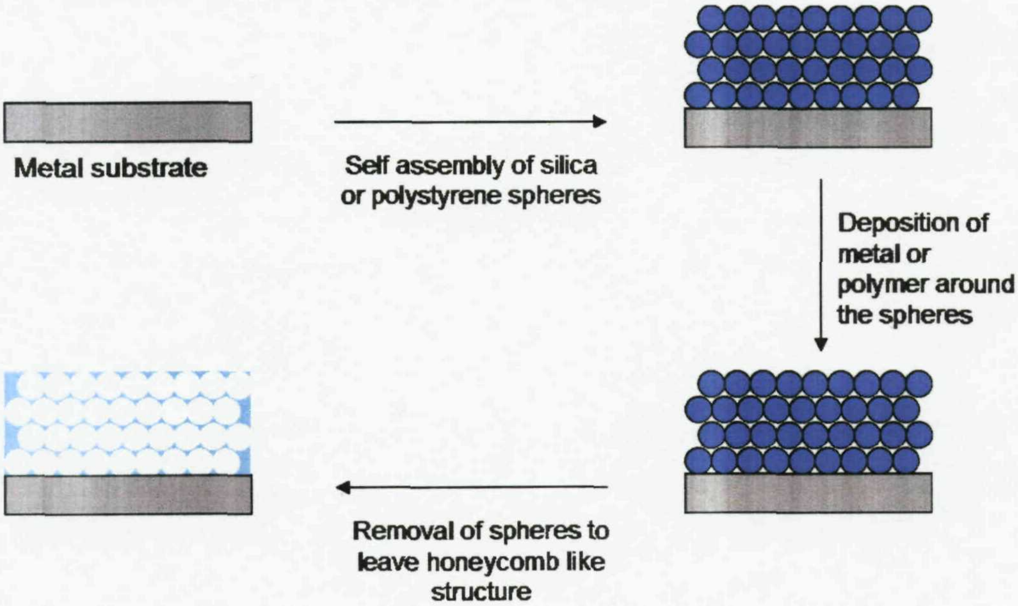

Figure 10 **General diagram showing the process for producing inverse opal photonic crystal structures, using a sphere template (dark blue spheres).**

The original structure made by Imhof and Pine [38] was made in a different manner to that used for the majority of structures made today. They used an emulsion templating procedure, which used an oil-in-formaldehyde emulsion, where the oil droplets acted as the template. The metal surrounded the droplets by the preparation of a metal oxide sol, which was mixed with formamide. The oil containing emulsion was then dispersed into the metal sol, and the droplet size was controlled by centrifugation. Finally the gel was dried and calcinated, leaving the inverse structure. Their method was quite successful and the film looked well ordered, however the technique yielded templates that were irreproducible and lacked absolute control over the pore size.

In contrast, Braun and Wilzius used CdS and CdSe to deposit around polystyrene spheres of 466 nm [40] The spheres were assembled on an indium tin oxide electrode. However their technique for the production of the template uses a sedimentation technique, which produces a multilayer polycrystalline material. These tend to have numerous defects e.g. stacking faults, cracking and grain boundaries.

A SERS substrate was developed using this template method by Tessier and Velev *et. al.* [42], which had a enhancement factor of 10^4. However the substrate lacked reproducibility in surface morphology – the area between the original template was filled with 25 nm gold nanoparticles, leading to a rough surface.

More recently there have been advances in templating techniques, for example templates can be produced with a monolayer of spheres, and with regular defects [43] and bands [44]. Our group now prepares templates with monolayer coverage and voids are filled using electrodeposition. The main benefits of this technique over methods such as spin coating [45] or electroless deposition [46] are:

1. Production of a high density material between the voids. The material is deposited in the voids between the spheres as opposed to around the surface of the spheres. This, in turn, means that there will be little or no shrinkage when the spheres are removed.
2. Electrodeposition can be used to prepare a wide range of materials. Both aqueous and non-aqueous solutions can be utilised.
3. Electrodeposition allows control over film thickness, by control of the total charge passed in the cell.

4. The film produced is very smooth, with typical roughness factors that may be fully accounted for by the nanostructure imposed by the spheres.

4 Sculpted SERS Substrates.

The substrate that is presented in this thesis has been developed over the course of 7 years. Mohamed Ghanem and Phil Bartlett originally produced platinum, palladium and cobalt films using metal salt solutions to deposit through a template of submicron polystyrene particles [47]. The structures produced consisted of multilayers of polystyrene spheres, however it paved the way for macroporous conducting polymers (polypyrrole, polyaniline and polybithiophene) structures to be produced, using the same principle [48].

It was realised that these cavity structures had many applications due to the structure's magnetic [49] and optical properties [50-52]. Therefore work was carried out on: optimising the preparation of the templates, to ensure monolayers were produced [51], development of structures of varying morphology i.e. isolated cavities [53] and nanodots [54], and metallic composition [55, 56].

The structure has been developed throughout this project to produce a SERS substrate and the full preparation procedure of these substrates is given in Chapter 2, however a brief schematic is given below in Figure 11.

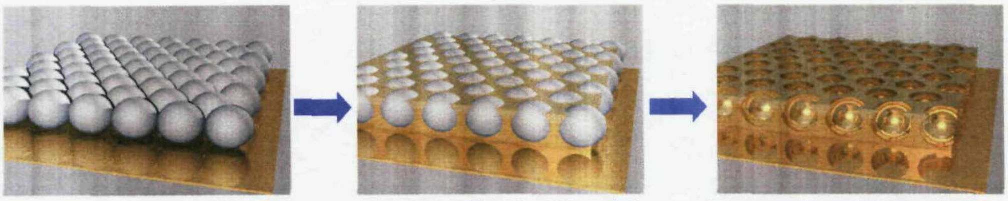

Self assembly of polystyrene spheres from an aqueous solution onto a hydrophilic gold slide.

Electrodeposition of gold through the template.

Polystyrene spheres dissolved in Tetra hydrofuran leaving a smooth surface.

Figure 11 **Diagram showing the three key stages in the preparation of a sculpted SERS substrate.**

The work presented throughout this thesis will show how an improved SERS substrate has been made in terms of: surface smoothness, enhancement factors, reproducibility, robustness, shelf life and the overall understanding of the mechanisms causing the enhancements.

5 Thesis Plan

The techniques, equipment and methods used to develop, prepare and measure the sculpted substrates are presented in *Chapter 2.* An in depth discussion of the principles of surface plasmon polaritons required to fully explain these substrates is provided in *Chapter 3.* Along with the theoretical plasmon modes associated with the structure.

Chapter 4 gives a more indepth look at the structure and the plasmonics and how this relates to the SER signal from different surface morphologies and laser wavelengths. The surfaces were varied by changing the void size and film thickness, and three different laser wavelengths were chosen to see how the signal varies.

The development of silver SERS structures and comparison to a Van Duyne MFON style structure in terms of shelf life and enhancements is given in *Chapter 5.* The background observed on every SERS substrate has rarely been discussed in SERS research, and an overview of how it changes with laser wavelength is also given in Chapter 5.

Chapter 6 discusses the applications of this substrate, and finally, conclusions and suggestions of further work are presented in *Chapter 7.*

6 References

1. Fleischmann, M., P.J. Hendra, and A.J. McQuillan. Chem. Phys. Lett., 1974. **26**(2): p. 163-166.
2. Albrecht, M.G. and J.A. Creighton. J. Am. Chem. Soc., 1977. **99**(15): p. 5215-5217.
3. Jeanmaire, D.L. and R.P. Vanduyne. J. Electroanal. Chem., 1977. **84**(1): p. 1-20.
4. Schatz, G.C. and R.P. Vanduyne. Surf. Sci., 1980. **101**(1-3): p. 425-438.
5. King, F.W. and G.C. Schatz. Chem. Phys., 1979. **38**(2): p. 245-256.
6. King, F.W., R.P. Vanduyne, and G.C. Schatz. J. Chem. Phys., 1978. **69**(10): p. 4472-4481.
7. Campion, A. and P. Kambhampati. Chemical Society Reviews, 1998. **27**(4): p. 241-250.
8. Moskovits, M. Rev. Mod. Phys., 1985. **57**: p. 783.
9. Tian, Z., B. Ren, and D. Wu. J. Phys. Chem. B, 2002. **106**(37): p. 9463.
10. Cintra, S., M.E. Abdelsalam, P.N. Bartlett, J. Baumberg, T. Kelf, and A.E. Russell. Faraday Discuss., 2005. **132**: p. 91.
11. Inoue, M. and K. Ohtaka. J. Phys. Soc. Jap, 1983. **52**(11): p. 3853.
12. Pettinger, B., X. Bao, I.C. Wilcock, and G. Muhler. Phys. Rev. Lett., 1994. **72**: p. 1561.
13. Van Duyne, R.P., J.C. Hulteen, and D.A. Treichel. J. Chem. Phys., 1993. **99**: p. 2101.
14. Roark, S.E. and K.L. Rowlen. Chem. Phys. Lett., 1993. **212**: p. 50.
15. Schueler, P.A. Anal. Chem., 1993. **65**(3177).
16. Dawson, P., J.W. Haas III, K.B. Alexander, J. Thompson, and T.L. Ferrell. Surf. Sci. Lett., 1991. **250**: p. L383.
17. Byahut, R. and T.E. Furtak. Langmuir, 1991. **7**: p. 508.
18. Moody, R.L., T. Vo-Dinh, and W.H. Fletcher. Appl. Spectrosc., 1987. **41**: p. 966.
19. Carron, K.T., W. Fluhr, M. Meier, A. Wokaun, and H.W. Lehmann. J. Opt. Soc. Am. B, 1986. **3**: p. 430.

20. Griffith Freeman, R., K.C. Grabar, K.J. Allison, R.M. Bright, J.A. Davis, A.P. Guthrie, M.B. Hommer, M.J. Jackson, P.C. Smith, D.G. Walter, and M.J. Natan. Science, 1995. **267**(1629).
21. Faulds, K., R.E. Littleford, D. Graham, G. Dent, and W.E. Smith. Anal. Chem., 2004. **76**: p. 592.
22. Faulds, K., L. Fruk, D.C. Robson, D.G. Thompson, A. Enright, E. Smith, and D. Graham. Faraday Discuss., 2005. **132**(20).
23. Cunningham, D., R.E. Littleford, E. Smith, P.J. Lundahl, I. Khan, W. McComb, D. Graham, and N. Laforest. Faraday Discuss., 2005. **132**(12).
24. Kneipp, K., Y. Wang, H. Kneipp, I. Itzkan, L.T. Perelman, R.R. Dasari, and M.S. Feld. Phys. Rev. Lett., 1997. **78**(1667).
25. Kneipp, K., H. Kneipp, R. Manoharan, I. Itzkan, R.R. Dasari, and M.S. Feld. Bioimaging, 1998. **6**: p. 104.
26. Schueler, P.A., J.T. Ives, F. DelaCroix, W.B. Lacy, P.A. Becker, J. Li, K.D. Caldwell, B. Drake, and J.M. Harris. Anal. Chem., 1993. **65**: p. 3177.
27. Mulvaney, S.P., L. He, M.J. Natan, and C.D. Keating. J. Raman. Spectrosc., 2003. **34**: p. 163.
28. Vo-Dinh, T. TrAC, 1998. **17**(8-9): p. 557.
29. Van Duyne, R.P., J.C. Hulteen, and D.A. Treichel. J. Chem. Phys., 1993. **99**(3): p. 2101.
30. Dick, L.A., A.D. McFarland, C.L. Haynes, and R.P. Van Duyne. J. Phys. Chem. B, 2002. **106**: p. 853.
31. Hulteen, J.C., D.A. Treichel, M.T. Smith, M.L. Duval, T.R. Jenson, and R.P. Van Duyne. J. Phys. Chem. B, 1999. **103**: p. 3854.
32. Joannopoulos, J.D. Nature, 2001. **414**: p. 257.
33. Kralchevsky, P.A. and N.D. Denkov. Current Opinion in Colloid & Interface Science, 2001. **6**(4): p. 383-401.
34. http://chemgroups.northwestern.edu/vanduyne/research_overview.htm, title.
35. Van Duyne, R.P. Faraday Discuss., 2005. **132**: p. 1.
36. Haes, A.J., C.L. Haynes, A.D. McFarland, G.C. Schatz, R.P. Van Duyne, and S. Zou. MRS Bulletin, 2005. **30**: p. 368.

37. Tian, Z., Z.L. Yang, B. Ren, J. Li, Y. Zhang, X.F. Lin, J. Hu, and D. Wu. Faraday Discuss., 2005. **132**(13).

38. Imhof, A. and D.J. Pine. Nature, 1997. **389**: p. 948.

39. Velev, O.D., P.M. Tessier, A.M. Lenhoff, and E.W. Kaler. Nature, 1999. **401**: p. 548.

40. Braun, P.V. and P. Wiltzius. Nature, 1999. **402**: p. 603.

41. Braun, P.V. and P. Wiltzius. Current Opinion in Colloid & Interface Science, 2002. **7**: p. 116.

42. Tessier, P.M., K.K. Ong, S.D. Christesen, A.M. Lenhoff, E.W. Kaler, and O.D. Velev. Vibrational Spectroscopy-Based Sensor Systems, 2002. **4577**: p. 53-64.

43. Sanchez - Gil, J.A. and J.V. Garcia - Ramos. Chem. Phys. Lett., 2003. **367**: p. 361-366.

44. Palacios-Lidon, E., J.F. Galisteo-Lopez, B.H. Juarez, and C. Lopez. Adv. Mater., 2004. **16**(4): p. 341 - 345.

45. Hu, J., Y. Zhang, J. Li, Z. Liu, B. Ren, S. Sun, Z. Tian, and T. Lian. Chem. Phys. Lett, 2005. **408**: p. 354.

46. He, H.X., H. Zhang, Q.G. Li, T. Zhu, S.F.Y. Li, and Z.F. Liu. Langmuir, 2000. **16**(8): p. 3846 - 3851.

47. Bartlett, P.N., P.R. Birkin, and M.A. Ghanem. Chem. Commun., 2000: p. 1671.

48. Bartlett, P.N., P.R. Birkin, M.A. Ghanem, and C.S. Toh. J. Mater. Chem., 2001. **11**: p. 849.

49. Bartlett, P.N., M.A. Ghanem, I.S. El Hallag, P. de Groot, and A. Zhukov. J. Mater. Chem., 2003. **13**: p. 2596.

50. Coyle, S., M.C. Netti, J.J. Baumberg, M.A. Ghanem, P.R. Birkin, P.N. Bartlett, and D.M. Whittaker. Phys. Rev. Lett., 2001. **87**(17): p. 176801.

51. Bartlett, P.N., J.J. Baumberg, S. Coyle, and M.E. Abdelsalam. Faraday Discuss., 2004. **125**: p. 117.

52. Prakash, V.G., L. Besombes, T. Kelf, J.J. Baumberg, P.N. Bartlett, and M.E. Abdelsalam. Opt. Lett., 2004. **29**(13): p. 1500.

53. Abdelsalam, M.E., P.N. Bartlett, J.J. Baumberg, and S. Coyle. Adv. Mater., 2004. **16**(1): p. 90.

54. Ghanem, M.A., P.N. Bartlett, P. De Groot, and A. Zhukov. Electrochem. Comm., 2004. **6**: p. 447.

55. Bartlett, P.N., J.J. Baumberg, P.R. Birkin, M.A. Ghanem, and M.C. Netti. Chem. Mater, 2002. **14**: p. 2199.

56. Bartlett, P.N., T. Dunford, and M.A. Ghanem. J. Mater. Chem., 2002. **12**: p. 3130.

Chapter Two Experimental Methods and Techniques

Detailed information regarding the theoretical and practical aspects of the experimental work undertaken in this project is presented in this chapter. This includes descriptions of: nanostructure preparation, Raman spectroscopy, electrochemical methods, optical and scanning electron microscopy.

1 Reagents and Materials.

The materials and reagents used within this study, along with their suppliers, are detailed below in Table 1.

Table 1 List of the reagents / materials used and their suppliers.

Reagent/Material	**Supplier**
Potassium Chloride (KCl)	BDH Laboratory Supplies
Potassium hydroxide (KOH)	BDH Laboratory Supplies
Pyridine (Py)	BDH Laboratory Supplies
Propan-2-ol	Sigma Aldrich
1 wt% aqueous solution polystyrene spheres (various sizes)	Duke Scientific
Cysteamine	Sigma Aldrich
Dimethyl formaide (DMF)	Sigma Aldrich
Benzenethiol (BT)	Sigma Aldrich
Ethanol HPLC grade	Fisher Scientific
Commercial gold plating bath (Cyanide free)	Metalor, Technic Inc.
Commercial silver plating bath	Metalor, Technic Inc.
Platinum plating bath: Hyrdogen hexachloroplatinate(IV) hydrate	Sigma Aldrich
Concentrated sulphuric acid (98%)	Fisher
Carbon Monoxide (CO)	BOC Gases

Argon	BOC Gases
Sodium Dodecyl Sulfate (SDS)	Fisher

2 Preparation of SERS substrates.

SERS substrates have typically been prepared by electrochemically roughening electrodes since the discovery of SERS in 1974[1] leading to an irregular surface structure made of peaks and troughs. However in the 3 decades since this discovery, many different substrates have been prepared, silver colloid structures [2-8] being the most used, due to the relative ease of preparation and good enhancements of signal. Nanostructured substrates have been coming to the forefront of SERS research since the mid 1990s with Van Duyne's 'Metal Film Over Nanostructure (MFON)' and the silver island structure [9-13]. Tian *et al*, have also developed many substrates, primarily using transition metals [6, 13-17], both of which have improved the reproducibility of SERS substrates.

The nanovoid substrate presented within this thesis has been developed over the past 6 years [18-24] at the University of Southampton, and there are several important stages that lead to the production of this smooth and robust SERS substrate. Surface modification, self assembly and electrodeposition will be discussed in the following section.

2.1 Surface Modification and Self Assembly.

In order to explain the surface modification techniques used to assemble polystyrene spheres in this project, the ideas of surface wetting, contact angles and self assembly must first be introduced.

Self assembley has been described as 'self aggregation of particles into an organised structure without external assistance' [25] and there have been many landmarks in it's understanding, including the discovery of the structure of Deoxyribose Nucleic Acid (DNA) and the development of microscale self assembly using surface tension [26]. Since this discovery self assembled structures have drawn interest from a wide variety of research fields.

Self assembly of particles using surface tension and capillary forces is of particular interest in this project. In particular Kralchevsky and Denkov [27] have published an excellent review on the theory of lateral capillary forces involved in the production of these structures. A capillary tube is the most obvious example of a capillary force; which can occur between particles, due to an overlap of menisci formed around each separate particle. Liquid forms a bridge between them, which can either be attractive or repulsive depending on contact angle between the particles and the solution. Attractive forces such as these give rise to aggregation of the particles and lead to the formation of a hexagonal close packed structure.

An example of regular arrays of latex particles produced by evaporation of suspensions are the substrates produced for the study of optical properties [28], which form multilayer's of particles which act in a similar way to an opal. However, the control over acquiring a single monolayer did not come until the 1990's with the first instance being when Velev *et al.* produced a 2D opal structure [29]. The control over the assembly arises from surface modification, and reducing the contact angle between the solution and the surface.

The contact angle depends on the properties of the solid and the liquid and if the angle is $0 < \theta < 90°$ then the surface is said be wet, and if the angle is between $90° < \theta < 180°$, then the surface is said to be non wetting. This is an important factor it terms of self assembly from aqueous solutions.

When a solution of particles, held in an aqueous solution, comes into contact with a surface the angle at which the liquid touches the surface has a profound effect on how the particles arrange themselves. As Figure 1 shows, if the contact angle is greater than 90° then the particles are able to form multiple layers upon the surface. However if the angle is below 90° the particles spread out and monolayer formation is more likely.

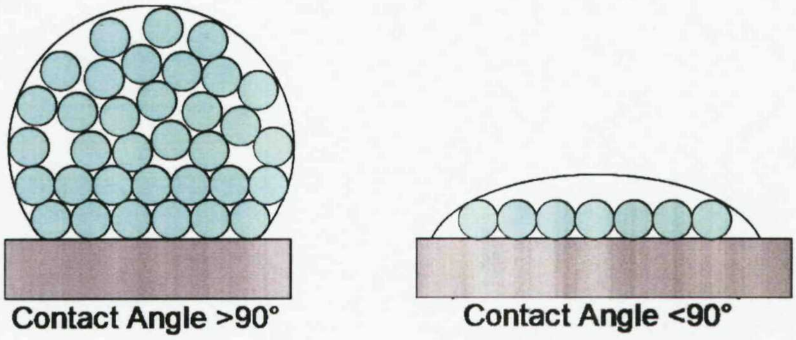

Figure 1 **Drops of solution containing particles, on a surface with contact angles greater and less than 90°.**

It is this technique that has been developed at the University of Southampton to create monolayers of polystyrene spheres, which are used as templates for the sculpted SERS substrates. The experimental procedure will now be explained in full.

2.1.1 Slide preparation

Gold slides were prepared in-house by evaporating a 20 nm layer of chromium onto a glass microscope slide, as the gold does not adhere straight onto the glass, followed by a 200 nm layer of gold. The slide was then cut into eight pieces using a diamond glass cutter. Each piece was cleaned by sonication in deionised water for 30 minutes followed by isopropanol for 90 minutes. Each slide was then placed into a 10 mM solution of an ethanolic solution of cysteamine.

The slides were left in the cysteamine for a minimum of three days to form a self assembled monolayer (SAM), for two reasons: Firstly, the contact angle between the gold surface and the aqueous solution decreases from 93° to 35° making the surface wet. Secondly, the molecule is a short alkane chain that ends with an amine group. The amine group becomes protonated in aqueous solution, which leads to the surface of the gold having an overall positive charge. The positive charge is important because the polystyrene spheres (used directly from the bottle) used as a template are polarised easily to a negative charge; therefore an electrostatic interaction occurs between the spheres and the gold surface, which aids the self assembly process.

A thin layer cell has been developed within this project which allows these techniques to come together in a practical way. The cell is comprised of a gold slide with a cysteamine SAM assembled onto it, a thin layer of parafilm and a glass cover slip. As shown in Figure 2.

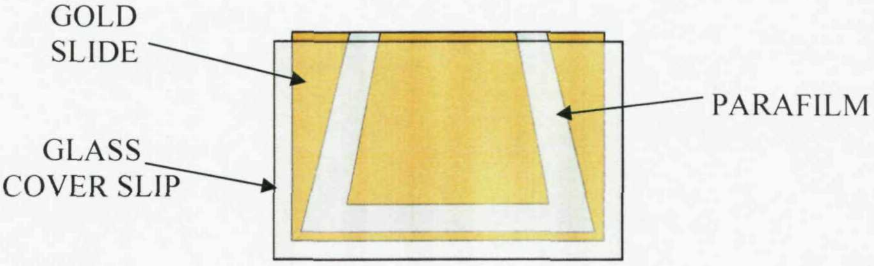

Figure 2 **Schematic diagram showing the components of a thin layer cell.**

The parafilm is cut into a tetrahedral shape to force the spheres together as the solution evaporates. The glass cover slip is used untreated, and is hydrophobic and as such repels the solution and forces it onto the gold. The distance between the glass and gold slides is ~100 μm.

The thin layer cell was filled with a solution of 1 wt% polystyrene spheres, used directly from the bottle, using an autopipette set to 5 μl. Once the cell was filled with the desired size of sphere (350 nm up to 1000 nm), it was placed into a petri dish and the open end of the cell was raised by placing it onto a flat microscope slide. The dish including the cell was placed into an incubator (LMS 305), and left overnight at 20 °C. Figure 3 shows how the polystyrene spheres assemble onto the top of a gold surface, using evaporation and surface modification techniques.

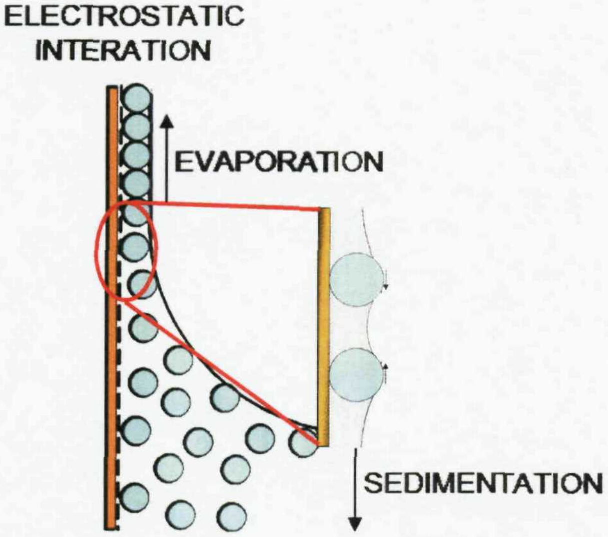

Figure 3 **Schematic diagram showing how polystyrene spheres assemble on a modified gold slide.**

When the aqueous solution evaporated out of the cell, a monolayer of spheres remained. The progress of evaporation can be monitored through the clear glass cover slip of the thin layer cell. This monolayer acts as a template for electrodeposition. Figure 4 shows an SEM image of a monolayer of spheres.

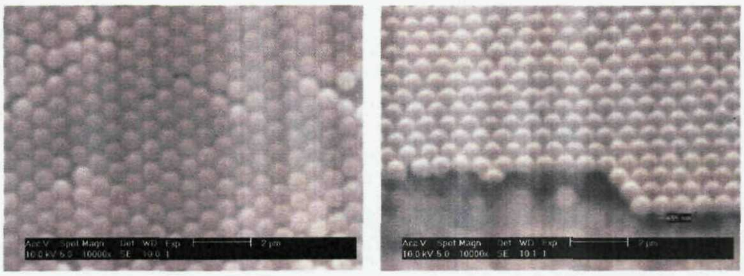

Figure 4 **SEM images of a monolayer of 600 nm polystyrene spheres which had been sputter coated in gold to make them conducting.**

There are two substrates that have been prepared in this project using the polystyrene spheres as a template. One is the nanovoid structure that is the predominant structure in this thesis. However a second structure has been prepared which is the inverse of this, involving evaporating metal over the top of the spheres. The preparation of the nanovoid structure will be presented in the next section (2.2), followed by the inverse structure in section 2.3.

2.2 Electrodeposition.

2.2.1 Chronoamperometry

The reaction shown in equation 1 is an example of a simple electrode reaction, where O is oxidised/reduced at the electrode surface, this is the simplest example of a reaction that can be controlled by chronoamperometry.

$$O^+ + e^- \leftrightarrows R \tag{1}$$

Chronoamperometry (CA), involves an instantaneous change in potential from E_1, where no reduction of O occurs to E_2, at time 0, where the reduction of O occurs at a diffusion controlled rate. The potential waveform is shown in Figure 5.

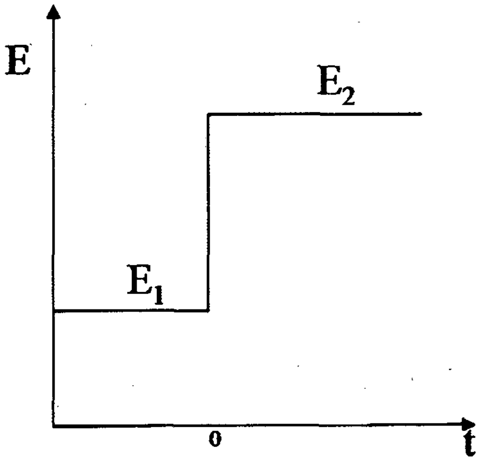

Figure 5 **Potential wave form for chronoamperometry.**

During time (t) the change in current occurring during the reaction can easily be monitored, for a simple diffusion controlled example such as equation 1. Using the Cottrell equation (2):

$$|i| = \frac{nFD^{1/2}c_o^{\infty}}{\pi^{1/2}t^{1/2}} \tag{2}$$

Where *i* is the current density, n is the number of electrons involved in the overall electrode reaction, F is the Faraday constant, *D* is the diffusion coefficient, c_o^∞ is the concentration of the bulk solution and *t* is time. It can be derived that, the current falls at $t^{-1/2}$. However this is a very simple example and is not the case for all reactions.

When the product or reactants are not soluble in solution, e.g. metal deposition, the current time transients are very different, and often contain a rising portion, which is a clear indication of a nucleation step, i.e. the formation of a species on the electrode surface. In this case the current time transients are usually presented as a function of *i* vs. t^n, where n depends on the type of nucleation involved, the geometry of phase growth and the rds in phase formation. There are three key transients in the different phase formation processes, as shown in Figure 6.

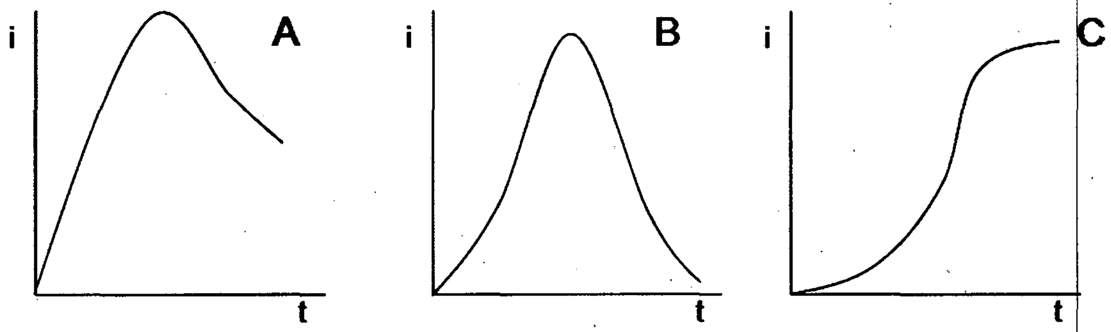

Figure 6 **Schematic diagrams of i-t transients for various types of phase formation processes. (A) monolayer formation with instantaneous nucleation; (B) monolayer formation with progressive nucleation and (C) three dimensional nucleation and growth process. [30]**

These three transients can also be seen to be combined when depositing a thick layer of metal. The *i–t* transient shown in Figure 7, shows clearly these three stages of metal growth, as labelled A, B and C.

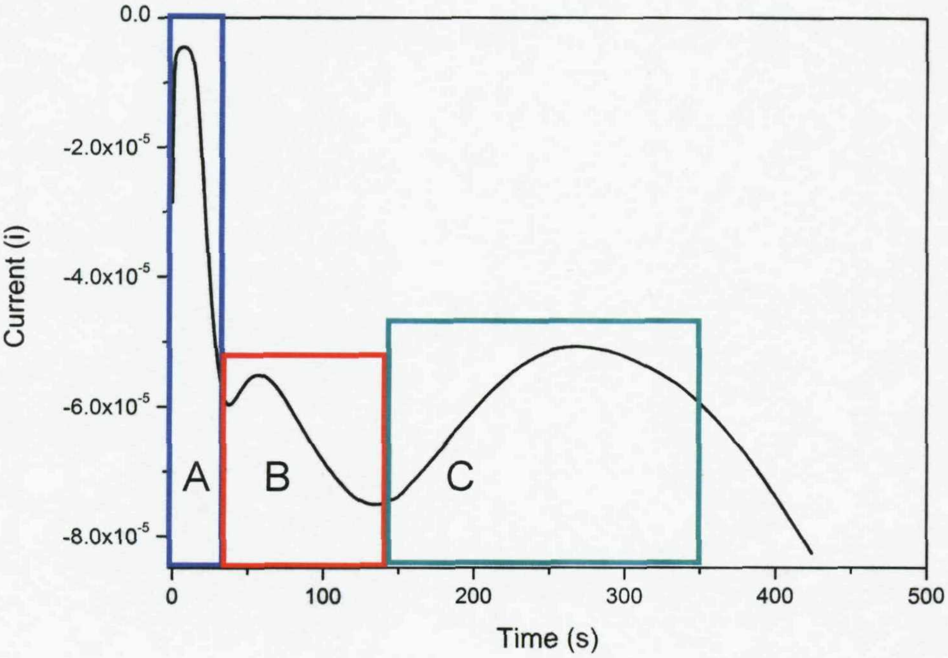

Figure 7 **Current – Time plot showing the electrodeposition of gold through a 600 nm polystyrene sphere template.**

The curve shown in Figure 7 shows gold being deposited through a polystyrene sphere template, and therefore the region between B and C can also be explained in terms of the change in surface area exposed between the spheres as the film deposition progresses. As the film thickness increases, the area between the sphere template decreases until a point where they touch, at this point the current reaches a maximum (shown in region C). As the area, available for deposition, between the spheres increases again, the current decreases. Further work done by Szamocki *et al* [31] has shown that current – time plots can be used to control the deposition through multilayer templates to a very accurate level.

Using the current time plot, the area under the curve can be integrated at the point where the spheres touched in the template (the maxima in region C), and the film thickness can be measured using the pore mouth diameter in the SEM to confirm that the film is ½ *d* (the film thickness divided by the sphere diameter). From this a calibration number can be calculated to allow deposition to other film thickness simply by using this ratio factor.

During the course of this project three different metals were electrodeposited through the polystyrene template. Full control over the film thickness comes from monitoring the potential as a function of time.

The potentials chosen for depositing metals through the templates are listed in Table 2.

Table 2 **Electrodeposition potentials, and solutions for each metal.**

Metal	Plating Solution	Deposition Potential /V	Calibration 1 C/cm^2 equals film thickness	Plating Solution Efficiency
Au	Metalor gold plating solution 5 ml brightener per 1 litre plating solution	*Au on Au* = -0.7 *Au on Ni* = -0.75 (vs. SCE)	2 µm	100%
Ag	Metalor silver plating solution	*Ag on Au* = -0.125 *Ag on Ni* = -0.21 (vs. MMSE)	2.2 µm	100%
Pt	50 mM H_2PtCl_6 & 0.5 M SDS	*Pt on Au =0.05V* *(vs. SCE)*	0.4 µm	100%

Chronoamperometry was primarily used for Electrodeposition, however it was also used during spectroelectrochemical experiments, explained later in the chapter. Electrodeposition of metals was carried out using a standard three electrode cell, controlled by an Autolab PGSTAT20 potentiostat. The three electrodes were as follows:

Working Electrode.

The gold slide was used as the working electrode. The area of the slide where deposition of gold was not required, i.e. the non templated area, was made non conductive by using nail varnish, as shown in figure 8.

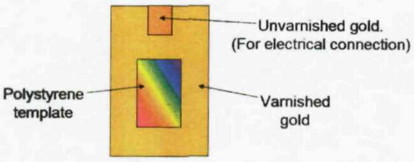

Figure 8 **Diagram showing a prepared working electrode.**

The area of the templated region was measured, and the dimensions were used to aid the control over the amount of metal that was deposited, as explained further below.

Counter electrode.

The counter electrode was 1 cm^2 platinum gauze. The area of the counter electrode was kept in proportion to the working electrode.

Reference electrode.

The reference electrode used in the cell was a home made saturated calomel electrode, as shown in Figure 9. The calomel electrode was chosen as the reference electrode, as it is one of the most stable reference electrodes, and is easily prepared.

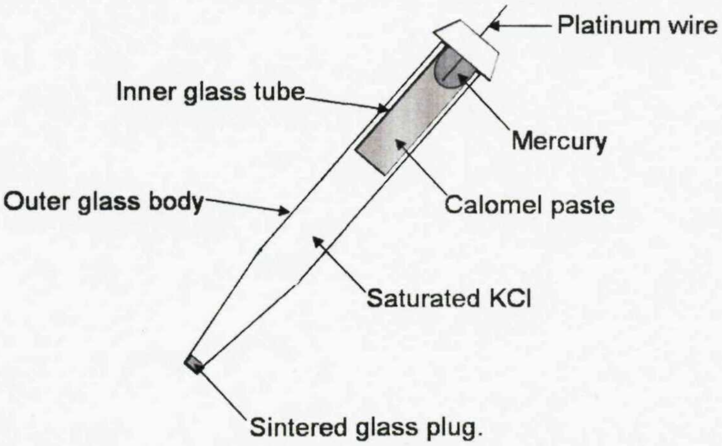

Figure 9 **Diagram depicting the completed homemade Saturated Calomel electrode (SCE).**

The electrode was prepared in accordance to the method produced at the University of Southampton. The electrode was stored in saturated KCl and the potential should remain stable and within ± 1 mV of a commercial SCE electrode.

The electrodes were set up in the arrangement shown in Figure 10:

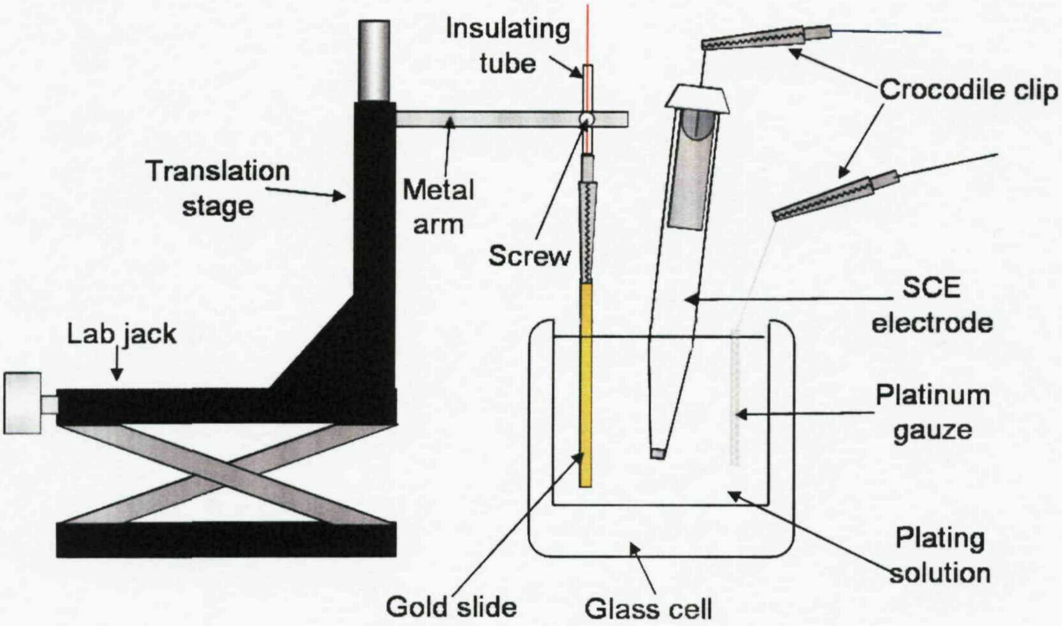

Figure 10 **Experimental set up for electrodeposition of metal.**

The working electrode was mounted onto an arm connected to a translation stage. This allows full control over the position of the electrode within the cell and, by calculating the area of the templated region on the electrode, the film height of each sample can be controlled by monitoring the charge passed through the cell. The relationship between the charge passed and film height is as follows:

$$Q = \frac{n\rho AHF}{M_r} \tag{3}$$

Where,

n = Number of moles involved in the reaction.

ρ = Density.

A = Area of electrode.

H = Height of film

F = Faraday Constant

M_r = Molecular mass

This relationship allows very precise control over the film thickness of the structure; this gives rise to the possibility of having multiple thicknesses using the same template. Each template was divided into sections, and the layers were electrodeposited one after the other, raising the substrate out of the solution in between depositions, creating a staggered film thickness.

Once the desired film thicknesses had been deposited across the template, the spheres were dissolved in DMF. A structure was then produced with increasing film thickness, as shown in Figure 11.

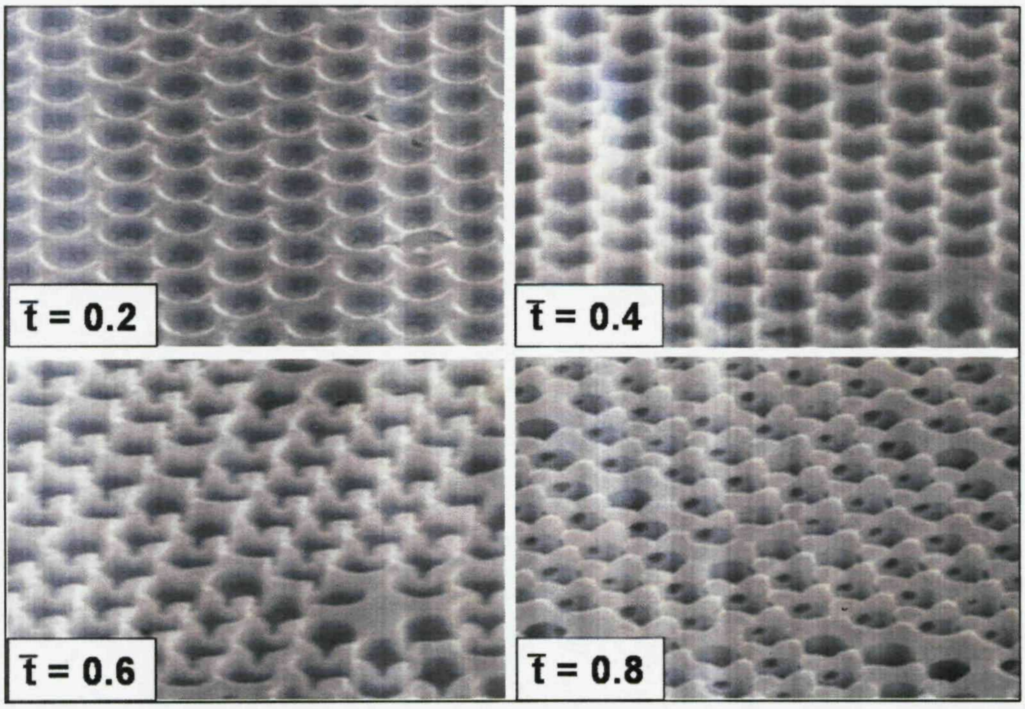

Figure 11 **Scanning Electron Microscope SEM pictures of a 600 nm film, with varying film thickness (*d*). The accelerating voltage was 15 KeV and the stage was at a tilt angle of 30 °. The magnification of the images is 20, 000**

2.3 Evaporation

The second type of surface that can be prepared using a polystyrene sphere template involves evaporating metal over the top of the spheres, producing a film similar to that of Van Duyne's MFON substrate [12].

Silver was evaporated over the template to a thickness of ~100 nm. The substrate was then immediately placed into a solution of the probe molecule, to avoid the silver oxidising in air. An SEM image of the silver structure is shown in Figure 12.

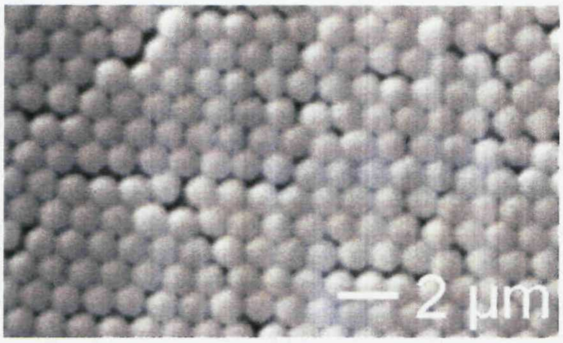

Figure 12 **SEM image showing a 200 nm silver film over a template of 600 nm polystyrene spheres. The image was acquired with an accelerating voltage of 25 KeV, and the magnification is 10,000.**

3 Scanning Electron Microscopy

Scanning Electron Microscopy (SEM) has been used to analyse the nanostructured surfaces before any other measurements were acquired. However, it is beyond the scope of this thesis to describe the intricate working of an SEM. Two models were used in this project: A Philips XL30 ESEM, in which electrons are accelerated, by a Tungsten filament source, to energy of 30 keV, the spot size used was 5 (arbitrary units) and images were recorded at magnifications of up to x 20 000, and the JOEL 5910 which has a higher resolution than the Philips, at 3 nm. The energy and spot size were varied depending on the sample, and the settings are reported with each image.

4 Raman Spectroscopy.

4.1 The Raman Effect

Raman spectroscopy arises from the detection of the Raman effect. When a molecule is polarised by incoming laser light there can be a temporary change in dipole. The laser light excites the electrons within the molecule, and while the molecule is temporarily polarised an electron can be excited, and a change in vibrational energy level can occur. If the electron should drop down to the energy level that it started from, this is known a Rayleigh scattering. However, if there is a change in vibrational energy level a photon is emitted and then this is Raman scattering, and the process is known as the Raman Effect, shown pictorially in Figure 13.

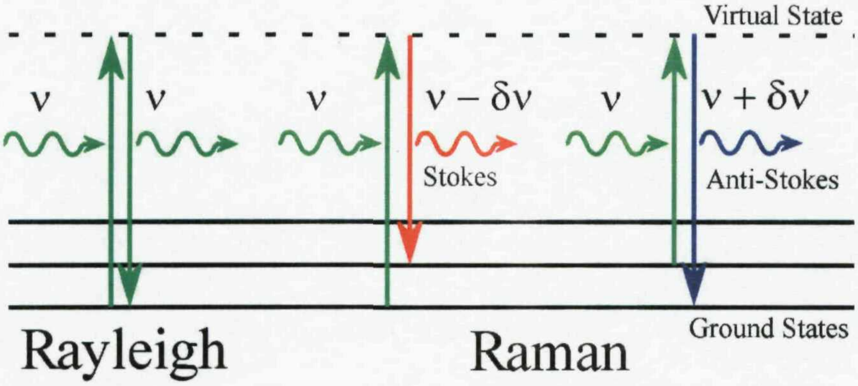

Figure 13 **Vibrational energy levels showing the Rayleigh and Raman scattering processes.**

If the Raman scattering occurs when there is an increase in the change of vibrational energy level, then this is termed Stokes scattering, whereas if there is a decrease this is termed Anti-Stokes scattering. The Raman effect is a very weak scattering phenomenon, with only 1 in 10^7 photons being Raman scattered. The Raman effect can be measured using spectroscopy.

4.2 Raman Microscopy.

The main type of Raman instrument used in this project was a Dispersive Raman system which involves using diffraction grating or prism to disperse the light and select the wavelengths seen by the detector. In this project the Raman scattered light was collected using a microscope objective. A schematic is shown in Figure 14.

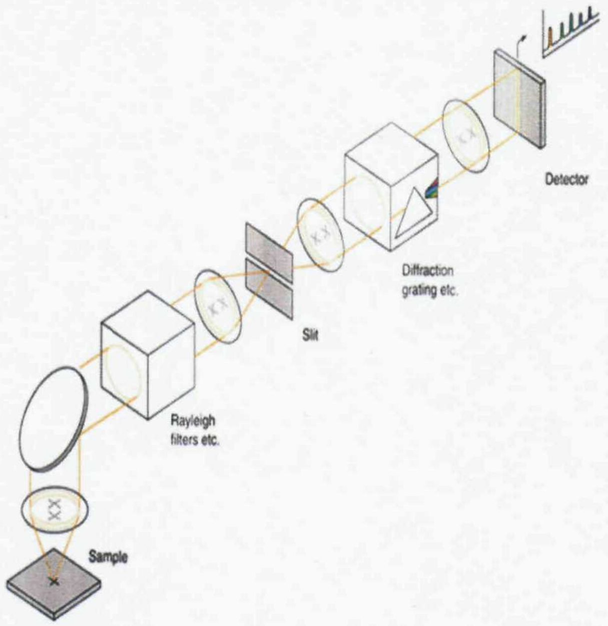

Figure 14 **A flow diagram showing the main components of a Raman Microscope system.**

A laser source (usually within the visible region of light) is used to excite molecules, and the Raman scattered light filtered out from the Rayleigh scattered light and dispersed onto a detector by a diffraction grating. The spectrometer used in this project was a Renishaw Raman 2000 system.

4.3 Renishaw Raman 2000 System.

The Renishaw Raman 2000 system, which encompasses a Leica DMLM series microscope, 632.8 nm Helium Neon laser source and a CCD detector, is shown in Figure 15:

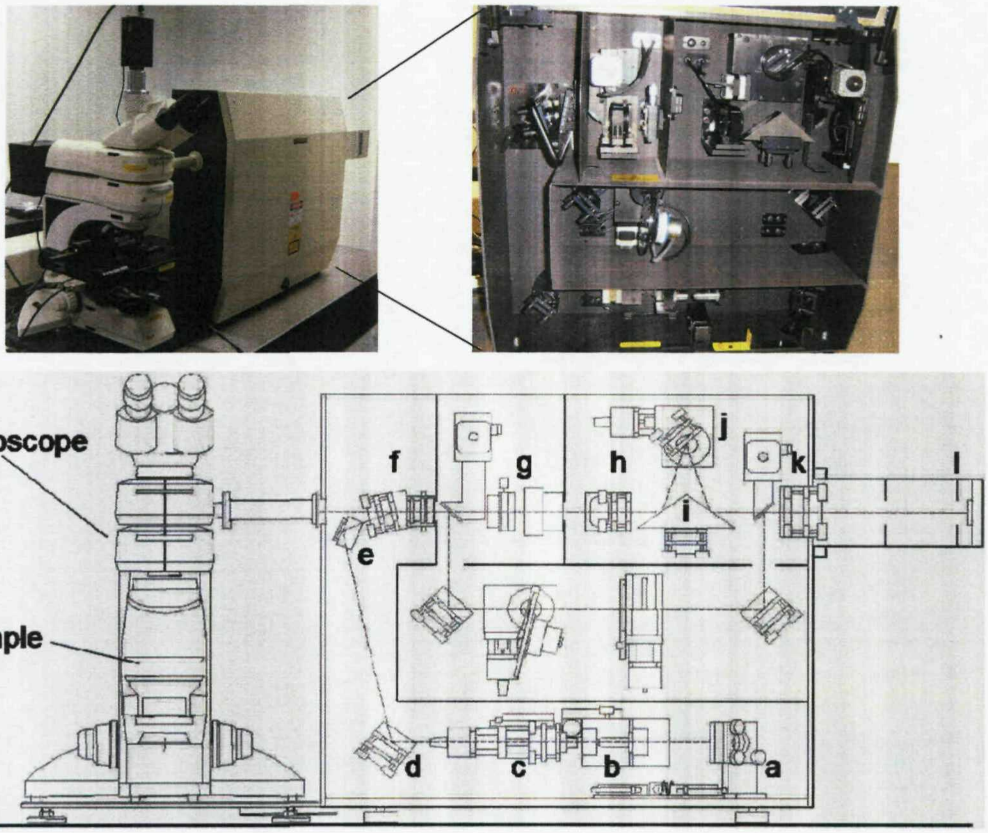

Figure 15 **The Renishaw 2000 Raman spectrometer. The main components are indicated by the letters a through l. a) Laser alignment mirror, b) × 40 objective lens and 10 µm pinhole, c) × 4 objective, d) Adjustable mirror, e) Fixed mirror, f) Holographic notch filter,g) Laser filter, h) Spectrographic entrance slit, i) Prism mirror, j) Diffraction grating assembly, k) CCD focusing lens, l) CCD detector.**

The Renishaw Raman system works is a confocal Raman system. The laser enters the system via the back of the spectrometer at mirror a. The beam is directed through the system using mirrors d and e, and then into the microscope where the sample is viewed through an objective, the laser should be aligned in such a way that the laser focuses in concentric circles.

The Raman and Rayleigh scattered light is reflected back through the microscope and the notch filters (f) cut out the Rayleigh scattering and any stray laser light, allowing only the Raman scattered light to pass through the rest of the system. The slit (g), must be set to the width to allow the greatest amount of Raman light through to the post slit lens (h), which refocuses the light onto the 1800 l/mm grating (j), using a prism (i). The scattered light is focused through the CCD lens (k), onto the CCD detector (l). The number of pixels used to collect data from the CCD is restricted because the spectrum only hits a small part of the detector, so the image area should only be this size allowing greater signal to noise within the spectrum. Figure 16 shows the image area on a standard CCD.

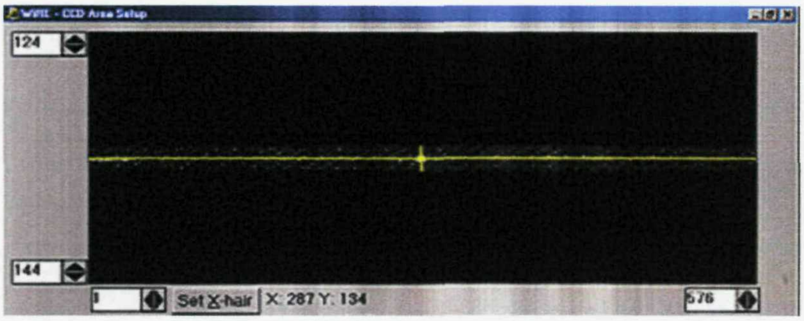

Figure 16 **Image area on the CCD detector.**

The CCD can have two different set ups. Non confocal and confocal Raman microscopy. The system is normally set up with the slit width at 50 µm and the image area on the CCD 10 pixels above and below the crosshair, when used in non confocal mode. In confocal mode the slit width is altered to 20 µm and the CCD image area is ±2 pixels from the crosshairs.

The confocality of the system can easily be measured using a piece of silicon as the sample, and collecting spectra with the focus set 10 microns above and below the surface of the silicon (at 1 micrometer intervals). The peak height of each spectrum is then plotted as a function of distance from the focal point, and the full width half maximum (FWHM) of the curve gives the confocality (hence sampling depth). The FWHM in confocal and non confocal mode are 12 µm and 32 µm respectively. The sampling volume is greatly reduced by using confocal mode. Reducing the sampling volume allows spectra to be obtained from defined volumes, or locations, such as the interface between the sample and solution.

There are two different ways of collecting Raman spectra using the Renishaw 2000 system: Static and extended scans. Static scans allow the user to focus on one particular 500 cm^{-1} region of the spectrum, and can be collected within a few seconds because the grating remains in one position throughout the accumulation. An extended scan allows the user to collect data from the whole spectral region by moving the grating. However the integration time is over any particular region of the spectrum is limited to 10 seconds using this technique.

4.4 Renishaw InVia System.

The InVia Raman system developed by Renishaw Ltd is essentially the same as the 2000 system, however all the mirrors and the notch filters are all electronically controlled, and the data is analysed using Renishaw Wire 2 software. The sample is also held within an enclosure cutting out any light interference. Work was carried out using the InVia system when working with 785 nm and 830 nm excitation.

4.5 Instrument Calibration and Scan Parameters.

Before measurements were taken, each system was calibrated using silicon as a reference. The silicon peak should occur at 520.4 cm^{-1}, and any variation was accounted for by offsetting the grating.

All Raman spectra collected within this project were collected using an extended scan from 3200 to 200 cm^{-1} with a single 10 s accumulation (which takes approximately 50 seconds to record a complete spectrum), using a ×50 objective produced by Leica, in non-confocal mode, unless otherwise stated. The spectral resolution is 4 cm^{-1}. All data was collected using laser powers between 0 and 10 mW across 4 laser wavelengths, and data was corrected for variations between power when comparing data.

4.6 Combined SEM and Raman.

The SEM with structural chemical analyser (SEM-SCA) incorporates a Raman imaging probe into an SEM system. This allows Raman measurements to be acquired from chosen points on a sample, with excellent spatial accuracy. The main components of the system are shown schematically in Figure 17

Figure 17 **The Renishaw SEM-SCA (A), the inside of the SEM chamber, showing the fibre optic Raman probe (B) and a schematic of the inside of the SEM showing the Structural and Chemical Analyser (C).**

The sample is mounted as in a standard SEM, discussed previously, however the working distance between the electron gun and the sample is larger (approximately 20 mm) in comparison to the standard set up, allowing room for the optics transfer tube (OTT). The sample can still be viewed when the OTT is in position, however it is a limited view, therefore the OTT is removed to acquire SEM images.

The 785 nm diode laser is coupled to an InVia spectrometer, and is carried to the SEM using a fibre probe, which has a spot size of 1.2 µm. The spectra were collected when the electron beam was blanked, which prevented any carbon building up on to the sample while the spectra were collected. Images were collected after each spectrum and the experimental details for each image are labelled individually.

5 Electrochemical Methods.

Electrochemistry is a useful analytical technique when it comes to monitoring surface reactions and modification. In this study chronoamperometry was employed for electrodepositing metal, as discussed previously, and while collecting Raman measurements in an electrochemical cell. Voltammetry was used to clean the substrate and remove any adsorbed molecules and to prepare electrochemically roughened surfaces.

5.1 Voltammetry.

Voltammetry covers a group of electrochemical methods, in which information about surface reactions and electrochemical processes is gained from measuring the current as a function of applied potential. The current response observed is dependent on the charge transfer processes taking place at the surface of the working electrode.

Cylic voltammetry (CV) is one of the simplest of these techniques, and was primarily used throughout this project. In CV the potential is swept from an initial potential, E_1, to a vertex potential, E_2, and returns to the initial potential, E_1, at a known sweep rate, υ.

5.1.1 Preparation of roughened SERS substrates.

Roughened gold and silver substrates were prepared using the Oxidation Reduction Cycle (ORC) method [32], which involves cycling a metal electrode numerous times, allowing the surface to become atomically rough. Table 3 lists the potential curves, electrolytes and sweep rates involved in the preparation of these substrates.

Table 3 **Experimental conditions for the preparation of gold and silver ORC SERS substrates.**

	Electrolyte	Potential Waveform	Parameters (E /V vs. SCE, t /s)	Cycles	Surface Appearance
Ag	0.1 M KCl	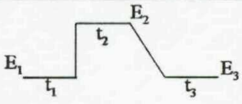	$E_1 = E_3 = -0.25$, $E_2 = 0.25$. $t_1 = 15$, $t_2 = 8$, $t_3 = 60$	1	Milky Yellow
Au	0.1 M KCL	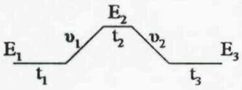	$E_1 = E_3 = -0.3$, $E_2 = 1.2$. $t_1 = t_3$ 30, $t_2 = 1.2$ $\upsilon_1 = 1$, $\upsilon_2 = 0.5$	25	Dark Brown

The substrates were treated in the same manner as has been previously described for the nanostructured substrate, before Raman spectra were collected.

5.2 In-Situ Spectroelectrochemistry.

Raman experiments were often run simultaneously with electrochemical measurements during the course of this project. Chronoamperometry (described previously) was used to control the potential whilst accumulating a Raman spectrum. Figure 18 shows the cell and electrode set up that were used for this purpose.

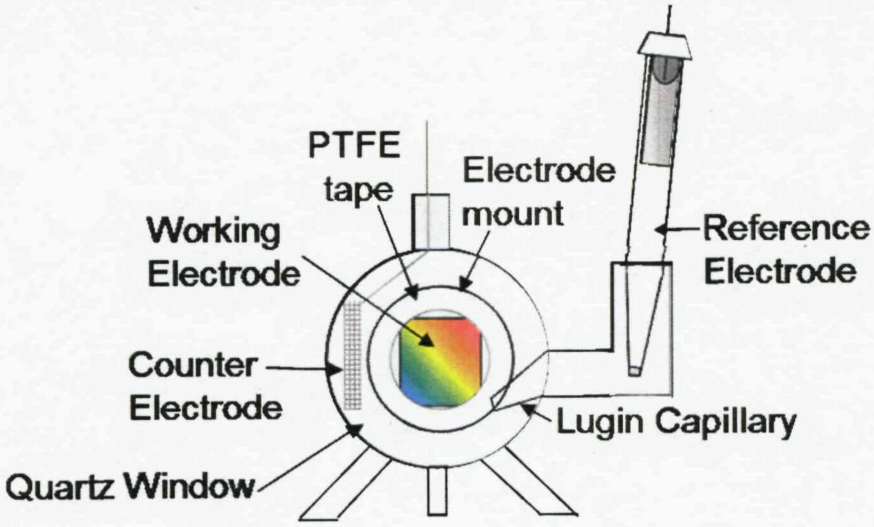

Figure 18 **Front view (not to scale) of the spectroelectrochemical cell used in conjunction with the Renishaw Raman 2000 system.**

The SERS substrate was mounted onto an electrode, consisting of a Pt wire encased in a glass tube, using a small piece of carbon tape and silver paint to ensure a connection was made with the gold on the top of the glass microscope slide. The electrode was secured using PTFE tape.

In order for the Raman spectra to be collected the laser beam was reflected using a macro lens set (Ventacon), so that it was at a perpendicular angle to the objective, and the laser beam was focussed through the quartz window onto the electrode surface.

6 Optical Spectroscopy

As previously mentioned, historically SERS substrates generally consist of randomly structured surfaces, which, although give good enhancements, are extremely irreproducible. The enhancements come from random 'hot spots' of tightly localised plasmons, which produce enhancements of the electromagnetic field. However in order to engineer surfaces to produce the greatest SERS signals, the surface plasmons must be fully monitored and understood. To do this, two techniques are employed: normal incident reflection spectroscopy, and angle resolved reflection measurements, both of which are fully described in Chapter 3, along with a detailed discussion of the plasmon modes observed.

7 Summary

All techniques described within this chapter were used in collaboration with each other to obtain the greatest understanding of the SERS substrates in question. Imperfections on the substrates, i.e., scratches etc, were used as reference points to ensure that the same areas were being sampled when different results were being compared.

8 References

1. Fleischmann, M., P.J. Hendra, and A.J. McQuillan. Chem. Phys. Lett., 1974. **26**(2): p. 163-166.
2. Aroca, R. and G.J. Kovacs. Journal of Molecular Structure, 1988. **174**: p. 53-58.
3. Goudonnet, J.P., G.M. Begun, and E.T. Arakawa. Chemical Physics Letters, 1982. **92**(2): p. 197-201.
4. Liao, P.F., J.G. Bergman, D.S. Chemla, A. Wokaun, J. Melngailis, A.M. Hawryluk, and N.P. Economou. Chemical Physics Letters, 1981. **82**(2): p. 355-359.
5. Bright, R.M., M.D. Musick, and M.J. Natan. Langmuir, 1998. **14**(20): p. 5695-5701.
6. Huang, Q.J., J.L. Yao, B.W. Mao, R.A. Gu, and Z.Q. Tian. Chemical Physics Letters, 1997. **271**(1-3): p. 101-106.
7. Bright, R.M., D.G. Walter, M.D. Musick, M.A. Jackson, K.J. Allison, and M.J. Natan. Langmuir, 1996. **12**(3): p. 810-817.
8. Freeman, R.G., K.C. Grabar, K.J. Allison, R.M. Bright, J.A. Davis, A.P. Guthrie, M.B. Hommer, M.A. Jackson, P.C. Smith, D.G. Walter, and M.J. Natan. Science, 1995. **267**(5204): p. 1629-1632.
9. Haynes, C.L. and R.P. Van Duyne. Journal of Physical Chemistry B, 2001. **105**(24): p. 5599-5611.
10. Jensen, T.R., M.D. Malinsky, C.L. Haynes, and R.P. Van Duyne. Journal of Physical Chemistry B, 2000. **104**(45): p. 10549-10556.
11. Jensen, T.R., R.P. Van Duyne, S.A. Johnson, and V.A. Maroni. Applied Spectroscopy, 2000. **54**(3): p. 371-377.
12. Vanduyne, R.P., J.C. Hulteen, and D.A. Treichel. Journal of Chemical Physics, 1993. **99**(3): p. 2101-2115.
13. Litorja, M., C.L. Haynes, A.J. Haes, T.R. Jensen, and R.P. Van Duyne. Journal of Physical Chemistry B, 2001. **105**(29): p. 6907-6915.
14. Tian, Z.Q., Z.L. Yang, B. Ren, and D.Y. Wu, in *Surface-Enhanced Raman Scattering: Physics and Applications*. 2006. p. 125-146.
15. Tian, Z.Q., Z.L. Yang, B. Ren, J.F. Li, Y. Zhang, X.F. Lin, J.W. Hu, and D.Y. Wu. Faraday Discussions, 2006. **132**: p. 159-170.
16. Ren, B., X.F. Lin, J.W. Yan, B.W. Mao, and Z.Q. Tian. Journal of Physical Chemistry B, 2003. **107**(4): p. 899-902.

17. Liu, G.K., J.L. Yao, B. Ren, R.A. Gu, and Z.Q. Tian. Electrochemistry Communications, 2002. **4**(5): p. 392-396.
18. Abdelsalam, M.E., P.N. Bartlett, T. Kelf, and J. Baumberg. Langmuir, 2005. **21**(5): p. 1753-1757.
19. Prakash, G.V., L. Besombes, T. Kelf, J.J. Baumberg, P.N. Bartlett, and M.E. Abdelsalam. Optics Letters, 2004. **29**(13): p. 1500-1502.
20. Abdelsalam, M.E., P.N. Bartlett, J.J. Baumberg, and S. Coyle. Advanced Materials, 2004. **16**(1): p. 90-+.
21. Bartlett, P.N., J.J. Baumberg, S. Coyle, and M.E. Abdelsalam. Faraday Discussions, 2004. **125**: p. 117-132.
22. Bartlett, P.N., J.J. Baumberg, P.R. Birkin, M.A. Ghanem, and M.C. Netti. Chemistry of Materials, 2002. **14**(5): p. 2199-2208.
23. Coyle, S., M.C. Netti, J.J. Baumberg, M.A. Ghanem, P.R. Birkin, P.N. Bartlett, and D.M. Whittaker. Physical Review Letters, 2001. **8717**(17).
24. Netti, M.C., S. Coyle, J.J. Baumberg, M.A. Ghanem, P.R. Birkin, P.N. Bartlett, and D.M. Whittaker. Advanced Materials, 2001. **13**(18): p. 1368-1370.
25. Campbell, D.J., E.R. Freidinger, J.M. Hastings, and M.K. Querns. Journal of Chemical Education, 2002. **79**: p. 201.
26. Hosokawa, K., I. Shimoyama, and H. Miura. Sensors and Actuators a-Physical, 1996. **57**(2): p. 117-125.
27. Kralchevsky, P.A. and N.D. Denkov. Current Opinion in Colloid & Interface Science, 2001. **6**(4): p. 383-401.
28. Alfrey Jr. T, Bradford. EB, Vanderhof. JW, and Oster. G. J. Optical Soc. Am., 1954. **44**: p. 603 - 609.
29. Velev, O.D., P.M. Tessier, A.M. Lenhoff, and E.W. Kaler. Nature, 1999. **401**(6753): p. 548-548.
30. Group, S.E. 1985: Ellis Horwood Limited.
31. Szamocki, R., S. Reculusa, S. Ravaine, P.N. Bartlett, A. Kuhn, and R. Hempelmann. Angewandte Chemie-International Edition, 2006. **45**(8): p. 1317-1321.
32. Tian, Z.Q., B. Ren, and D.Y. Wu. Journal of Physical Chemistry B, 2002. **106**(37): p. 9463-9483.

Chapter Three Optical Properties of Sculpted SERS Substrates.

1 Introduction

It has been widely accepted that there are two theories as to why Raman scattering is enhanced by modified surfaces: the chemical enhancement model and the electromagnetic model. The chemical enhancement model is essential a charge transfer mechanism between the metal and molecule and only account for 10^3 to 10^4 enhancements, it is also molecular specific. The electromagnetic model is thought to account for a 10^4 to 10^6 enhancement; however the reasons behind the enhancement are still under debate. Surface plasmon polaritons are thought to be the dominant factor and this chapter explains the basics behind plasmons, and how they can be monitored and controlled with the sculpted surfaces used in this project.

2 History of Surface Plasmon Polaritons (SPP's)

Interesting optical properties of metals were seen as early as the 4th century AD, and the most common example is the Lycurgus cup, Figure 1.

Figure 1 The Lycurgus cup. Dating back to 4th Centruy AD, this cup shows optical properties which are now known to be surface plasmon polaritons. [1]

This cup possesses very interesting optical properties. When the cup is viewed in daylight it appears green, however when the cup is illuminated from within it appears red. In very simple terms, this is due to the metallic particles within the glass (the same is true for some stained glass), as light hits the tiny particles it is diffracted and this results in a colour change.

The way that light interacts with a metal surface is easily described using a mirror as an example. Metals are characterised by the presence of free electrons within in them. Light and electrons have an intimate connection due to their electric fields. The oscillation of the light field causes the electrons in the metal to also oscillate. Because the electrons have some mass it takes time to get them moving, so they tend to oscillate in anti-phase with the optical field. This movement stops the light from entering the material, the electrons create a screening field that the light cannot pass through, and thus the light is reflected.

In the case of the cup the pieces of metal are so small that the movement of the free electrons is restricted. The free electrons moving around the metal particles in the cup can only oscillate at certain frequencies, this is the simplest definition of a surface plasmon; an oscillation of the free electrons at the surface of a metal at a certain frequency. At these frequencies the light is absorbed and scattered leading to a reduced transmission but enhanced reflection, giving the cup its properties. By altering the size of the metal particle the scattered colours/wavelengths (and therefore transmitted colours) are altered. However, it wasn't until the 1950s that surface plasmons became recognized, due to the pioneering work done by Ritchie *et al.* [2]

The general concesus is that surface plasmons (SP), interacting with metal structures, are essentially light waves that are trapped on the surface because of their interaction with the free electrons of the surface. In this interaction, the free electrons respond collectively by oscillating in resonance with the light wave. The resonant interaction between the surface charge oscillation and the electromagnetic field of the light constitutes the SP and gives rise to its unique properties.

The longitudinal surface charge oscillations give rise to an electric field perpendicular to the interface which decays exponentially with distance, shown pictorially in Figure 2. This corresponds to an evanescent field above the surface with a decay length similar to that of the wavelength of light. The plasmon has similar properties to the optical field but always has a greater momentum and is non-radiative.

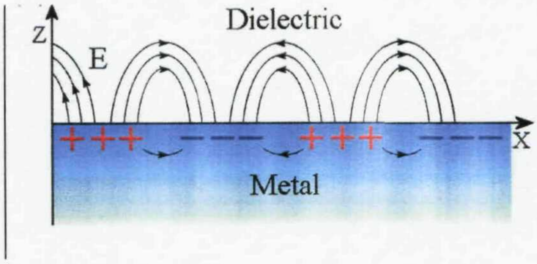

Figure 2 **Schematic of the surface charge and electric field. [3]**

It is possible to create a standing wave SP due to the non-radiative nature of the plasmon, especially when it is confined to a surface such as a grating or photonic crystal.

2.1 Photonic Crystal Structures

The production of photonic crystals allows fantastic control over light, and can be used to produce micron-scale optical circuits, through which the light is squeezed and manipulated. The earliest and most common examples of photonic crystals are the Papilio Ulysses butterfly and a naturally occurring opal, shown in Figure 3.

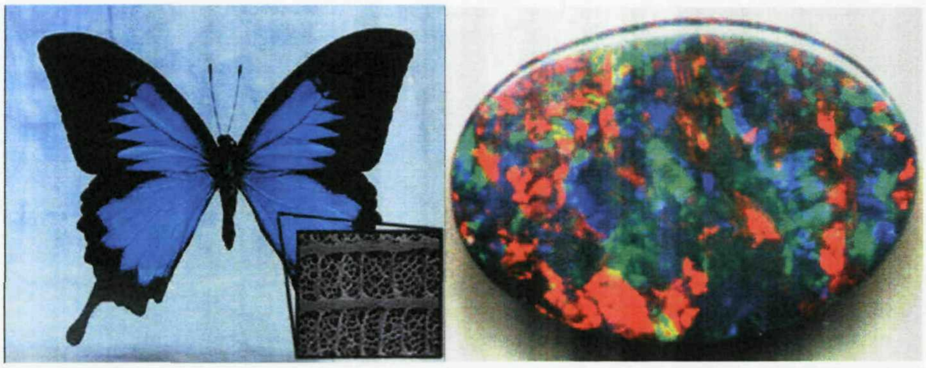

Figure 3 **The Papilio Ulysses butterfly [1], found in Australia and the optical properties shown in a natural opal.**

The butterfly's wing and the piece of opal are great examples of how structuring on this size scale leads to strong optical effects. The butterfly's wing acts as an optical filter, only reflecting blue light, producing the vibrant colour. It is important to note that the better the ordering of the structure the stronger the optical effect will be. The opal has more variation in colour because it has a more random structure, leading to the reflection of different colours from different places.

There are many groups who have specialized within the area of photonic crystal structures [4-6], an excellent review of plasmonics properties of nanostructures was produced in the MRS Bulletin with articles published by Halas [7] and Xia [8, 9] on the properties of shape controlled nanostructures . However, very few structures can control the plasmons in the way that has been developed within the group at the University of Southampton [10-17].

The SERS substrates developed in this project have been based upon what is seen in nature but are essentially diffraction gratings, which interact with light producing opalescent patterns, Figure 4.

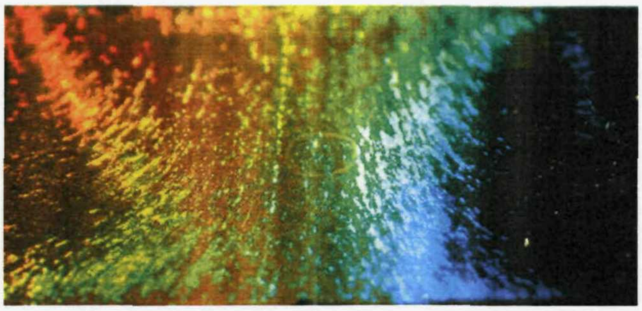

Figure 4 **600 nm ½ d gold nanostructured SERS substrate as seen when illuminated with a white light.**

Depending on how thick the film is grown around the original sphere template the light interacts with the SERS substrate in one of two ways, diffraction from the rim of the dishes, or interference from the light within the dishes and the ingoing light.

3 Diffraction.

Diffraction, from the SERS substrate, occurs when the film is very thin or thick and there is a large top surface area in between the dishes. This allows for the light waves to propagate between the dishes before being scattered. The scattering of light can be described in terms of Bragg scattering/diffraction.

3.1 Bragg Scattering.

The simplest example of Bragg diffraction is that from a crystal structure: as a wave of light enters the crystal, some portion of it will be reflected by the first layer, while the rest will continue through to the second layer, where the process continues. By the definition of constructive interference, the separately reflected waves will remain in phase if the difference in the path length of each wave is equal to an integer multiple of the wavelength ($n\lambda$), the path difference is given by:

$$n\lambda = 2d\sin\theta$$

Where d denotes the interplanar distance and θ the angle of incidence, as shown schematically in Figure 5.

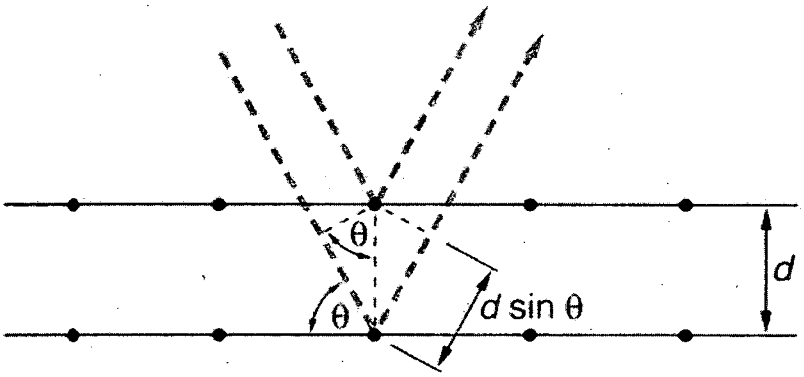

Figure 5 **Bragg diffraction from a crystal structure [18].**

Waves that satisfy the Bragg condition interfere constructively and result in a reflected wave of significantly changed intensity. In terms of the photonic crystal structures, this change in intensity is seen as a colour change, and is seen clearly in Figure 4. Due to the hexagonal close packing of spheres in the original template for the SERS substrate, a 2D six fold diffraction pattern is observed, as shown in Figure 6.

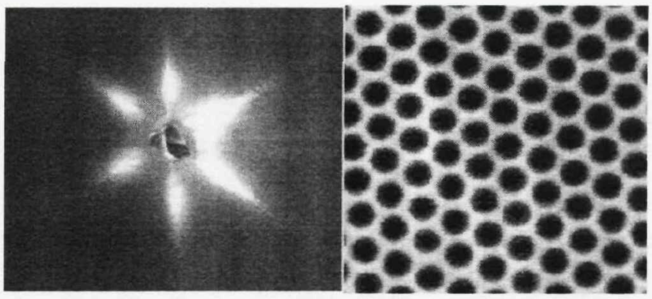

Figure 6 Diffraction of white light upon a nanostructured gold film with 600 nm pores and a film thickness of 0.3 d.

The image shown in Figure 6 is simply the diffraction pattern observed when a white light laser illuminates the surface of a 600 nm ¾ d substrate, at an angle of incidence of 0 °. This pattern can also be observed within Bragg plasmon modes, and will be discussed further in following sections.

3.2 Mie Scattering

The second type of diffraction between the SERS substrates and incident light is Mie scattering. Mie scattering formed part of the initial research into plasmonics, which can be traced back to the first studies of the optical properties of metals when Michael Faraday observed the changing colours of solutions of gold colloids. Since then a great deal of progress has been made in this field, but metallic colloids are still used in the forefront of research; especially in the field of surface enhanced Raman scattering. Whilst the SERS substrate developed within this project does not use metal particles, many of the results require an understanding of the tools developed from colloidal theory [19].

It has been shown that in two-dimensions the optical properties of metals can be significantly modified by surface plasmon resonances and surface effects dominate the optical properties of small metal particles. It has also been noted that a SPP can travel up to about 10 μm over a metal film at visible frequencies. If a metal particle with a diameter of several nanometres is considered, a SPP will traverse the particle many times before decaying. In reality, a SPP mode will interfere with itself as it travels around the particle, leading to an electro-magnetic standing wave. This standing wave will follow the field of the incident light, taking a dipole form for particles much smaller than the wavelength of light, as shown pictorially in Figure 7.

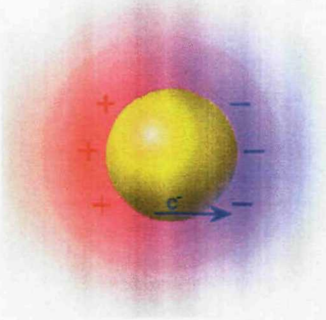

Figure 7 **Pictorial representation of the electric field (the blue arrow indicates the direction of the field) around a colloidal particle (yellow sphere) when illuminated. The electric field arises due to the formation of an *electromagnetic standing wave formed when light traverses an object smaller than itself.***

An electromagnetic wave can probe structures many times smaller than its wavelength, as shown in Figure 8 where gold coatings have been applied to sub-micron sized dielectric particles in solution. By varying the thickness of the gold layer by tens of nanometres the SPP is tuned, in turn tuning the maximum scattering frequency, thereby altering the colour of the light transmitted through the solution [20].

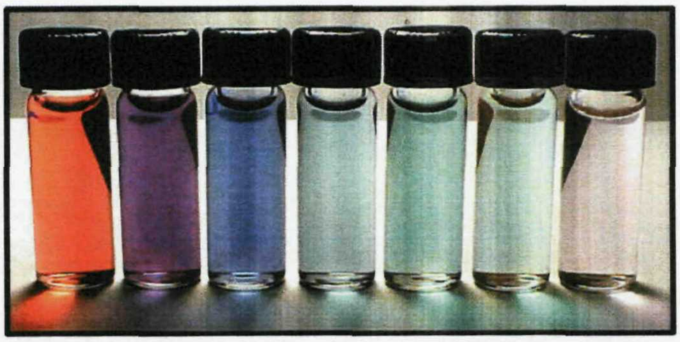

Figure 8 **Solution of Ag nano-shell particles from [21], increasing the shell thickness (left to right) alters the surface plasmon energy to longer wavelengths and changes the scattering efficiency.**

The idea of standing waves around a colloid can be applied to the void structure used in this project, except that the standing wave forms within the cavity rather than around it, and there are many different patterns in which the standing wave can arise. Recent publications from the Baumberg group in the School of Physics at the University of Southampton have given a very thorough over view of the plasmon modes [1, 10-12], predicted and observed, from the SERS substrates, and a brief summary of Mie and Bragg plasmons is given in the following section.

4 Plasmon modes of sculpted SERS substrates.

It has recently been shown that absorbance features observed in reflectance spectra of the sculpted surface may be described in terms of the relative contributions of SPPs, which may be attributed to either Bragg plasmons or localised Mie plasmons [22]. Reflectance spectroscopy is a way of monitoring the light that is reflected back from the surface, when it is probed by a white light laser. There are two types of spectroscopy that have been used in this project: Normal incidence and angular resolved reflectance spectroscopy, the experimental set up of both will be described in the following section.

4.1 Normal Incidence Reflection Spectroscopy.

All reflectance spectra were recorded using a BX51 TRF Olympus optical microscope. The samples were illuminated by a white light source and the images were recorded using a CCD camera (DP2 Olympus). A fibre optic coupled spectrometer (Ocean Optics, spectral range 300 – 1000 nm, resolution 1 nm) placed in the focal plane of the image was used to record the spectral response from the selected area, the spot size of the fibre is 50 μm.

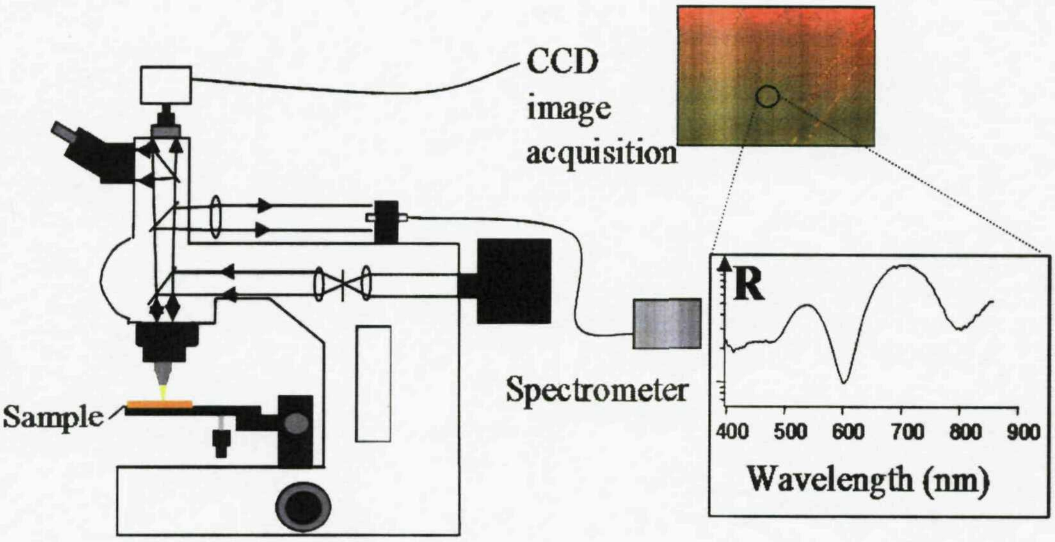

Figure 9 **Experimental arrangement used to record reflection spectra from small areas of the sample with simultaneous optical microscopy**

The same areas of the samples were used for both Raman and reflectance spectra. Well ordered areas of sample were pin pointed using the SEM images acquired and the optical images were used to find irregularities and defects in the film as reference points. Replicate measurements were made at each step to verify the spectra were a true representation of each step in film thickness.

An example of the spectra obtained using this method is shown in Figure 10.

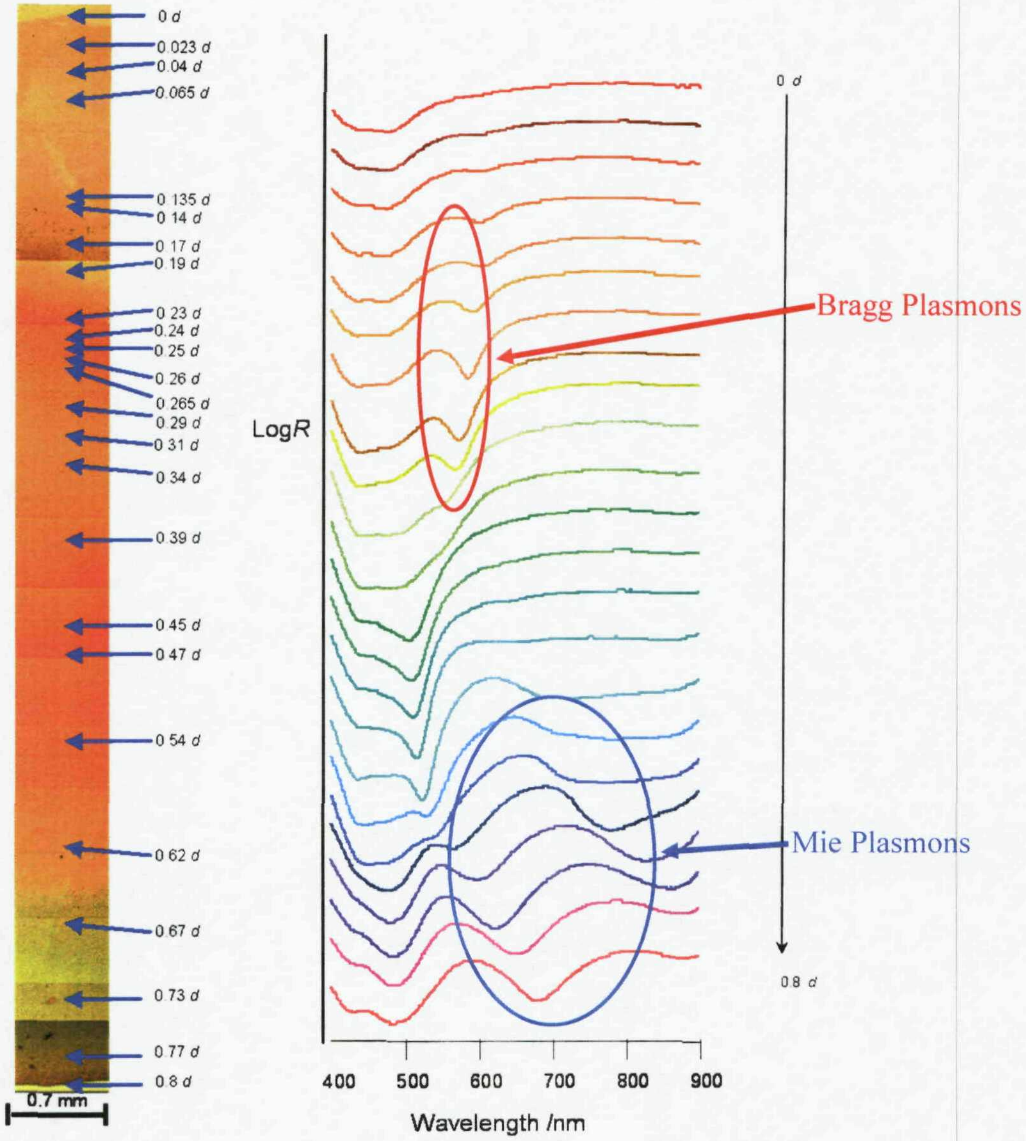

Figure 10 **Example of reflection spectra and white light images obtained. The image on the left shows the white light images of the whole sample, and the blue arrows (indicating the film thicknesses) show the positions at which the reflection spectra were recorded. The spectra are off set for clarity.**

The sample is illuminated from above at normal incidence (0°), and the light is then reflected back through the microscope. If the surface interferes with or absorbs the light a dip will be observed in the spectrum. The spectrum at the top of Figure 10 comes from the area corresponding to the arrow marked 0 *d*, this is the response from flat gold, as the film becomes structured, the interactions between the surface and the light increase.

For the thinnest films, < 0.2 *d* thick, the surface of the metal film consists of a hexagonal array of shallow circular dishes, with the top surface consisting of flat areas of metal separating the dishes. Surface plasmon-polaritons are able to travel across this surface, being scattered off the rims of the dishes, giving rise to Bragg diffraction modes. These modes are evident as the absorbance features in the reflectance spectra (Figure 10) observed between 550 nm and 600 nm for the thinner films, and they move to shorter wavelengths as the film thickness is increased.

At a thickness of 0.5 *d*, corresponding to hemispherical voids, the top surface breaks up into disconnected triangular islands and the fraction of the area of the top surface that is flat is a minimum. At this point the scattering of the Bragg modes at the top surface starts to give way to the absorbance features seen from thicker films. For films with thickness ≥ 0.4 *d* localised plasmons are trapped within the spherical cavities in addition to the surface plasmons traveling across the top surface. The two different types of interaction can be seen in Figure 11, these plasmons can be modeled using Mie theory and are, therefore, termed Mie Plasmons.

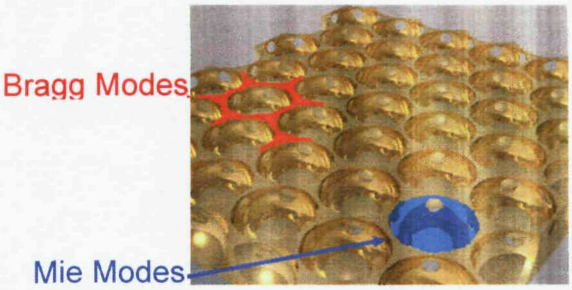

Figure 11 **Computer generated image of a porous structure, showing where the Bragg and Mie plamons occur.**

As previously discussed, the surface gives rise to a six fold diffraction pattern. Therefore, to obtain a full overview of how the surface interacts with light, the samples must be illuminated, and data collected from various angles of incidence. To do this an angular reflectance spectroscopy rig was set up in the School of Physics.

4.2 Angle Resolved Measurements.

The dispersion of the plasmons is investigated by recording the reflectivity spectrum for different incident angles θ and sample azimuthal orientations φ and for various sample thicknesses *d* and hence geometries.

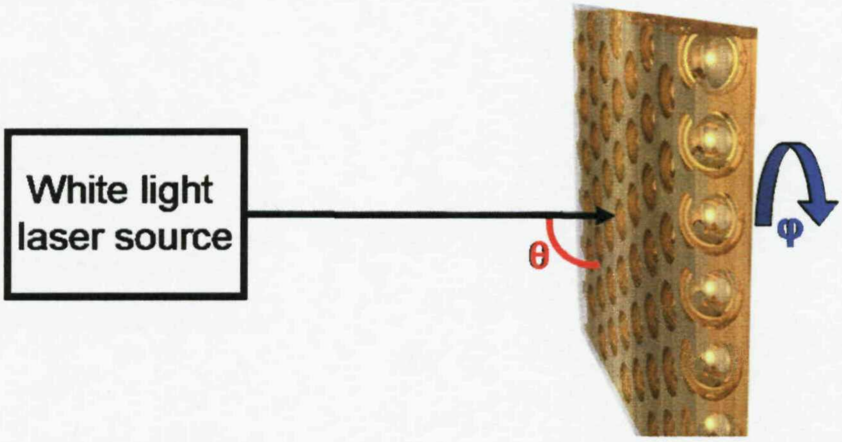

Figure 12 Sample orientation and incident angles for angle resolved reflectivity measurements. Θ is the angle of incidence of the white light laser and φ is the sample orientation or azimuthal angle.

A supercontinuum white-light laser was used to simultaneously study absorption features throughout the visible and infrared spectral regions. Samples were mounted on a custom-built computer-controlled goniometer. This can be programmed to move in both the θ and φ directions as well as move in the *x*-*y* plane of the sample. An optical fiber is attached to the end of the goniometer arm, on which the reflected light is focused, and this was also positioned under computer control. The light is polarised before illuminating the sample and a polariser was placed before the fiber to select the polarisation of the reflected light. Spectra were collected using both visible and infrared spectrometers (Ocean Optics USB2000 and NIR512), which were also controlled via the same software used to operate the goniometer. This setup can therefore perform reflectivity measurements over a wide range of parameters. The data collected are then combined into a matrix where they can be viewed as a contour map and analyzed [23]. An example of a contour map is given in Figure 13.

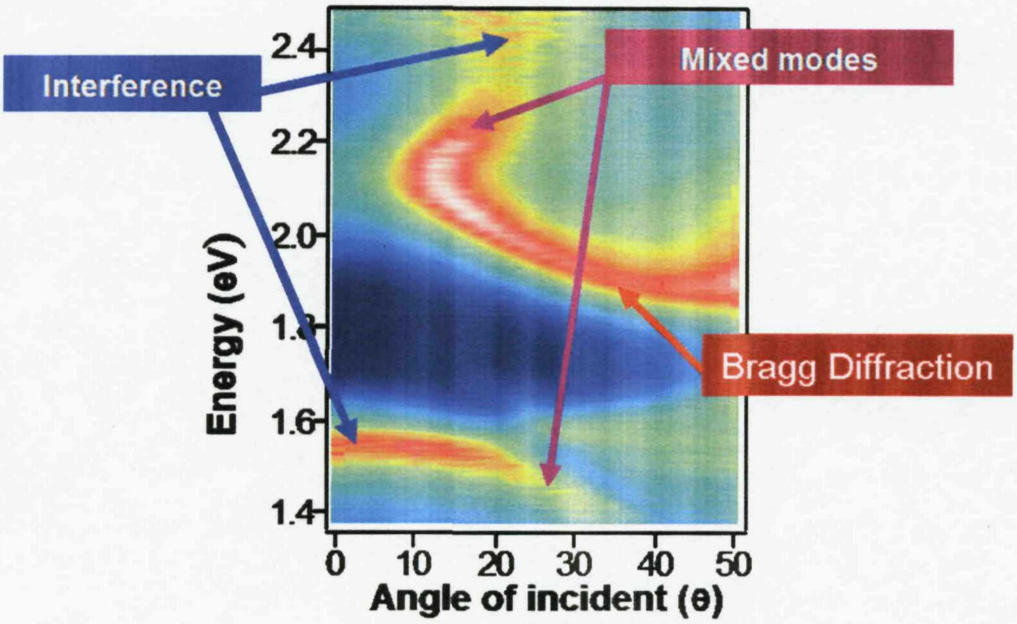

Figure 13 **An example of a contour plot of the reflection spectrum, showing how light interacts with the surface at different incident angles (θ). Red corresponds to greatest absorbance and blue the least. Each normal incident spectrum, as shown in Figure 10 can also be represented by a contour plot.**

It is possible to create a contour plot such as the one in Figure 13, for every normal reflection incidence spectrum in Figure 10, and hence compare Figure 14 with Figure 10.

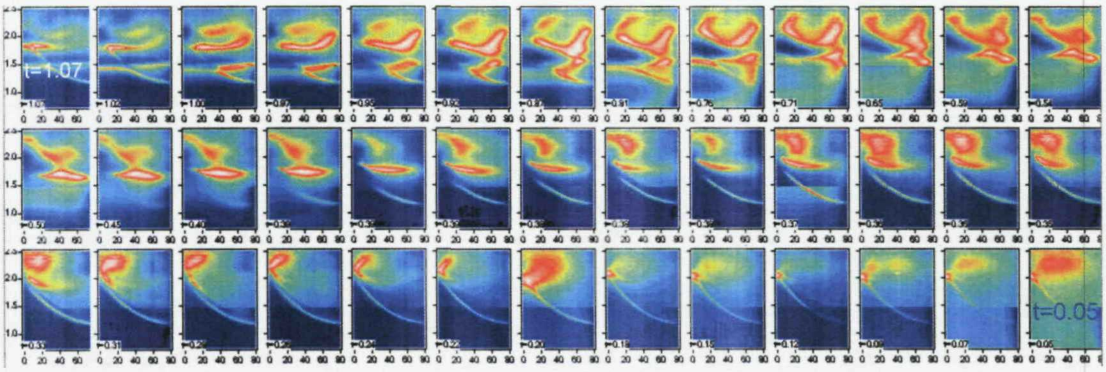

Figure 14 **Contour plots of reflectance spectra for varying degrees of film thickness (*d*) increasing from left to right across each row, from a 500 nm sample. With the thinnest end of the sample being in the bottom left and the thickest end of the sample being in the top right corner.**

It is also possible to take one angle of incidence and plot all variations of *d* as one figure as shown in Figure 15.

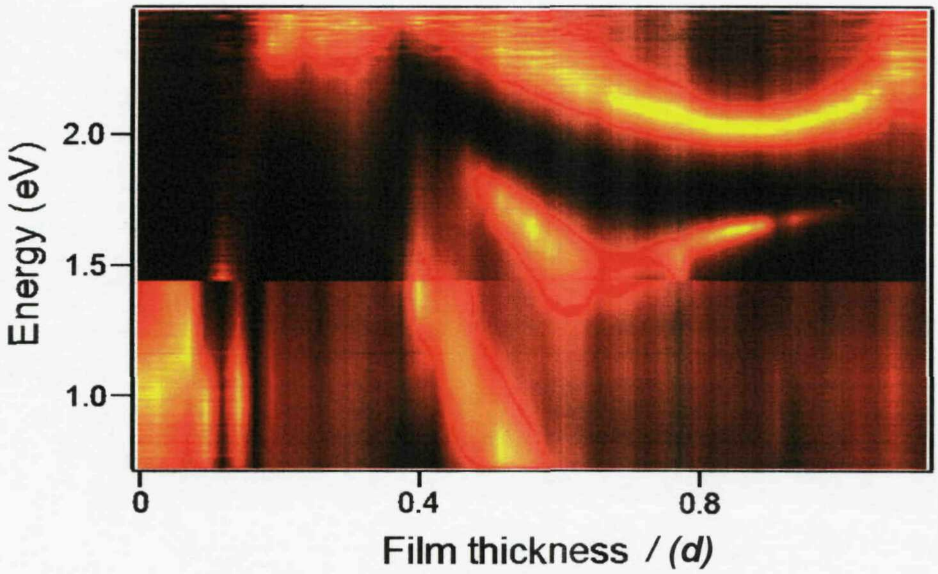

Figure 15 **Contour plot for one incident angle as a function of film thickness (*d*). The angle resolved reflection spectrum was recorded for a 500 nm with film thickness that was fully graded from 0 to 1 *d*. The spectrum was collected with an incident angle of 0°.**

The angle resolved reflectance spectrum shown in Figure 15 can be compared directly to a normal incidence spectrum, except that the results are shown as a contour plot with the intensity of the plasmon modes (yellow being the highest and black the lowest), being represented in the z axis.

Using each of the techniques described in sections 4.1 and 4.2 it is possible to predict and assign plasmon modes to different film thicknesses of samples.

4.3 Modelling of plasmon modes

Recent papers published by our collaborators in the School of Physics at the University of Southampton, led by Prof. Jeremy Baumberg [11-13, 16] have comprehensively summarized the different modes within the void substrate. The results of their calculations/models are summarized below so that the concepts may be applied to the surfaces developed in this thesis in later chapters.

4.3.1 Bragg Plasmons

For sample regions where $d < 0.3$ the nanostructured surfaces take the form of a thin two-dimensional grating and a six-fold diffraction pattern from these structures is observed. This model assumes the surface to be flat with point scattering, from the rims of the cavity, in a hexagonal lattice. All six modes are only seen when the sample is illuminated from varying incident angles (ϕ), as shown in Figure 16.

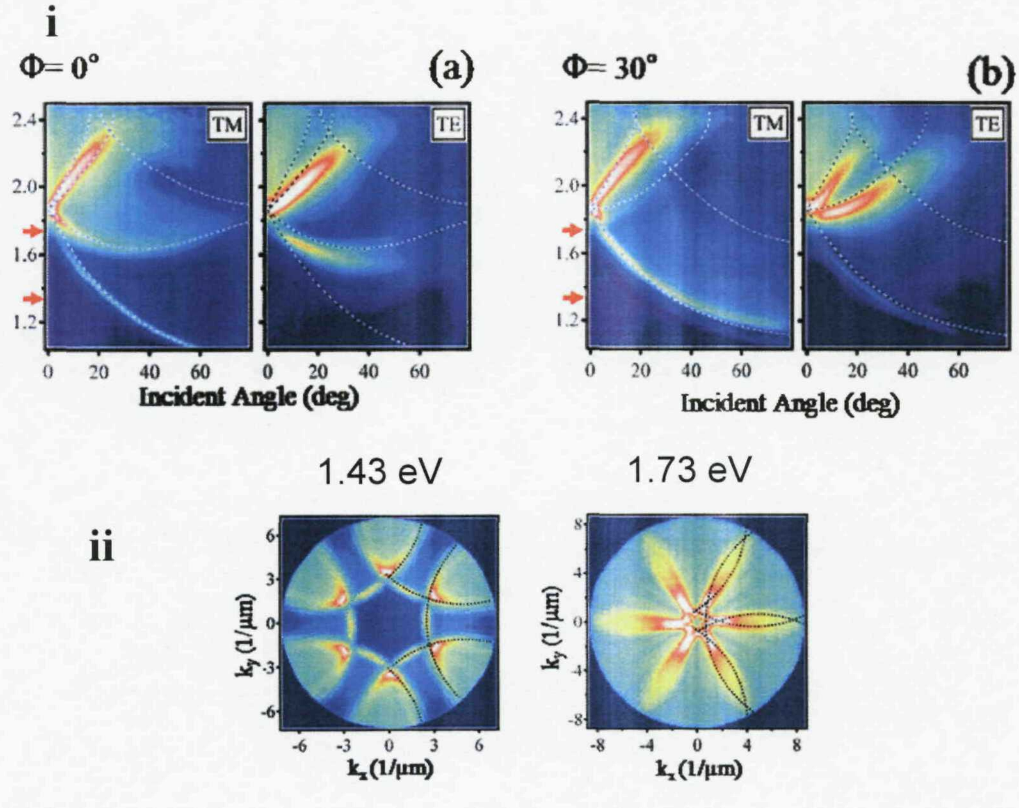

Figure 16 **(i) Reflectivity of a surface with a void diameter of 700 nm at a thickness of 0.3 d, for incident angle (ϕ) 0° (a) and 30° (b). The dotted white lines show the theoretical Bragg plasmons. The red arrows show the energies that were used to show the arrangement of the six fold diffraction pattern in Figure 16 ii. (ii) The six fold Bragg diffraction pattern at the energies 1.43 and 1.73 eV.**

The Bragg modes fit very well with theoretical calculations up to 0.3 *d*, however at this point it must be assumed that that plasmon is tightly bound to the surface in order to allow for film thickness variations to be considered up to 0.4 *d*. At this thickness they are no longer seen on the surface as the top surface breaks into triangular sections (Figure 17), and the mode becomes encompassed within the void, as a Mie plasmon.

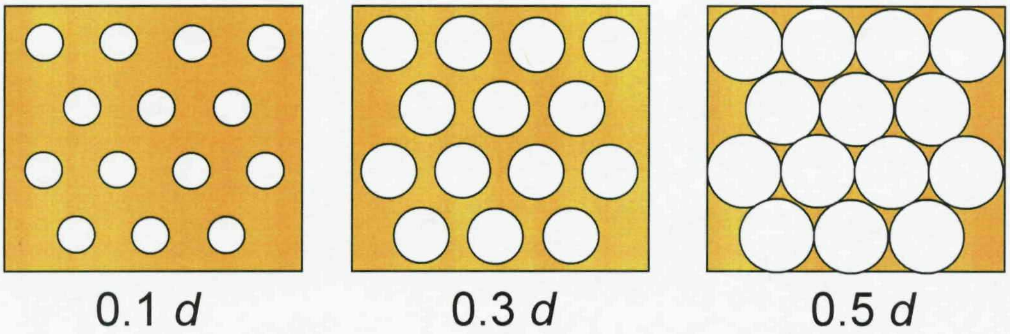

Figure 17 **Schematic diagrams showing the top surface of a gold void structure as the film thickness is increased from 0.1 *d* to 0.5 *d*.**

A typical set of angle resolved (with respect to incident angle) reflectance spectra from a nanostructured film up to 0.4 *d* are shown in Figure 18, and the transition between Bragg plasmons and Mie plasmons can be observed. Bragg modes shift in energy as a function of incident angle, whereas Mie modes do not.

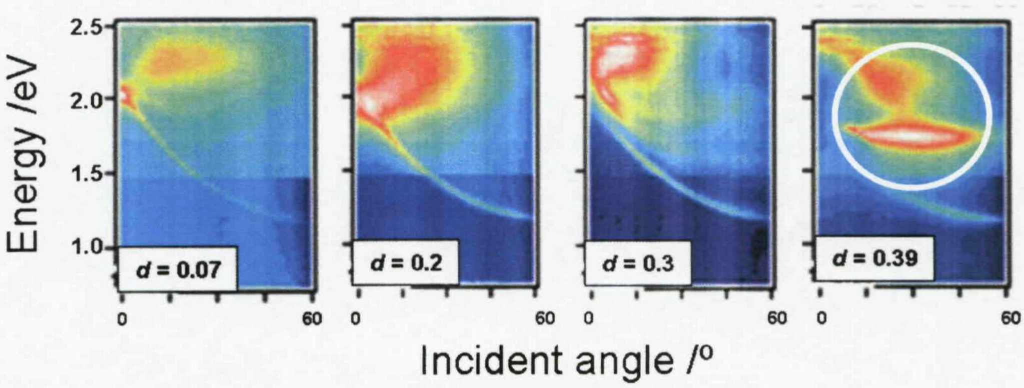

Figure 18 **Reflectance spectra with respect to incident angle for four different film thickness up to *d* = 0.39. The spectra were acquired using a 500 nm substrate.**

The plasmon modes can be seen to correlate with the theoretical plots shown overlaid on Figure 16 i. The mode starts at 2.0 eV and drops to lower energy when the angle of incidence is increased. As the film thickness increases through 0.2 to 0.3 *d*, the mode becomes stronger, as the dishes are more pronounced. However, when the film thickness reaches 0.39 *d*, the Bragg mode seems to split into a higher and lower energy mode, which is indicative of the start of the Mie modes (indicated by the white circle in Figure 18). This mode splitting is the start of a new series of Plasmon modes, all within the theoretical standing waves represented by Mie theory.

4.3.2 Mie Plasmons.

As the film thickness reaches 0.4 *d* the voids can be modeled using Mie scattering. The plasmons are simply standing waves within the cavity, and they have been modeled on *P* and *D* molecular orbitals. Figure 19 shows the theoretical modes for a 500 nm structure with increasing film thickness, along with the top view of the void. It should be noted at this point that the model does not take into consideration that the voids are interconnected by windows between adjacent voids that occur in the real structure, where adjacent spheres touched in the original template.

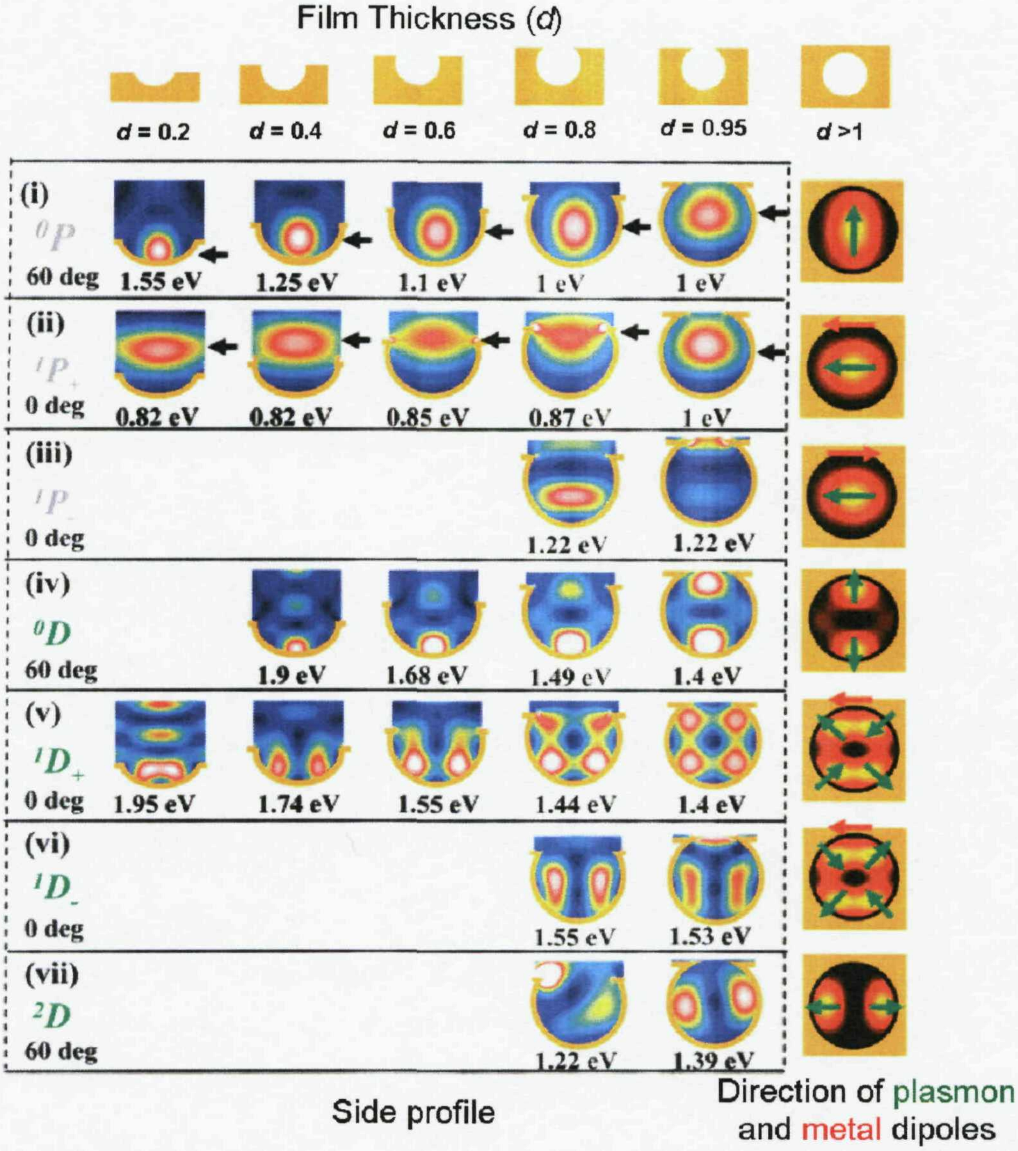

Figure 19 **Theoretical plasmon modes within a 500 nm sample. The film thickness (*d*) is indicated at the top of each column, and the theoretical molecular orbital is given for each row. The column for film thickness d > 1 shows the overall direction of the dipole within the metal (red arrows) and the void itself (green arrows). [14]**

Figure 19 shows the different types of Mie modes predicted to occur within spherical cavities. Each mode is labeled to correspond to bonding (+) and anti-bonding (-) molecular orbital's within the cavity.

The overall movement of electrons within the metal creates a dipole at the rim as indicated by the red arrows in the right hand column in Figure 19. If the plasmon mode is in phase with the metal field, then there a bonding type interaction between the metal and the plasmon, leading to a low energy plasmon mode. The modes that show this in the clearest manner are the ${}^1P_+$ and ${}^1P_-$ modes. When the electric field around the rim and in the void are in phase (${}^1P_+$), or bonding, then the plasmon mode is seen between 0.8 and 1 eV, depending on the film thickness of the sample. However, if the rim and void field are out of phase (${}^1P_-$), or anti-bonding, then the energy of the plasmon mode increases to ~1.2 eV. This increase in energy for anti-bonding modes holds true for each of the plasmon modes.

Further details of how the plasmon modes correlate to SER signals will be given in Chapter 4, however it is felt that the theory of the plasmon modes within the structure will allow for a strong understanding as to which plasmon modes actually give rise to SER signals at varying void diameter, and film thickness.

5 Conclusion.

The sculpted SERS substrates have been modelled upon naturally occurring photonic crystal structures, such as butterfly wings and opals. The manner in which they diffract light has been modelled using Bragg and Mie scattering with excellent correlations. The six fold Bragg scattering is clearly observed at thin films ($d <$ 0.4), and above 0.4 d Mie scattering occurs. The standing waves created within the cavities have successfully been modelled.

6 References

1. Kelf, T., title. 2006, University of Southampton.
2. Ritchie, R.H. Phys. Rev., 1957. **106**: p. 874.
3. Barnes, W.L., A. Dereux, and T.W. Ebbesen. Nature, 2003. **424**: p. 824.
4. Mulvaney, P. Langmuir., 1996. **12**: p. 788.
5. Jackson, J.B. and N.J. Halas. PNAS, 2004. **101**(52): p. 17930.
6. Yin, L., V.K. Vlasko-Vlasov, A. Rydth, J. Pearson, and U. Welp. Appl. Phys. Lett., 2004. **85**(3): p. 467.
7. Halas, N.J. MRS Bulletin, 2005. **30**: p. 362.
8. Wiley, B., Y. Sun, J. Chen, H. Cang, Z.Y. Li, X. Li, and Y. Xia. MRS Bulletin, 2005. **30**: p. 356.
9. Xia, Y. and N.J. Halas. MRS Bulletin, 2005. **30**: p. 338.
10. Coyle, S., M.C. Netti, J.J. Baumberg, M.A. Ghanem, P.R. Birkin, P.N. Bartlett, and D.M. Whittaker. Phys. Rev. Lett., 2001. **87**(17): p. 176801-1.
11. Cole, R.M., J.J. Baumberg, F.J. Garcia de Abajo, S. Mahajan, M. Abdelsalam, and P.N. Bartlett. Nano Letters, 2007. 7(7): p. 2094-2100.
12. Kelf, T.A., Y. Sugawara, R.M. Cole, J.J. Baumberg, M.E. Abdelsalam, S. Cintra, S. Mahajan, A.E. Russell, and P.N. Bartlett. Physical Review B, 2006. **74**(24).
13. Teperik, T.V., V.V. Popov, F.J.G. de Abajo, T.A. Kelf, Y. Sugawara, J.J. Baumberg, M. Abdelsalem, and P.N. Bartlett. Optics Express, 2006. **14**(25): p. 11964-11971.
14. Cole, R.M., Y. Sugawara, J.J. Baumberg, S. Mahajan, M. Abdelsalam, and P.N. Bartlett. Physical Review Letters, 2006. **97**(13).
15. Baumberg, J.J., T.A. Kelf, Y. Sugawara, S. Cintra, M.E. Abdelsalam, P.N. Bartlett, and A.E. Russell. Nano Letters, 2005. **5**(11): p. 2262-2267.
16. Kelf, T.A., Y. Sugawara, J.J. Baumberg, M. Abdelsalam, and P.N. Bartlett. Physical Review Letters, 2005. **95**(11).
17. Bartlett, P.N., J.J. Baumberg, S. Coyle, and M.E. Abdelsalam. Faraday Discussions, 2004. **125**: p. 117-132.

18. http://www.farmfak.uu.se/farm/farmfyskem-web/instrumentation/saxs.shtml.

19. Teperik, T.V., V.V. Popov, and F.J.G. de Abajo. Phys. Rev. B., 2004. **69**: p. 155402.

20. Westcott, S., J. Jackson, C. Radloff, and N.J. Halas. Phys. Rev. B., 2002. **66**: p. 155431.

21. http://www.ece.rice.edu/halas/index.html.

22. Kelf, T.A., Y. Sugawara, J.J. Baumberg, M. Adbelsalem, S. Cintra, P.N. Bartlett, and A.E. Russell. Phys. Rev. Lett. **Submitted**.

23. Abdelsalam, M.E., P.N. Bartlett, J.J. Baumberg, S. Cintra, T.A. Kelf, and A.E. Russell. Electrochemistry Communications, 2005. **7**(7): p. 740-744.

Chapter Four: SERS from Gold Nanostructures.

1 Introduction.

Gold is known as one of the coinage metals and has very similar properties to Silver and Copper which are the most common metals for SERS substrates. This is due to the altered electronic configuration of these d^9 metals, where the configuration becomes s^1 d^{10}. The single electron within the s orbital lies at a lower energy to that of the electrons within the full d orbital and therefore the electron is more easily excitable and surface plasmons are more easily generated on these metals.

The most commonly used substrates made by Van Duyne [1-3], Tian [4, 5] and others [6-8], presented in Chapter 1, all possess optical properties which give rise to surface plasmons. However none of these substrates are as readily tuneable as those discussed in this thesis. The ability to grade the film thickness on the substrates, and hence alter their plasmonics properties sets our substrates apart from other surfaces. The aim of this chapter is to develop an understanding of how the surface plasmons on the sculpted gold surfaces correlate with the SER signals obtained, and to determine which modes are responsible for the enhancements.

In my MPhil thesis work I showed that the diameter of the sphere sizes in the template had a large effect on the SERS enhancement seen [9, 10]. Figure 1 shows the SERS intensities from varying different diameter size voids and film heights of sculpted gold surfaces, with 633 nm excitation.

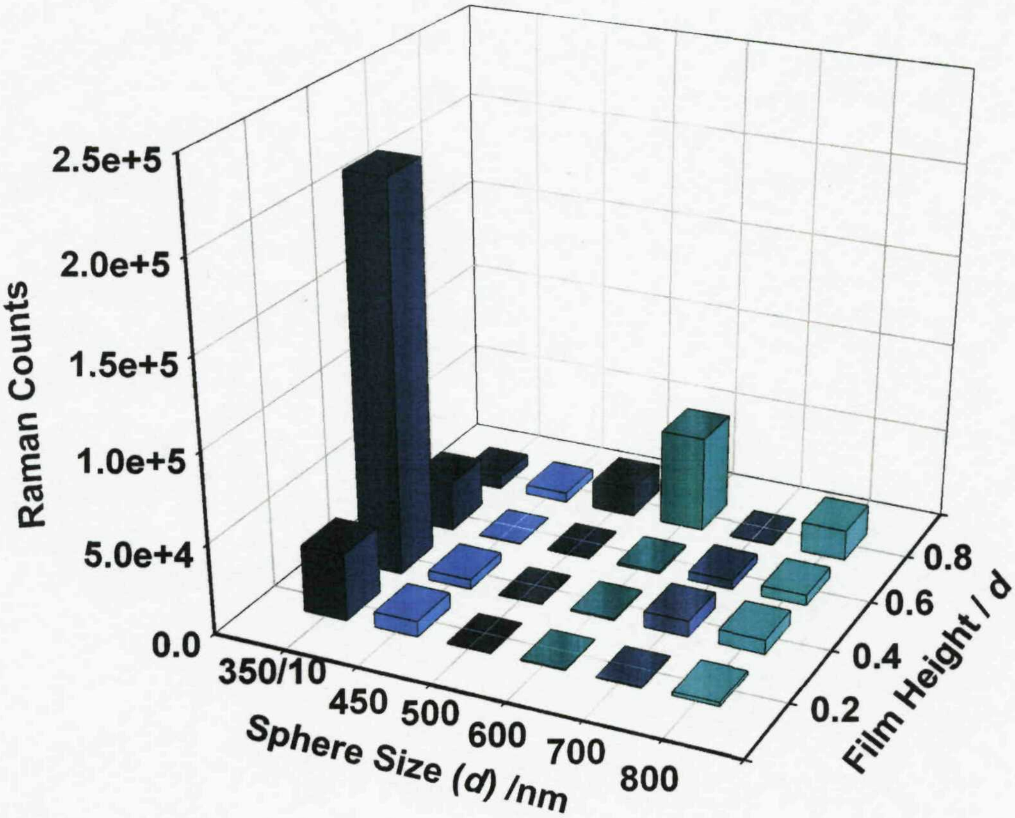

Figure 1 **Peak intensity of the 1571 cm^{-1} band in the SERS spectrum of adsorbed benzene thiol as a function of the sphere diameter, *d*, and fractional film thickness [9,10]**

To obtain these results the samples were tested for a Raman signal by adsorbing 10 mM Benzene Thiol (BT) onto the surface. Three spectra were taken at each step on the sample and the peak height at 1571 cm^{-1} was measured for each spectrum, and the average was determined. Although this result showed that the 350 nm sample gave the greatest enhancement, no theoretical reasons were proposed. Therefore further work was required to establish the origins of the variation in enhancement of the tuneable nature of the sculpted substrates; and to extend the study more excitation wavelengths to determine generality.

Using the comprehensive understanding of the optical properties of the structures that have been developed since the initial SER spectra were obtained, and were discussed in Chpater 3, a more thorough discussion of the origins of the SERS enhancements will be presented. To restrict the number of variables a single probe molecule was chosen for all the studies. BT was chosen due to its strong polarisability, and the fact that the thiol forms a strong bond with gold creating monolayer coverage of the molecule within ~30 minutes of the substrate being submerged in a 10 mM solution.

A typical SERS spectrum of BT adsorbed on a gold substrate from10 mM BT, in ethanol, is shown in Figure 2, the peak assignments are given in Table 1.

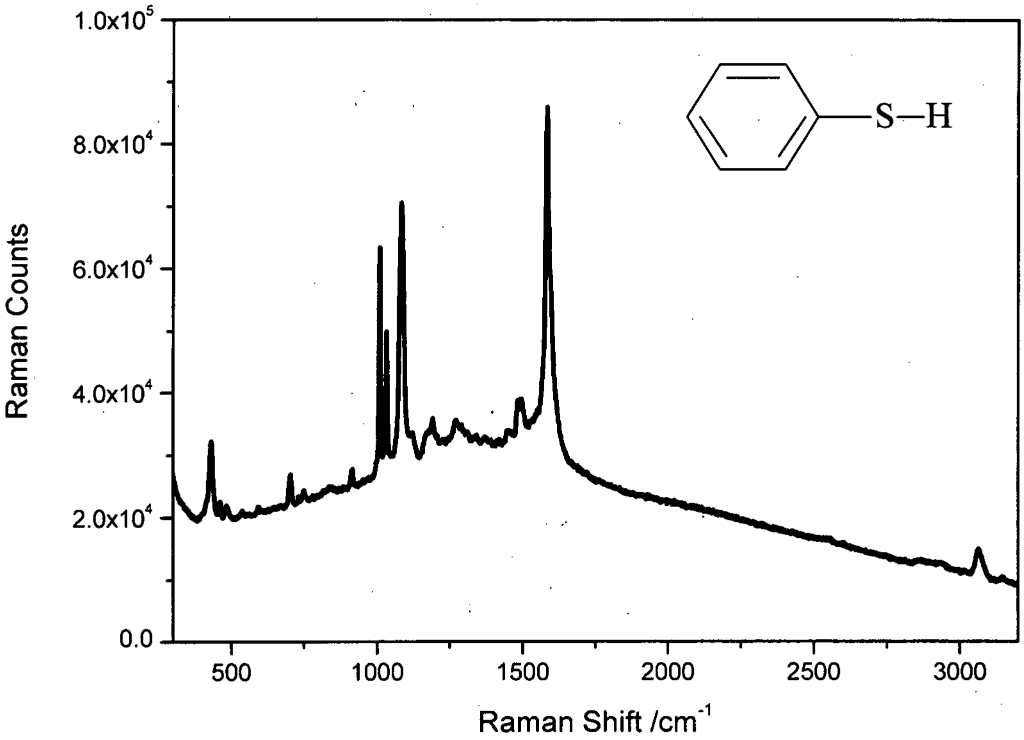

Figure 2 **SER spectrum of 10 mM BT adsorbed onto a nanostructured gold surface, collected with a single 10 s accumulation with 633 nm excitation at 2 mW with a Renishaw Raman 2000 system.**

Table 1 **Assignment of the SERS peaks for benzene thiol on structured gold.**

SERS peak (cm^{-1})	Assignment[a]
3055	a_1, υ(C – H)
1571	a_1, υ(C – C – C)
1471	a_1, υ(C – C)
1177	a_1, υ(C – H)
1071	a_1, υ(C – C – C) and υ(C – S)
1021	a_1, υ(C – H)
996	a_1, υ(C – C – C)
689	a_1, υ(C – C – C) and υ(C – S)
416	a_1, υ(C – C – C) and υ(C – S)

[a] Assigned on the basis of Han et al.[11]

All samples presented within this chapter were graded in film thickness, which is achieved simply by raising the template out of the plating solution when depositing the metal, as explained in Chapter 2. SEM images for several steps on a 600 nm template sample are shown in Figure 3.

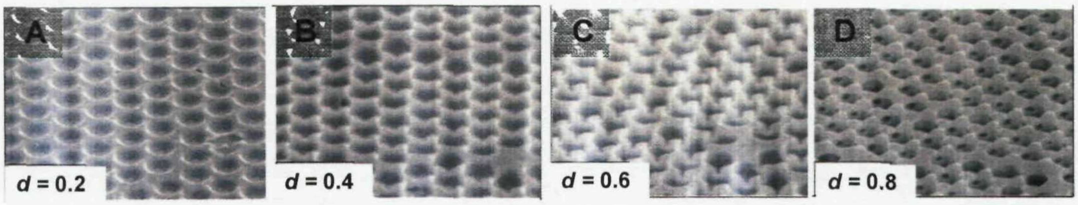

Figure 3 **SEM images of four film thicknesses on a 600 nm void sample. (A) ~0.2 *d*, (B) 0.4 *d*, (C) 0.6 *d* and (D) 0.8 *d*. Each image was acquired from a JOEL 5910 SEM, with a stage tilt angle of 30°, and a magnification of 10,000.**

Figure 3A shows a film that is 0.2 *d*, the film has a relatively large area between the dishes (the top surface area) at this film height, whereas when the film increases to 0.4 *d* (Fig 3B), the area between the voids has decreased, and the voids are now interconnected at the point where the spheres originally touched. As the film thickness increases (figures 3 C & D) the voids begin to close over again. However, even at thicknesses close to 1.0 *d* the film does not close completely over the voids and a chimney is formed above the sphere yielding a pillow like structure top surface. This pattern repeated for all the void sizes investigated; therefore the other full sets of SEM images have not been shown.

2 633 nm excitation on 350 – 800 nm voids.

2.1 Comparison with normal incidence spectroscopy

The position on the stepped sample i.e. thickness, that showed the greatest SERS intensity from each sphere diameter investigated was used to acquire a reflectance spectrum, normal incident reflectance spectroscopy was described in Chapter 2. For each sample the enhancement factor was also calculated to allow direct comparison between each sample.

The enhancement factor shows how much of a SERS signal the substrate is producing. The standard enhancement factor for a SERS substrate seems to be approximately 10^6 as was observed in the original measurements by Fleischmann [12], and enhancements up to 10^8 are common from the substrates which were introduced in Chapter 1 [2, 13-15]. The enhancement factor, EF, can be calculated using the formula [4]:

$$EF = \frac{c_\infty N_A \sigma h I_{\mathrm{surf}}}{R I_{\mathrm{bulk}}}$$

Each EF was calculated using the Raman peak that corresponds to the benzene ring stretching mode of BT at 1571 cm^{-1}. Thus, I_{surf} is the integrated intensity of the band at the surface and I_{bulk} is the integrated intensity in solution of concentration c_∞. N_A is Avogadro's number, σ is the surface area occupied by the adsorbate, R is the roughness factor of the surface (which is the real surface area divided by the geometric surface area) and h (units of μm) is the area illuminated on the surface. It should be noted that accurate enhancement factors could only be calculated for 633 nm excitation wavelength. This is due to lack of fume cupboard facilities at Renishaw Plc, meaning that spectra for 'bulk' benzene thiol could not be measured safely using 785 nm and 830 nm.

The SER spectra corresponding to the greatest enhancements and the equivalent reflectance spectra for each sphere size are summarized in Figure 4.

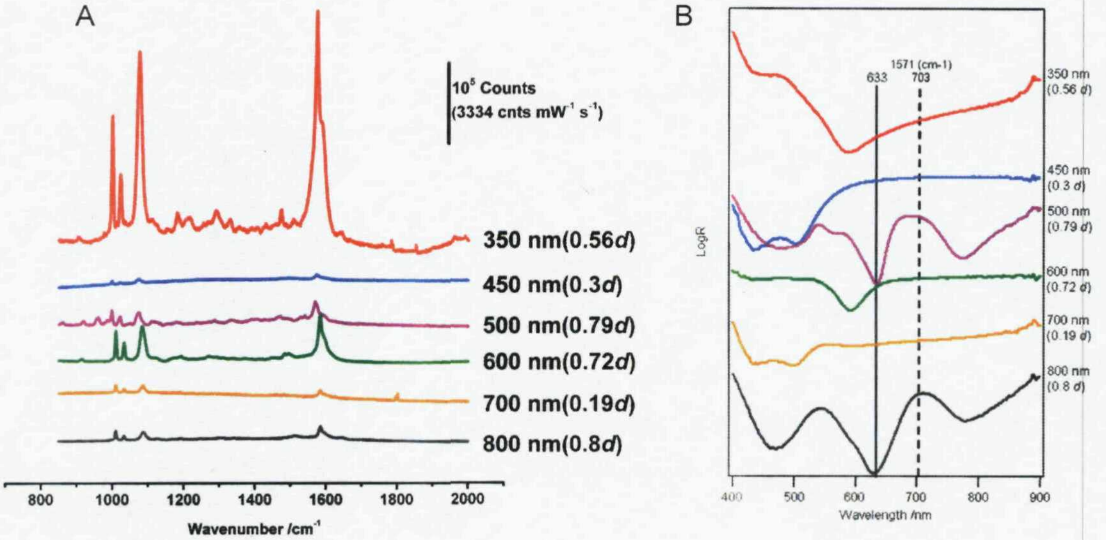

Figure 4 **(A) SERS of benzene thiol adsorbed on sculpted gold substrates as a function of sphere diameter. Note that the substrates were deposited to various thicknesses as indicated in the diagram. The reported spectra represent the largest SERS enhancements for each sphere size. (B) Reflectance spectra corresponding to the sculpted surfaces used in figure 3A.**

From Figure 4A it is clear to see that the SERS spectra obtained from the 350 nm structure is the most intense by a factor of 10, the calculated enhancement factor for this sample was 6.6×10^8. The reflection spectra shown in Figure 3B are taken from the same point as the SERS spectra allowing a direct comparison. The wavelengths corresponding to laser excitation, 633 nm, and Raman scattered photons of the 1571 cm^{-1} SERS peak, 703 nm, are indicated in Figure 4B. The primary difference between the 350 nm sample and the other sphere size is that the reflection spectra is dominated by a very broad band as opposed to the relatively sharp peaks seen for the 800 nm and 500 nm sphere templated samples, for example.

In order to get a more thorough picture of how the SERS substrates perform, SER spectra were collected using three available laser wavelengths (633, 785 and 830 nm). Samples were also analysed using angle resolved reflectance spectroscopy, which led to a full overview of the plasmon resonances occurring on the samples. The SER data will first be presented from the various wavelengths for each sample, followed by a more in depth review of three of the samples with a comparison to the theory presented in Chapter 3.

3 SER data from 633, 785 and 830 nm incident laser excitation.

All work performed using 785 and 830 nm excitation was carried out at Renishaw plc, using an InVia Raman system, and all work done at 633 nm was carried out at Southampton using an RM2000 system, both systems were described in Chapter 2.

The same samples were used for each laser wavelength and the top right hand corner of the slide was used as a point of reference to ensure that the starting points were the same for each experiment.

The results will be shown in order of void size, with all the raw spectra from each laser wavelength being presented in the form of a contour plot, for each sample in the first instance. An example of a contour is shown in Figure 5. Each spectrum is plotted as a function of film height, with the intensity shown in the z axis. The spectra were collected between 200 cm^{-1} and 3200 cm^{-1}, however no peaks occurred above 2000 cm^{-1}, so the data is not shown.

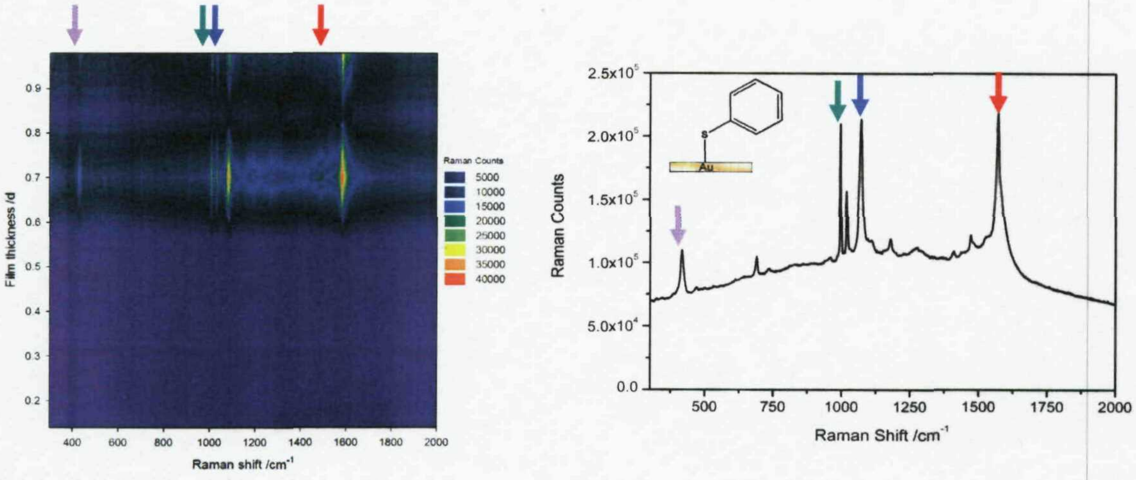

Figure 5 **An example of the type of plots used to present data within this chapter. The peaks within the plot correspond to those in the actual spectra as shown by the coloured arrows. The contour plot shows Raman Shift plotted against film thickness with the SER spectra shown in the z-axis. With purple being the weakest intensity and red the strongest Raman scattering.**

3.1 SERS variability with excitation wavelength.

A comprehensive study of wavelength scanned SERS (WS SERS) done by Van Duyne and colleagues showed that the strongest SER signal was obtained when both the incident an out going Raman photons were both enhanced [16]. This theory agrees very well with the results initially observed and shown in Figure 4.

The SER spectra obtained using 633 nm, 785 nm and 830 nm excitation wavelengths from 10 mM BT adsorbed onto 350 nm, 450 nm, 500 nm, 600 nm, 700 nm and 800 nm diameter void structures are shown in Figure 6. Each contour plot consists of approximately 50 spectra.

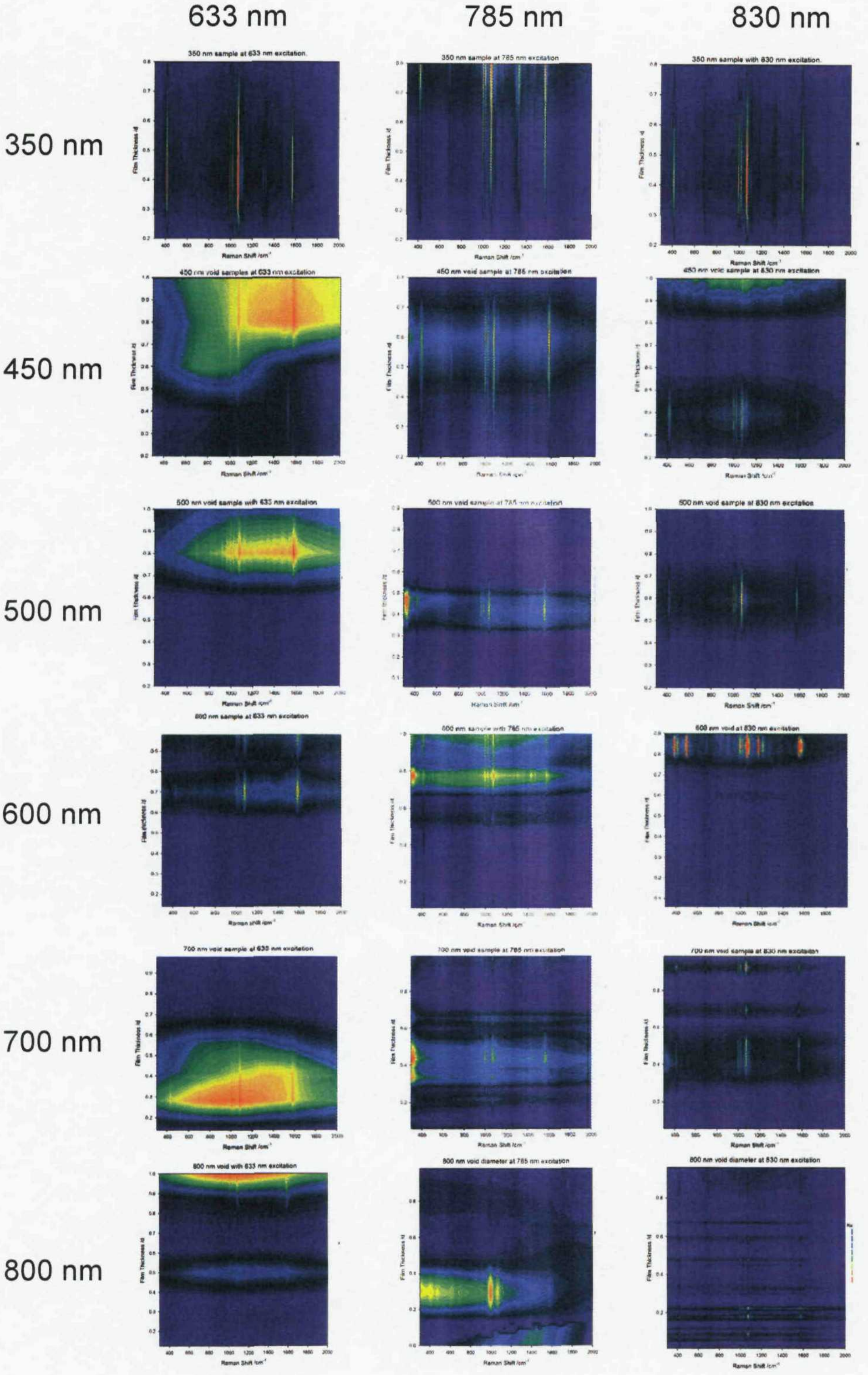

Figure 6 **SER spectra, plotted as a contour plot described in Figure 5, obtained from BT using 350 nm, 450 nm, 500 nm, 600 nm, 700 nm and 800 nm voids, with excitation from a HeNe 633 nm laser, and diode lasers 785 nm and 830 nm. Note that the colour scales vary for each plot, with the greatest intensity being set to red and the weakest to purple**

A very clear observation from the data shown in Figure 6 is that the SERS enhancement varies with incident laser wavelength void diameter and film thickness. Therefore it can be concluded that a single surface morphology (thickness) does not give the greatest enhancement at all excitation wavelengths or for a given sphere diameter.

The theoretical plasmon modes which were described previously, and how they shift with void diameter, have been calculated by a colleague (Robin Cole) in the School of Physics, and are shown in Figure 7.

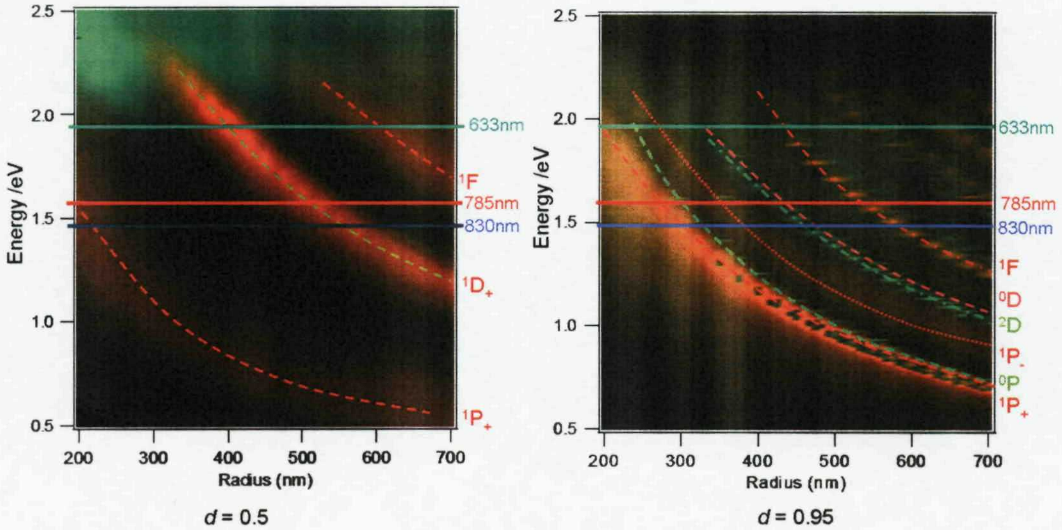

Figure 7 **Plots showing how the plasmon modes are expected to shift with increasing void size. Figure 7A are the expected plasmon energies for a sample at ~0.5 *d*, and figure 7B are the expected plasmon energies for a sample at 0.9 *d*. The dashed lines are labeled as the theoretical plasmon modes (in terms of molecular orbitals, described in Chapter 3). The red dashed lines correspond to 0° incident angles, whereas the green dashed lines correspond to an incident angle of 60°.**

The plots shown in Figure 7 will be used to analyze how the SER signal from each sample correlates with the plasmon modes expected for that sample. However, there are only two film thicknesses accounted for in this figure, therefore a few sample will be looked at more thoroughly with the angular resolved reflectance spectra for the whole sample. Each sample will be discussed individually in the first instance.

3.1.1 350 nm void diameter

The lines which represent the peaks, as shown in Figure 5, within the spectra are all very narrow for the 350 nm template, whereas other size voids have very broad lines showing lower signal to background ratio. However there is also the presence of an extra peak within the spectra at 785 nm excitation. This was assumed to be an impurity at the sample and will be ignored for the purpose of analysis.

Figure 8 shows the curve fitted peak intensity, for the peak at 1571 cm^{-1} as a function of film thickness for each laser wavelength. Note that all data presented in this manner throughout this thesis have been corrected for laser power variations.

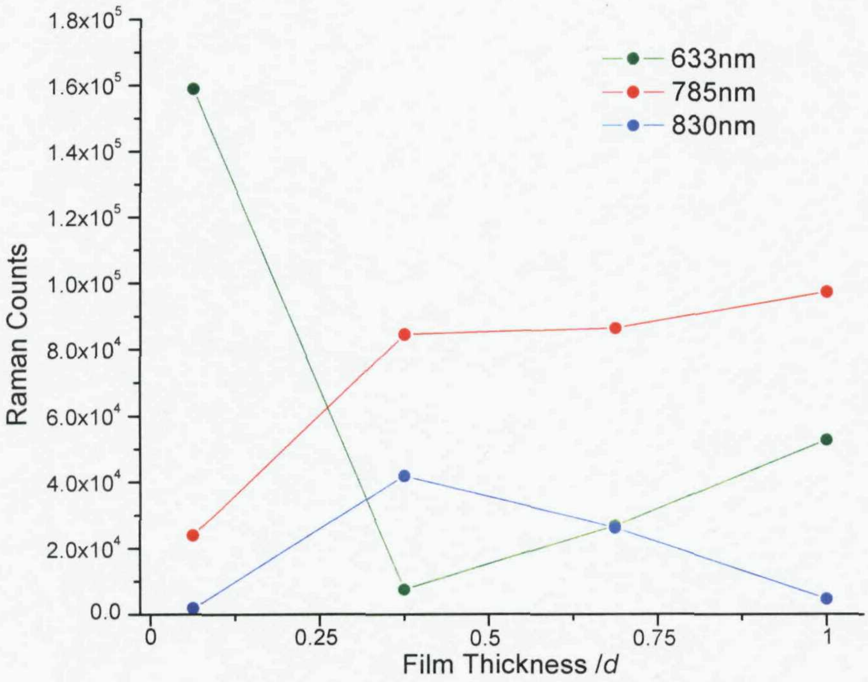

Figure 8 **Comparison of the trends in signal at 1571 cm^{-1} obtained at 633 nm, 785 nm and 830 on a 350 nm void sample.**

The intensity of the 350 nm void surface showed an order of magnitude increase in signal across all wavelengths in comparison to the substrates, which agrees with the earlier study as shown in Figures 1 & 4. The predicted plasmon modes for various sized samples, shown in Figure 7 does not extend to cover this sphere diameter, as the plot is for samples larger than 400 nm in diameter. However, it can be reasonably predicted that the ${}^1P_+$ mode is the dominate plasmon mode within this structure, by looking at the trends in the modes as the sphere diameter decreases. This will be looked at more thoroughly later in this chapter.

3.1.2 450 nm void diameter

For 450 nm there are clearly variations in the positions (thicknesses) that give the greatest intensities for each of the laser wavelengths. At 633 nm excitation the greatest enhancement seems to occur very near 1 *d*, however the broad yellow region in the contour plot implies that the background at this point was also very large. The plots from 785 and 830 nm excitation show clear lines corresponding to peaks for BT, which implies that signal to background ration is much higher.

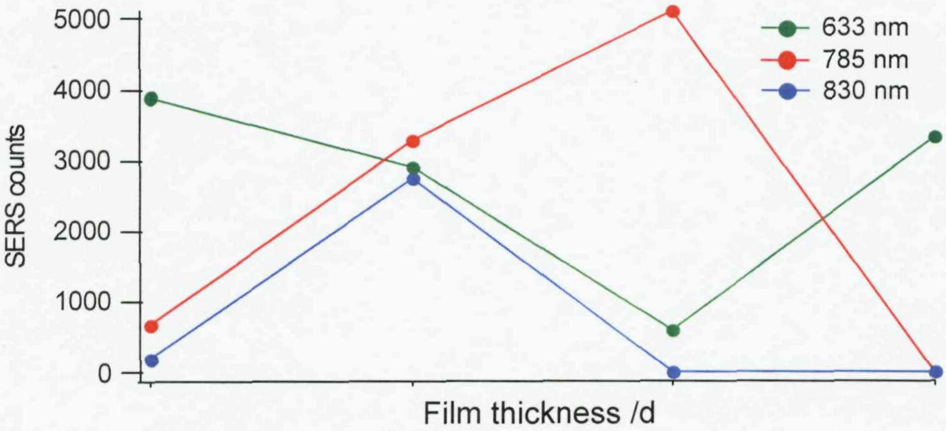

Figure 9 **Comparison of the trends in signal at 1571 cm^{-1} obtained at 633 nm, 785 nm and 830 nm excitation from a 450 nm void sample.**

Figure 9 shows that the peak intensities are all relatively low, at ≤ 5000 counts and there is a relatively large variation in enhancements across the sample. The predicted plasmon modes (Figure 7) for this sample show that the ${}^1P_+$ mode (described in Chapter 3) would give rise to the SER signal at thin films with 830 nm excitation, however for thicker films it is predicted that 633 nm excitation would give rise to the largest SER signal, also corresponding to overlap with the $^{1}P_{+}$ plasmon mode, and this is what is actually observed.

3.1.3 500 nm void diameter

The contour plots shown in Figure 6 for 500 nm show that there are positions within the sample that give intense SERS at each wavelength. However, for this sample the SERS signal is only strong in one place on the sample for each wavelength. Figure 10 shows that the 785 nm and 830 nm excitation wavelengths produced a SER signal that was almost an order of magnitude larger than at 633 nm.

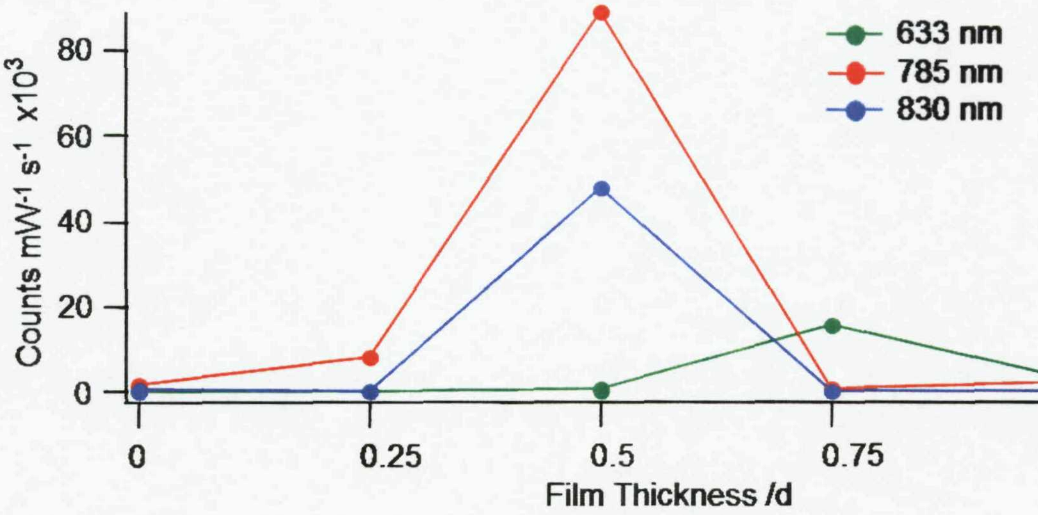

Figure 10 **Comparison of the trends in signal at 1571 cm^{-1} obtained at 633 nm, 785 nm and 830 nm excitation from a 500 nm void sample.**

The point at which the 500 nm sample produces the largest SERS occurs when the film is ½ *d* film thickness. The plots of the plasmon modes shown in Figure 7 are for the two extremes in film thickness, therefore this sample is looked at again in greater detail later within this chapter. Full angular resolved spectra are shown to aid the analysis of which plasmon mode contributes to the SER signal.

3.1.4 600 nm void diameter

The contour plots in Figure 6 showing the raw spectra for a 600 nm void sample show that the enhancement does not reach a maximum until the substrate gets to above ½ d. This is shown more clearly in Figure 11, where the trends for each wavelength are shown as a line graph.

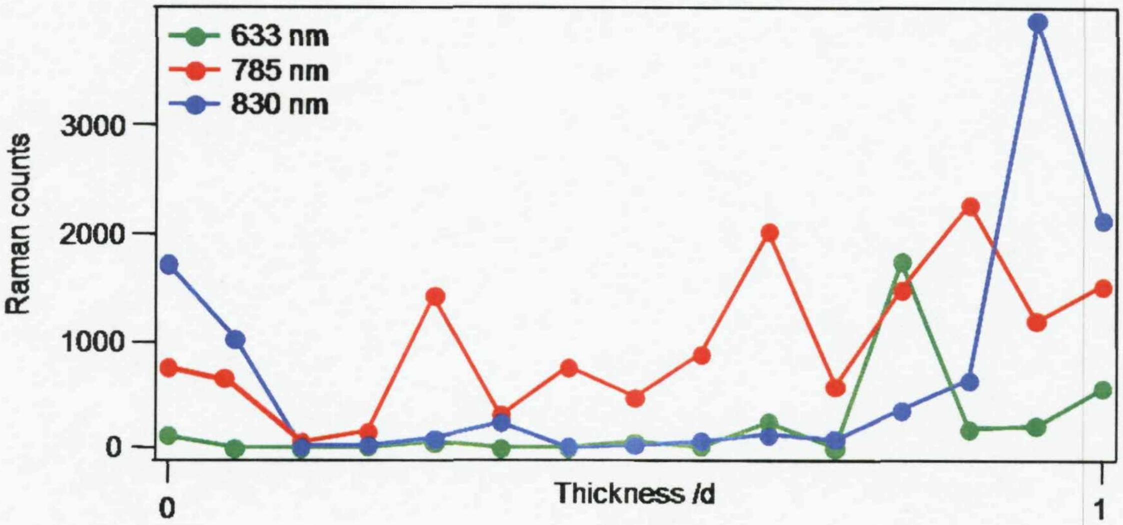

Figure 11 **Comparison of the trends in signal at 1571 cm^{-1} obtained at 633 nm, 785 nm and 830 nm excitation from a 600 nm void sample.**

The trends for the 3 different wavelengths show that the enhancement reaches a maximum at different points on the sample, starting from the higher energy 633 nm excitation to the lowest at 830 nm. This implies that each wavelength is interacting with a different plasmon mode as it decreases in energy. The plasmon modes which contribute to this sample's SER signals are difficult to assign from Figure 7 so this sample will be looked at in more detail later in this chapter.

3.1.5 700 nm & 800 nm void diameters

The SER signal obtained from 633 nm and 785 nm excitation with a 700 nm sample are an order of magnitude lower than that obtained from 830 nm. There is also a large background seen at 633 and 785 nm shown by the areas of greater intensity across a broad range of wavenumbers and film thicknesses, in Figure 6. The origins of this background will be discussed in greater detail in Chapter 5. The SER signal obtained from the 800 nm sample was also of much higher intensity using 830 nm, and the signal was the largest when the film is above 0.7 *d* for 633 nm and under 0.4 *d* for 785 nm or 830 nm. As the cavities of the substrate increase in size there is more interaction between different plasmon modes, as shown in Figure 7, so it is far more complex to determine which plasmon modes are contributing to the SERS for these substrates.

4 Plasmon modes within 350 nm, 500 nm and 600 nm samples.

As previously discussed the samples with void diameters 350 nm, 500 nm and 600 nm showed the most interesting variations in SERS intensity as a function of film thickness and laser wavelength. Therefore these surfaces will be examined in much greater depth in this section of the chapter and the plasmon modes that were introduced in Chapter 3 will be employed to interpret the results.

4.1 350 nm void

Preliminary results from a 350 nm void showed an enhancement that was an order of magnitude higher than any other sample. For the study with multiple laser wavelengths a sample was prepared, which had very fine grading in film thickness, which enables a more thorough examination of the plasmon modes occurring within the structure.

Data was collected from the Renishaw RM2000 for 633 nm, and the Renishaw InVia system for the 785 nm and 830 nm. The curve fitted intensity of the peak at 1571 cm^{-1} of the BT SER spectra from each wavelength is shown in Figure 12.

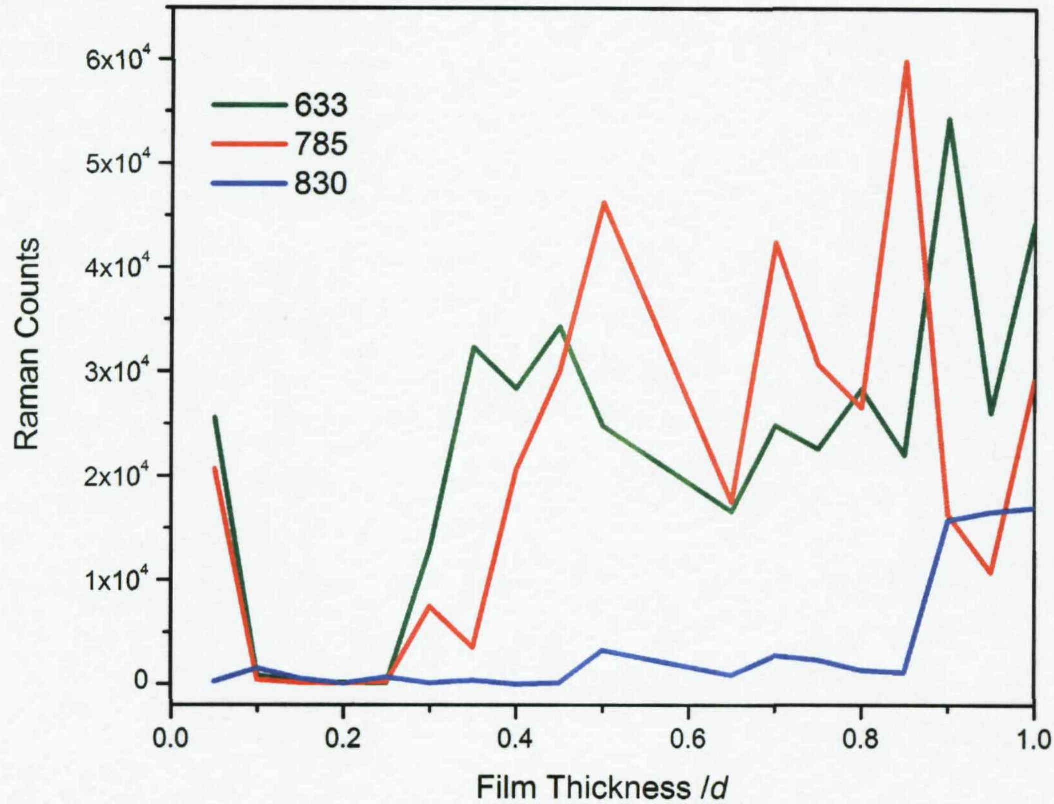

Figure 12 **Comparison of the trends in signal of the Raman spectra of BT, at 633 nm, 785 nm and 830 nm excitation from a 350 nm void sample.**

The enhancement observed using 633 nm and 785 nm excitations are much larger than that at 830 nm, the reason for this becomes clear when the angle resolved reflectance spectrum of this sample is examined, shown in Figure 13.

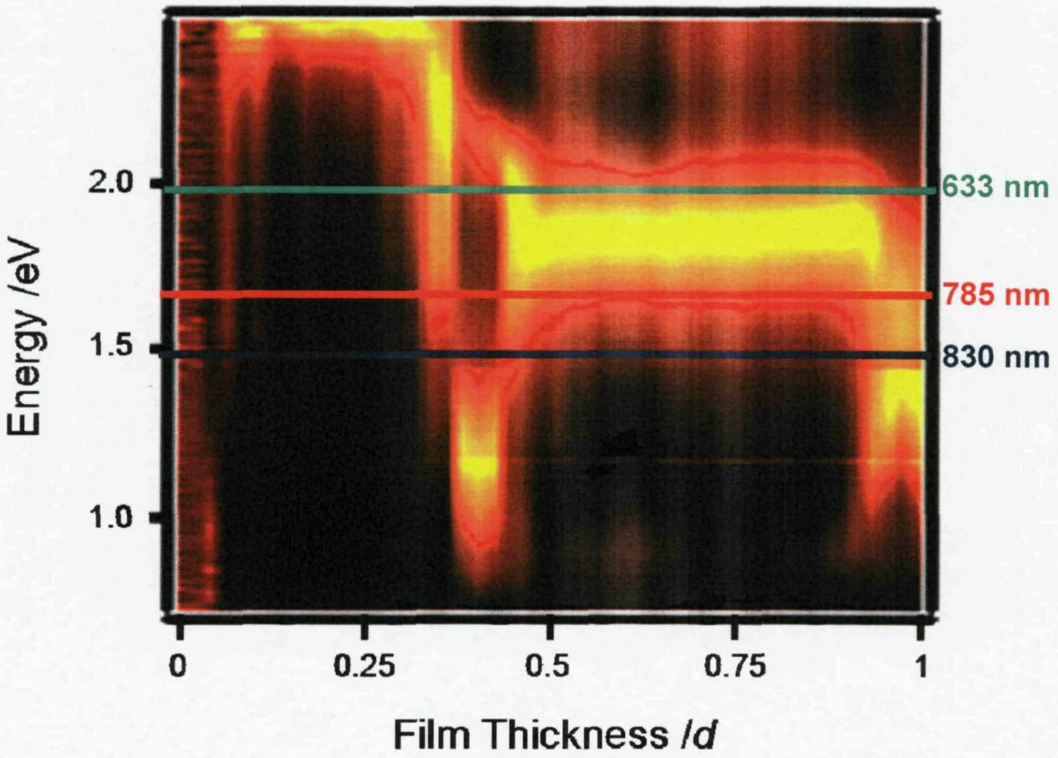

Figure 13 **Angular resolved reflectance spectra as a function of film thickness (*d*) for a 350 nm void sample. The colored lines across the figure show the relative energies for each incident laser wavelength used, the largest intensity reflectance is yellow, and the lowest is black.**

The angle resolved spectra shown in Figure 13, has the white light laser at an incident angle (θ) of 0°, and the reflectance, at this angle, from the sample is plotted as a function of film thickness, the brighter red and yellow areas are points at which there is an absorption/interference of light on the surface, and this indicates the presence of a surface plasmon. The lines indicating the incident laser wavelength are overlaid on the reflectance spectra at the correct energies.

There is an overlap of both the 633 and 785 nm incident laser radiation with the plasmon mode occurring at above ½ *d*. At this point the SERS enhancements, shown in Figure 12, show a clear increase with 633 nm and 785 nm excitation. The signals observed at 633 and 785 nm excitations correspond well with the plasmon modes seen on the surface. As the thickness increases to ~0.4 *d* there is a sharp increase in SER signal, after which the SERS signal remains strong for all remaining thicknesses.

The results from 830 nm excitation are consistent with the plasmon intensities, as the energy of the laser does not correlate with any plasmon intensities until the energy drops, near 1 *d*, at which point there is an increase of 10^4 in the peak intensity of the adsorbed BT.

In order to understand which plasmon modes are causing the SER signal a more thorough representation of the plasmon modes on the sample was required. This was achieved by collecting the reflectance spectra of the sample with varying incident angle. Figure 14 shows the angle resolved reflectance spectra with respect to incident angle, for increasing film thickness for the 350 nm sample.

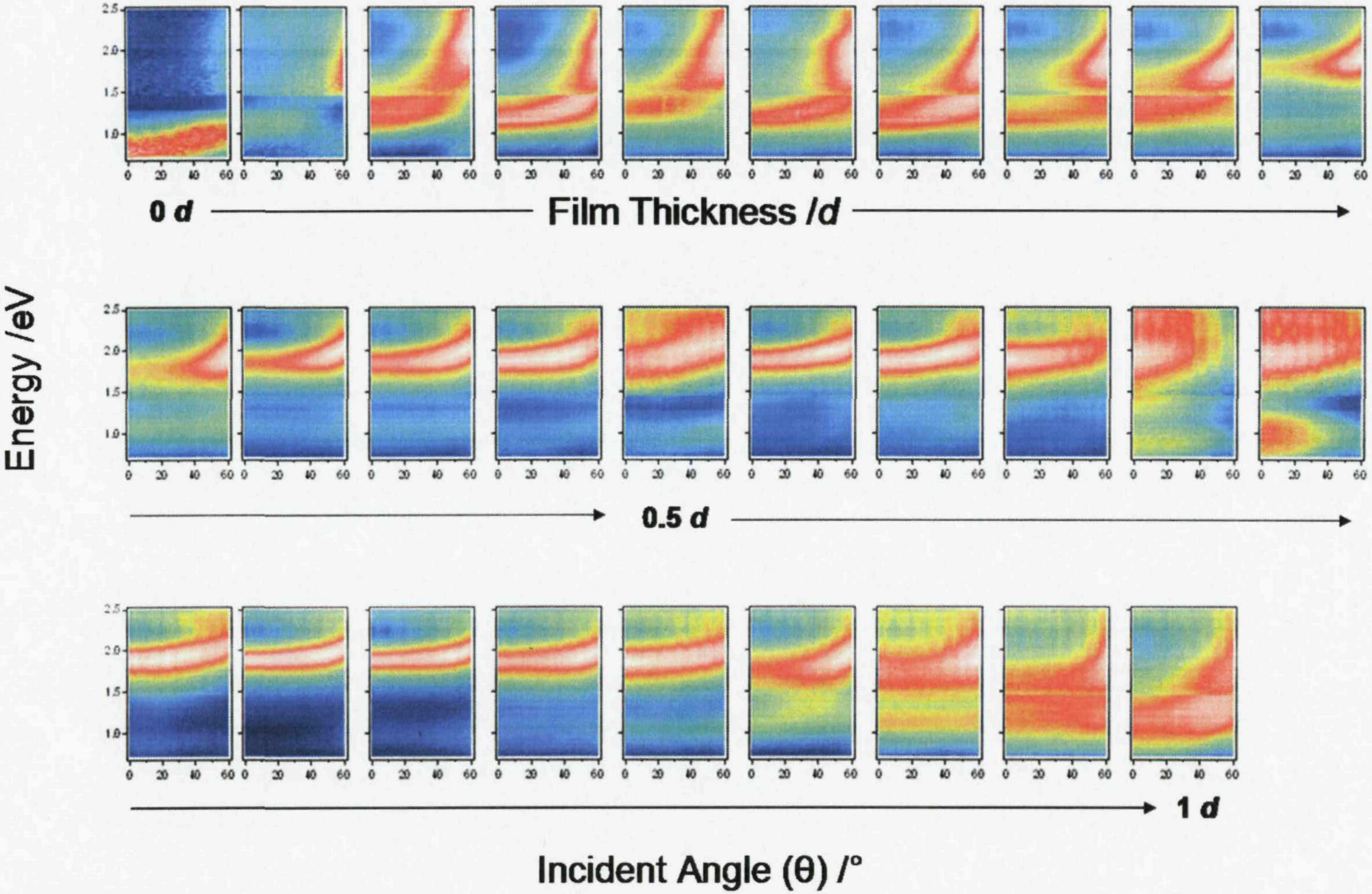

Figure 14 Angular reflectance spectra obtained from a 350 nm sample every 200 microns along the graded film thickness. The spectra are as a function of incident angle, over the range 0 to 60°. Film thickness increases from the top left across the first row, then along the second and third rows to the bottom right plot. Blue is the lowest intensity and red/white the highest intensity.

Each image shown in Figure 14 is taken at one point of the sample and the incident angle (θ) of the white light laser is varied from 0 to 60°. The angle at which the microscope objectives, used for the Raman measurements, collect can easily be calculated from their Numerical Aperture (NA), and can be described, in respect to a point P, as the half-angle θ of the maximum cone of light that can enter or exit the lens. Which is shown pictorially in Figure 15:

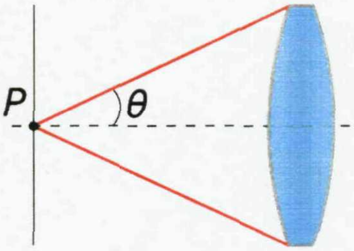

Figure 14 **Schematic showing the cone of light that is sampled when calculating the NA of an objective.**

The *NA* of the x50 objective used in this project is 0.74, this yields a collection angle of ~45°. Therefore any of the absorbance features that are occurring between 0 and 45° in Figure 14 are relevant in terms of SERS enhancements and represent overlap with the incident laser wavelengths.

From the reflectance spectra it is seen that there is one dominant mode, that occurs at when $d \geq 0.4$, seen at ~1.8 eV, which does not shift with incident angle or film thickness. This implies that the mode is not confined within the cavity itself, as it has been shown that the Mie modes within the cavity do shift with film thickness [9]. The enhancements from 633 nm and 785 nm arise from this mode.

There is also a lower energy Bragg mode which occurs at thin films and as the void closes over near 1 *d*. From this it can be assumed that the SER signal seen from the 830 nm excitation comes from the low energy Bragg mode.

The mode that occurs at 1.8 eV, has been modelled [*Robin Cole, School of Physics, University of Southampton*] for films if thicknesses 0.4 *d* and 0.9 *d* yielding theoretical images showing where the plasmon mode is thought to occur. Figure 16 shows the predicted plasmon modes based on the energy seen within the actual spectra.

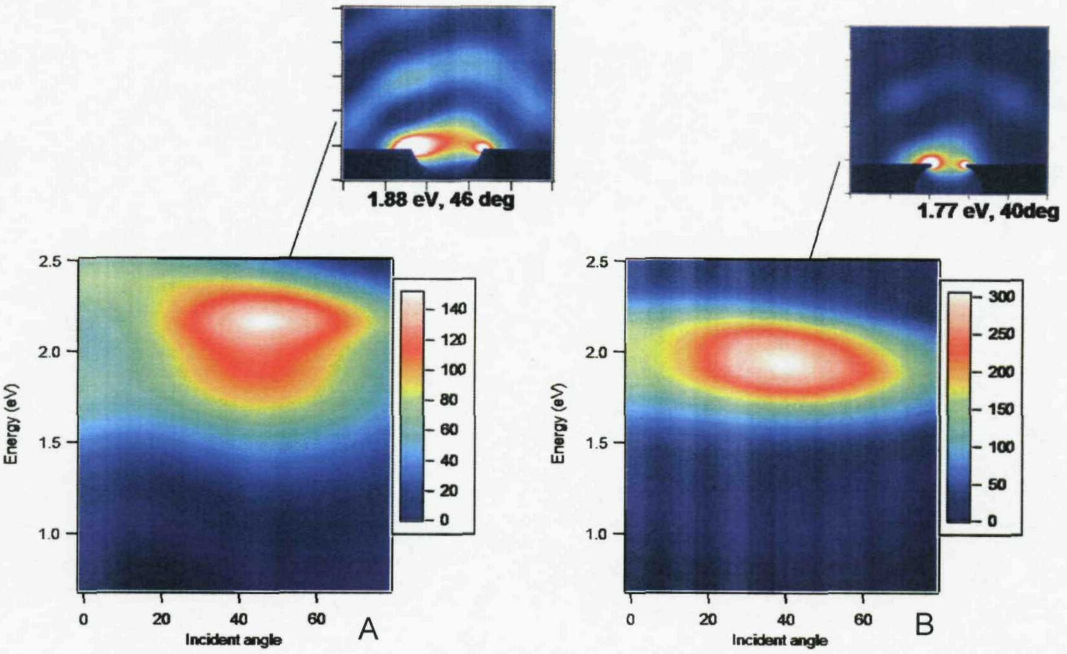

Figure 15 **Theoretical plots of the plasmon mode occurring within a 350 nm diameter void sample at a film thickness ~0.4 *d* (A) and at a thickness of ~0.9 *d* (B).**

Figure 16A shows the theoretical plasmon mode with respect to incident angle at a film thickness of 0.4 *d*, which is where there is an increase in SER signal. The scale has arbitrary units, and simply indicates the strength of the plasmon field. The image offset above the theoretical reflectance spectra is an image of how the plasmon field is thought to be occurring, and shows a side view of the surface at each film thickness indicating how the plasmon field interacts with the top surface of the gold. Figure 16B shows the same set of images as for 16A, except that the predicted field is for a film thickness of 0.9 *d*. These images suggest that the very broad mode around 1.8 eV consists of a plasmon interaction around the rim of the cavity and depending on the thickness of the film it shifts in energy. The 'rim mode' is at a higher energy when the film is thinner; however as the film thickness increases the mode drops to a lower energy. It is thought that this is due to the bonding interaction from within the cavity, as explained below.

There is a charge variation across the metal structures due to the movement of the free electrons, creating a dipole like state across the voids. The surface plasmons also have a dipole like standing wave, and if these two dipoles match then there is a 'bonding' type of interaction, whereas if the dipoles don't match then there is an 'anti-bonding' type of interaction. If there is a bonding or anti-bonding interaction the plasmon energy would shift to lower or higher energies respectively [17].

The plasmon modes within these structures have been modelled on molecular orbitals, as previously described in Chapter 3. The mode that is centred around the rim of the cavity is a ^1P mode, as shown in Figure 17. The ^1P mode is the equivalent of a p_x or p_y orbital, and a ^0P mode modeled on the p_z orbital, with the mode 'sitting' at the base of the cavity.

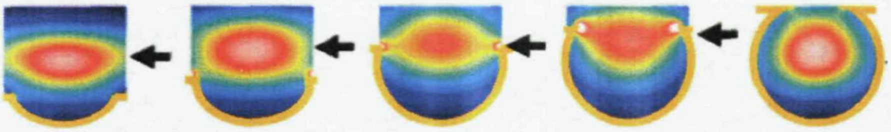

Figure 16 **Computer modeled images showing how the plasmon modes are thought to interact with the rim of the cavities. The images shown are plotted with respect to increasing film thickness, as indicated by the yellow rim around the plasmon field [17].**

The observation that this mode shifts to lower energy as the thickness increases suggest that it consists of a bonding type interaction with the metal, and is therefore given the notation $^1P_+$.

The $^1P_+$ mode is at its strongest at films above ½ *d*, and this would therefore account for why the 785 nm data shows a higher SERS activity at thicker films than 633 nm. Also as the film grows thicker the opening to the void becomes narrower, which would intensify the plasmon mode occurring and would confine the plasmon within the void. This theory accounts for why substrates show a sharp increase in intensity at the very thick end of the sample. This idea is also supported by the work done on colloid plasmon fields. It has been shown since early SERS paper's that as the colloids and nanoparticles become closer then the plasmon field intensity increases and shifts in wavelength. [18, 19].

4.2 500 nm void

In the preliminary study the 500 nm void sample showed a sharp increase in intensity at around ½ *d* but the rest of the substrate seemed relatively inactive. The angular resolved reflectance spectra as a function of *d* is shown for a sample that had 250 μm steps in film thickness is shown in Figure 18. The predicted plasmon modes have been plotted over the top of the image, taken from the paper published by our collaborators in the School of Physics at the University of Southampton [17].

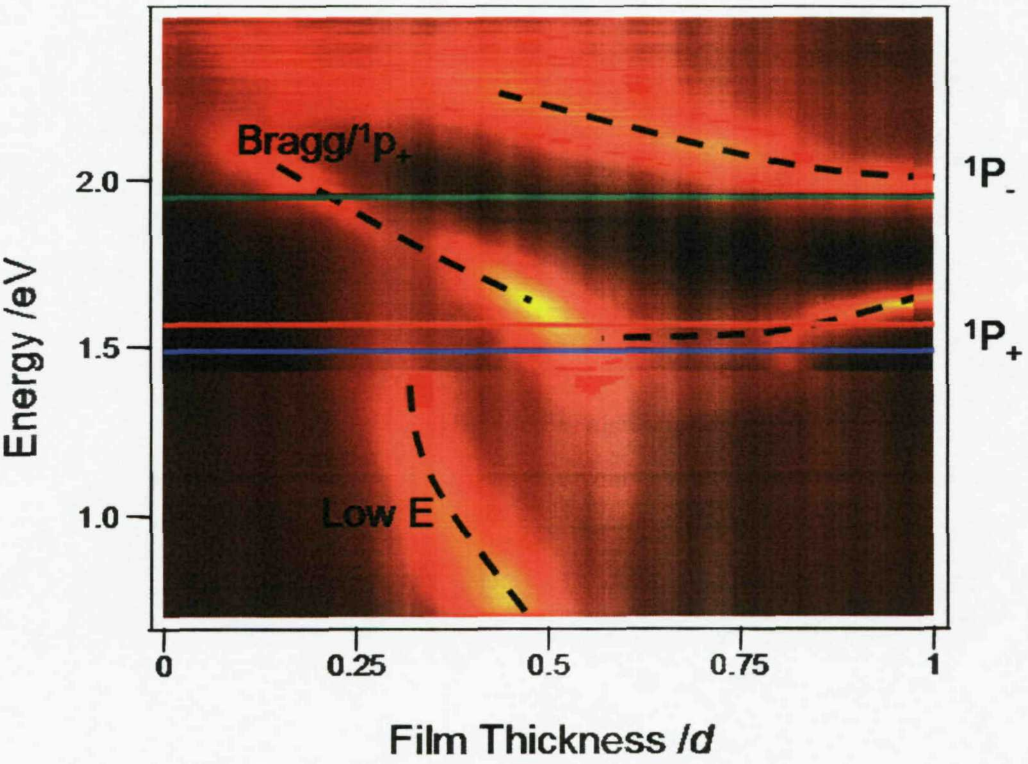

Figure 17 **Angular resolved reflectance spectra as a function of film thickness for a 500 nm void sample. The colored lines across the figure show the relative energies for each incident laser wavelength used.**

The angular resolved spectra for the 500 nm sample show two ^{1}P modes which dominate the spectra. The $^{1}P_{+}$ mode drops to lower energy as the film thickness increases and become the most intense around ½ *d*.

Raman spectra were collected via line maps for 785 nm and 830 nm excitation (the Raman 2000 system did not have a mapping capability, therefore spectra were collected every 250 microns from this system) which were set to collect a spectrum every 10 microns down a finely graded sample. The general trends (an average over 200 micrometers) from the maps along with the 633 nm excitation data are summarised in Figure 17. The 1571 cm^{-1} peak intensities were used for comparison.

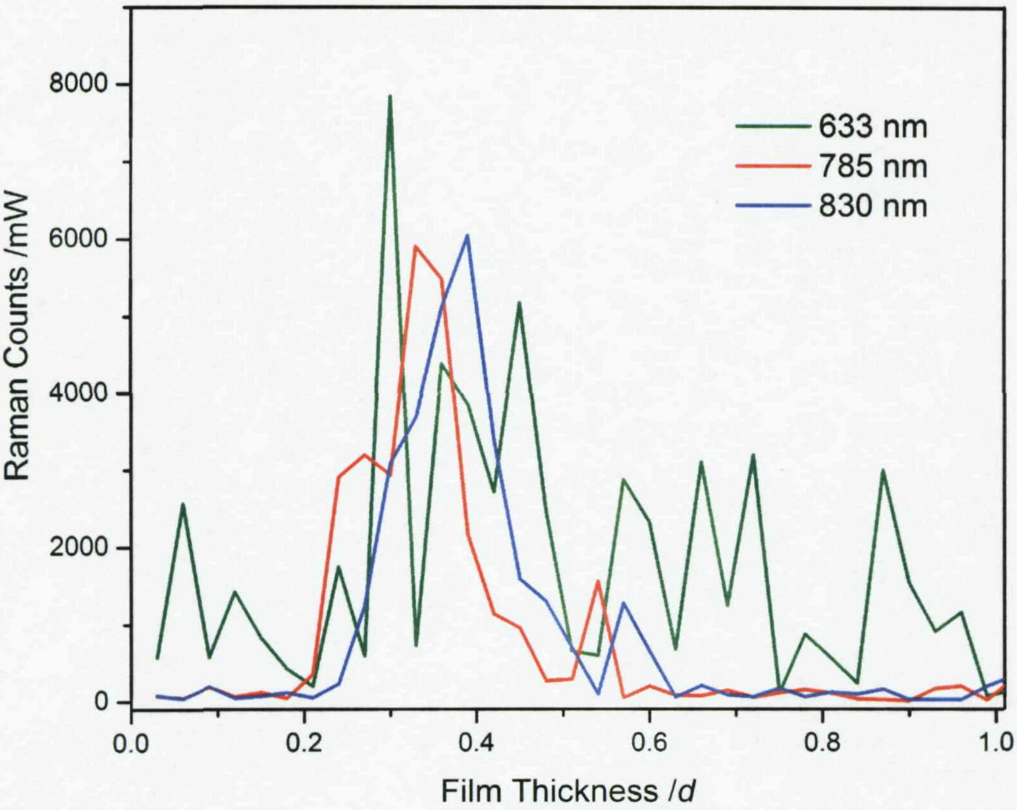

Figure 18 **The trend in signal at 1571 cm^{-1} obtained from a 500 nm structured surface at 633 nm, 785 nm and 830 nm excitation. The sample had a film thickness graded from 0 to 1 *d*.**

There are obvious points of greatest enhancement for each excitation, which shift to increased film thickness with increasing laser excitation energy. Figure 18 gives the theoretical plasmon modes overlaid on the angular reflectance spectra, and from this it is apparent that the SER signals from 785 and 830 nm arise from the $^1P_+$ plasmon mode. The enhancement seen below 0.5 *d* from the 633 nm excitation originally arise from the $^1P_+$, whereas as the sample gets thicker the $^1P_-$ plasmon mode accounts for the enhancement.

There is variability in the SER signal seen at 633 nm excitation, however this became more prominent in the mapped results from 785 and 830 nm excitation where the spectra were collected every 10 micrometers along the sample. The intensity at 1571 cm^{-1} for the two maps is shown in Figure 20.

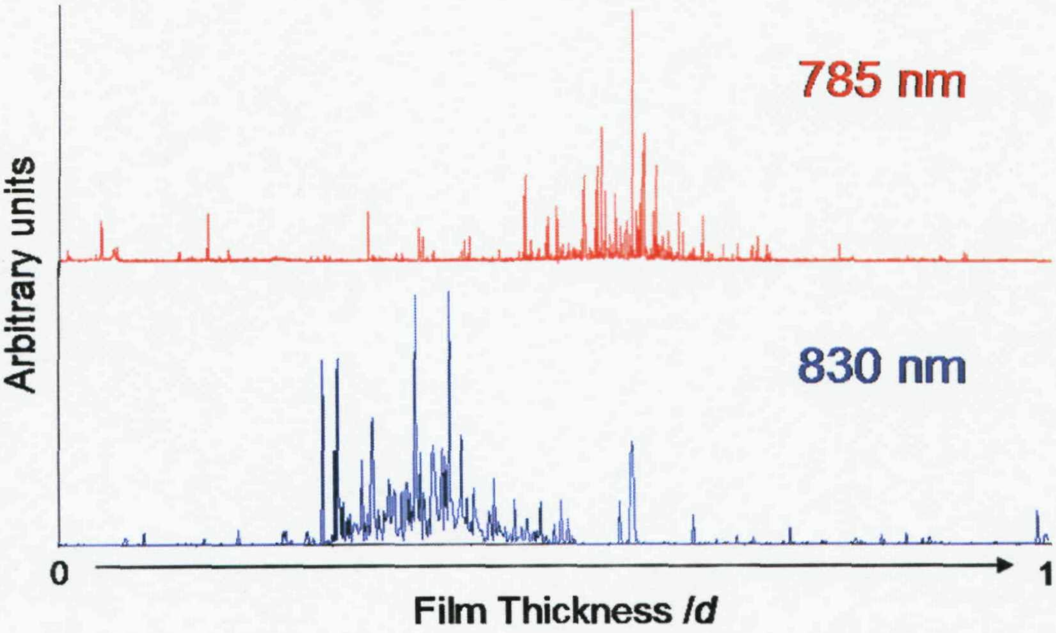

Figure 19 **Intensity at 1571 cm^{-1} from the SER spectra of 10 mM BT adsorbed onto a graded 500 nm void sample. The spectra were collected every 10 μm down the sample, with 785 nm and 830 nm diode lasers on a Renishaw inVia Raman system. Each spectrum was acquired with a single 10 s accumulation.**

The variability is thought to arise from the data being acquired from different combinations of voids. The spot size for the laser can be calculated using the formula:

$$s = \frac{0.61\lambda}{NA}$$

Where λ is the laser wavelength and NA is equal to the numerical aperture of the microscope objective, which is equal to:

$$NA = n \sin\theta$$

The NA of the x50 objective used in this project is 0.74, which leads to theoretical spot sizes of less than 1 micrometer. Therefore in some cases the spot could be focussed on one entire void, whereas in others it could be centred over the edge of 3 or 4 voids.

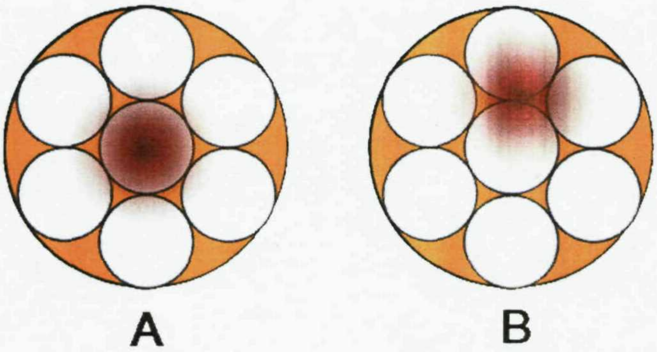

Figure 20 **Schematic image showing how a < 1 µm laser spot hits either an entire 500 nm void (A) or a series of void rims (B). The red spot indicates the laser spot, and the orange area between the voids indicates the top surface of the structure.**

The images shown in Figure 21 are for a film thickness of ½ *d* which corresponds to the area of increased enhancement for the 500 nm sample. From these simplistic diagrams it is predicted that the SER signal would be obtained when multiple voids are sampled, due to multiple Mie plasmon modes within the cavity being generated, however this needs further investigation.

The final sample that has been looked at in greater depth was a 600 nm void sample, as this gave a strong enhancement in initial studies [10], and the sample seemed to show a large variation in the position on the sample that gave the strongest enhancement.

4.3 600 nm void

The work carried out by other research groups, has shown that when the laser wavelength is approximately the same size as the particle under investigation the strongest SERS signal is observed [3, 9, 20-23]. Therefore the 600 nm void sample was predicted to give the greatest enhancement at 633 nm in initial studies. The plasmon modes start to become more complex when the void gets bigger than 600 nm. A sample that was fully graded in terms of film thickness was prepared in order to monitor the plasmon modes within the structure, and correlate them to the SERS signals.

Given that the plasmon modes are more complex for this sample the reflectance spectra, with respect to both incident angle and film thickness, along with the peak intensity at 1571 cm^{-1} for each laser wavelength (normalised for laser power) and SEM images, from each position measured, are shown in Figure 22.

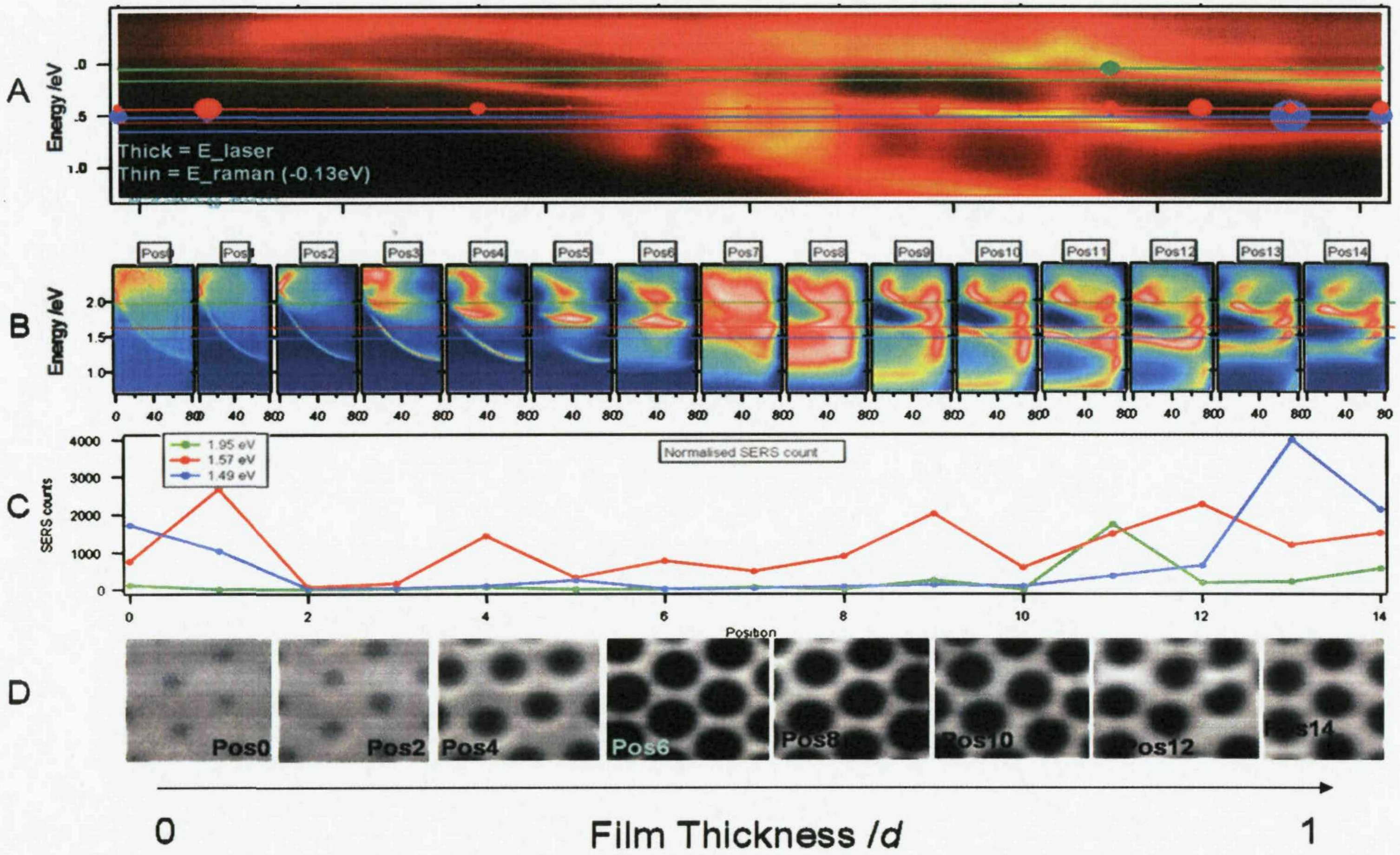

Figure 22 Summary of reflectance and SER spectra from a 600 nm void sample. (A) Shows the angular resolved reflectance spectra with respect to film thickness, overlaid is the excitation lines for 633 nm (green), 785 nm (red) and 830 nm (blue), with the SERS intensity of the BT 1571 cm^{-1} peak. (B) Shows the angular resolved spectra as a function of incident angle at each point that the SERS spectra were obtained. (C) Shows the peak intensity of BT with varying film thickness. (D) Shows the SEM image of the point where the SER spectra would have been obtained.

The results summarised in Figure 22 combine all the techniques used to monitor the performance of the substrates in terms of both SER signal and reflection spectroscopy. The spectra in Figure 22A is the angle resolved reflectance spectra of the 600 nm graded sample, with the incident laser excitation energies overlaid (633 nm – green, 785 nm – red and 830 nm blue) with the Raman signal at that point showed as a spot on the line (the larger the spot, the higher the intensity). The energy of the Raman band of BT at 1571 cm^{-1} is also plotted as the thinner colour coded line for each excitation energy. The spectra in Figure 22B are the reflection spectra, with respect to incident angle, for each point that the SER signal was collected from. The incident laser wavelengths are overlaid as per Figure 22A. Figure 22C shows the intensity of the 1571 cm^{-1} band of BT plotted as a function of film thickness for each laser wavelength. The SEM images in Figure 22D show the film thickness for every other position that SERS and reflection spectra were collected from.

At film thicknesses $d \leq 0.4$, there is little SERS activity from 633 nm excitation. However, there is enhancement from both 785 nm and 830 nm at thin films. There is an overlap between the lower energy laser excitation energies and the Bragg plasmon mode at high angles of incidence, for thin films which is not observed in Figure 22A, but accounts for the SER signals at low film thicknesses.

As the film reaches thicknesses of $0.4 < d < 0.6$ there is a very broad plasmon mode that shows up within both Figures 22A & B, however, it is also clear to see that there is very little SERS signal at these film thicknesses. On first inspection this looks like an anomalous result, given the correlation between SER signal and plasmon modes seen up until this point in the thesis. This result can be explained by referring back to Figure 7 where the theoretical modes can be seen for increasing sphere diameter. At 600 nm diameter the *D* plasmon mode is beginning to be observed, and theory suggests that the *D* plasmon mode occurs in the centre of the void. The molecules being detected in this study are adsorbed to the surface of the gold, therefore nothing is being excited by the plasmon that is localised within the centre of the cavity. Recent work on solution phase SERS has shown an enhancement at these film thicknesses, which arise from the *D* plasmon mode [17].

At film thicknesses of $d > 0.6$ enhancements in signal are seen from all excitation energies. At 633 nm there is a sharp increase in energy as the laser energy matches that of the higher energy $^1P_-$ mode, however, no further signal is observed as the laser did not couple with any other plasmon modes. The strongest enhancement is seen at approximately ¾ *d* film thickness from 830 nm excitation. This is where the laser is coupled to another plasmon mode, which according to the theory in Figure 7 is the $^1P_+$ mode, which has dominated the enhancements seen from other substrates.

The overall enhancements seen from this substrate, correlate with the results from previous samples, where the largest enhancement arises from coupling to the $^1P_+$ plasmon mode, which is that centred on the rim of the void.

5 Conclusions.

The aim from this chapter was to asses which plasmon modes accounted for the observed SERS enhancements, this was achieved through a systematic study of different surface morphologies and incident laser wavelengths. The results presented within this chapter have shown that no one surface performs the same for all the different laser wavelengths used.

The enhancement factors from the sculpted SERS substrate, at 633 nm, reached 6.6 x10^8 which compares very favourably with those seen from the surfaces discussed in Chapter 1. It can reasonably be predicted that the enhancement factors are of a similar magnitude at different laser wavelengths from the peak intensities. The enhancement arises from a coupling of light into a plasmon mode within the structure, and the strongest enhancement is seen when both the ingoing light and outgoing Raman scattering overlaps with a plasmon mode (as shown in Figure 4) and illustrated schematically in Figure 23.

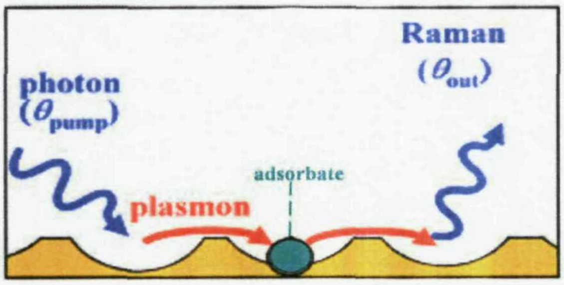

Figure 21 **Theory of ingoing light and outgoing Raman shift interacting with a plasmon to produce a SER signal, shown schematically.**

This supports the theory put forward by Van Duyne and co workers [16] and reported in our paper [9], and emphasises the importance of the electromagnetic theory of SERS.

Many different plasmon modes have been introduced through the course of this thesis; however the most prominent in terms of SERS enhancement is the $^1P_+$ mode which is a type of Bragg plasmon and it continually interacts with the excitation laser wavelengths used in this project. The theoretical model of the mode was shown in Figure 17, it is localised around the edge of the dish and couples light into the void. The fact that the Rim seems to account for the large enhancements observed, a large variability within one sample is observed when a tightly focussed laser spot is used and the data is collected at many closely spaces places on the substrate surface. This was shown to be dependent on whether the laser spot is hitting one single void or multiple voids.

The ability to understand the plasmon modes occurring within the substrates allows precise control over SER signals obtained. This, in turn, allows a surface to be produced, using the controlled electrochemical templating technique, to give the best performance at any given laser wavelength, or even molecular excitation. This is a unique property of any SERS substrate currently used in research.

6 References.

1. Van Duyne, R.P., J.C. Hulteen, and D.A. Treichel. J. Chem. Phys., 1993. **99**: p. 2101.
2. Hulteen, J.C., D.A. Treichel, M.T. Smith, M.L. Duval, T.R. Jenson, and R.P. Van Duyne. J. Phys. Chem. B, 1999. **103**: p. 3854.
3. Haes, A.J., C.L. Haynes, A.D. McFarland, G.C. Schatz, R.P. Van Duyne, and S. Zou. MRS Bulletin, 2005. **30**: p. 368.
4. Tian, Z., B. Ren, and D. Wu. J. Phys. Chem. B, 2002. **106**(37): p. 9463.
5. Tian, Z., Z.L. Yang, B. Ren, J. Li, Y. Zhang, X.F. Lin, J. Hu, and D. Wu. Faraday Discuss., 2005. **132**(13).
6. Mulvaney, S.P., L. He, M.J. Natan, and C.D. Keating. J. Raman. Spectrosc., 2003. **34**: p. 163.
7. Faulds, K., R.E. Littleford, D. Graham, G. Dent, and W.E. Smith. Anal. Chem., 2004. **76**: p. 592.
8. Kneipp, K., Y. Wang, H. Kneipp, I. Itzkan, L.T. Perelman, R.R. Dasari, and M.S. Feld. Phys. Rev. Lett., 1997. **78**(1667).
9. Cintra, S., M.E. Abdelsalam, P.N. Bartlett, J.J. Baumberg, T.A. Kelf, Y. Sugawara, and A.E. Russell. Faraday Discussions, 2006. **132**: p. 191-199.
10. Pelfrey, S., title, in *Chemistry*. 2005, University of Southampton.
11. Su, K.H., S. Durant, J.M. Steele, Y. Xiong, C. Sun, and X. Zhang. Journal of Physical Chemistry B, 2006. **110**(9): p. 3964-3968.
12. Fleischmann, M., P.J. Hendra, and A.J. McQuillan. Chemical Physics Letters, 1974. **26**(2): p. 163-166.
13. Hicks, E.M., O. Lyandres, W.P. Hall, S.L. Zou, M.R. Glucksberg, and R.P. Van Duyne. Journal of Physical Chemistry C, 2007. **111**(11): p. 4116-4124.
14. Kneipp, K., H. Kneipp, R. Manoharan, E.B. Hanlon, I. Itzkan, R.R. Dasari, and M.S. Feld. Applied Spectroscopy, 1998. **52**(12): p. 1493-1497.
15. Kulakovich, O.S., N.D. Strekal, V.F. Oskirko, S.A. Maskevich, S.V. Gaponenko, M.I. Samoilovich, and A.V. Gur'yanov, in *Photonic Crystal*

Materials and Nanostructures, R.M. DeLaRue, et al., Editors. 2004. p. 517-522.

16. McFarland, A.D., M.A. Young, J.A. Dieringer, and R.P. Van Duyne. Journal of Physical Chemistry B, 2005. **109**(22): p. 11279-11285.
17. Mahajan, S., R.M. Cole, P. Bartlett, J. Baumberg, and A. Russell. PCCP, 2008. **In Press**.
18. Zhong, Z.Y., S. Patskovskyy, P. Bouvrette, J.H.T. Luong, and A. Gedanken. Journal of Physical Chemistry B, 2004. **108**(13): p. 4046-4052.
19. Ghosh, S.K. and T. Pal. Chem. Rev., 2007. **107**: p. 4797.
20. Perney, N.M.B., J.J. Baumberg, M.E. Zoorob, M.D.B. Charlton, S. Mahnkopf, and C.M. Netti. Optics Express, 2006. **14**(2): p. 847-857.
21. Halas, N. Mrs Bulletin, 2005. **30**(5): p. 362-367.
22. Mahajan, S., M. Abdelsalam, Y. Suguwara, S. Cintra, A. Russell, J. Baumberg, and P. Bartlett. Physical Chemistry Chemical Physics, 2007. **9**(1): p. 104-109.
23. Perney, N.M.B., F.J.G. de Abajo, J.J. Baumberg, A. Tang, M.C. Netti, M.D.B. Charlton, and M.E. Zoorob. Physical Review B, 2007. **76**.

Chapter Five Substrate Properties

1 Introduction

The substrates that are commonly used for SERS, introduced in Chapter 1, all show enhancements of over 10^4 in Raman signals [1-8], however limited data has been presented which shows the reproducibility of the signals, and how stable each of the surfaces are. The nanostructured gold substrate, presented in this thesis, will be discussed in terms of reproducibility, robustness and shelf life in this Chapter.

2 Reproducibility and robustness

The lack of reproducibility obtained in terms of SERS signal and the surface morphology of substrates has hampered the progress of SERS over the last three decades. As will be illustrated in this chapter, sculpted substrates, however, have broken through this barrier.

2.1 Reproducibility in substrate morphology and SER signal.

The surface morphology of sculpted substrates can be controlled and tuned by selecting the appropriate sphere sizes, and the method used to assemble the polystyrene spheres yields well ordered close packed structures. The sphere sizes used for the original template have thus far been chosen to be within the range of visible light to near infra-red (300 to 900 nm) as this produced substrates with plasmon modes that overlapped with the lasers available.

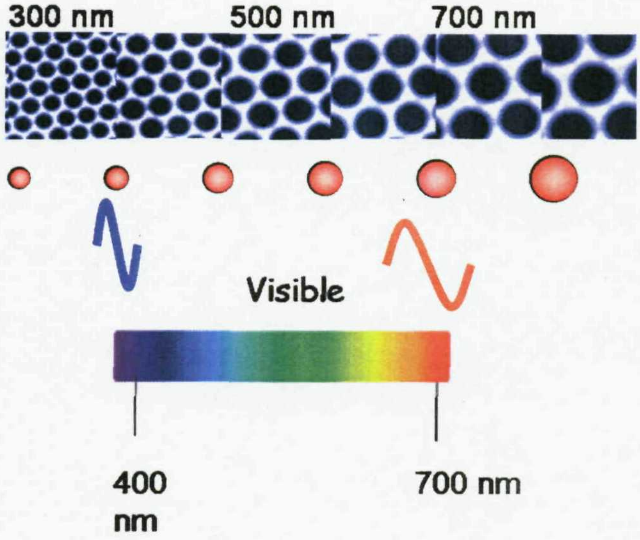

Figure 1 **SEM images of gold void structures sized 300 to 800 nm, each image shown was acquired with an accelerating voltage of 30 keV, with a magnification of 10,000.**

Figure 1 shows SEM images of a series of different sized samples at the same film thickness. The surfaces are very well ordered with a hexagonally close packed structure, which shows that the surface morphology is highly reproducible across a wide variety of template sizes. The film structure with varying film thickness was shown in Chapter 4 and is reproduced for each sphere diameter.

Not only is there reproducibility between substrate structures, the spectra obtained from them are also highly reproducible across a substrate sample. To demonstrate this over 60 spectra were collected from a 600 nm ¾ *d* sculpted SERS substrate, at different spots across the sample (the total area of uniform thickness was 250 μm x 5000 μm), and there was a variability of less than 10% when over 60 spectra were collected from this area. The spectra are shown in Figure 2.

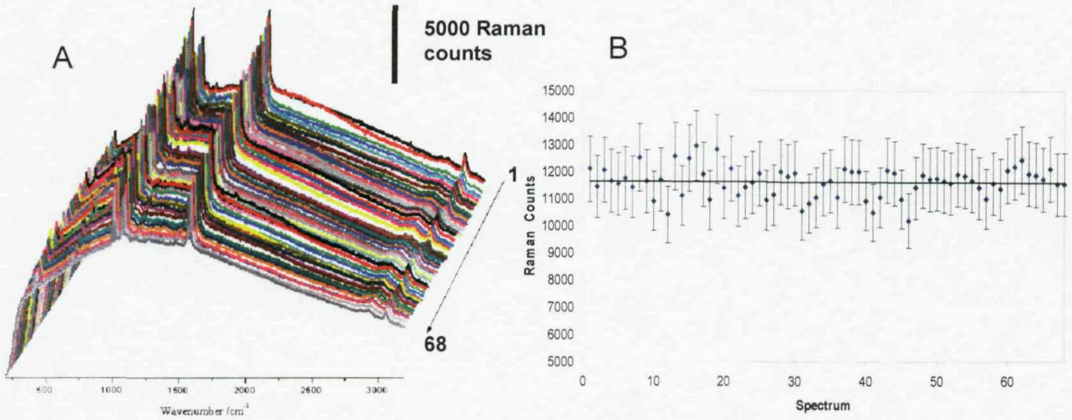

Figure 2 **68 SERS spectra obtained every 100 µm from 10 mM Benzene Thiol on a 600 nm ¾ *d* sample. (A) Each spectrum was obtained using 633 nm excitation in conjunction with a Renishaw Raman 2000 system. A single 10 s extended scan was used for the acquisition of each spectrum. (B) Peak height of each spectrum with the 10% standard deviation of the height.**

The standard deviation from these spectra was calculated by analyzing the peak intensity at 1021 cm^{-1}. The SERS signal is also reproduced when different substrates with the same structure are compared, the typical standard deviation between samples was found to be less than 13% [9].

2.2 Reusability

Uniquely compared to all the other SERS substrates previously discussed it is possible for each sculpted SERS substrate to be used more than once; however the original molecule must first be desorbed from the surface. In the case of thiols, which have been predominantly used in this project, the metal - thiol bond was broken by electrochemical cycling.

The thiol covered substrate was used as the working electrode in a standard three electrode cell, as discussed in Chapter 2, in 0.5 M KOH. The potential was cycled between -0.1 and -0.9V vs. SCE at 0.1 mV s^{-1}. Each substrate was cycled twice and Figure 3 shows the first and second cyclic voltammograms.

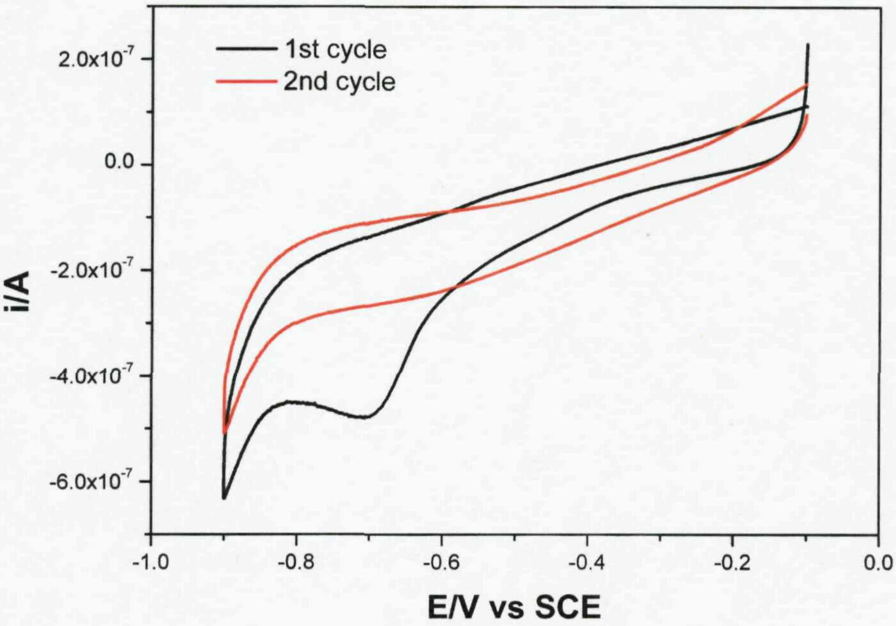

Figure 3 **First and Second sweeps showing the desorption of benzene thiol, in 0.5 M KOH, from a 600 nm templated structure, grown to ¾ *d*.**

The black line CV in Figure 3 shows the first sweep of the substrate a reduction peak is seen at -0.7 V vs. SCE. The Au – S bond is broken at this potential and the negative current shows the irreversible desorption of the benzene thiol. The red line shows the second scan, which has a lack of the reduction of the adsorbate, and is hence showing a clean gold surface.

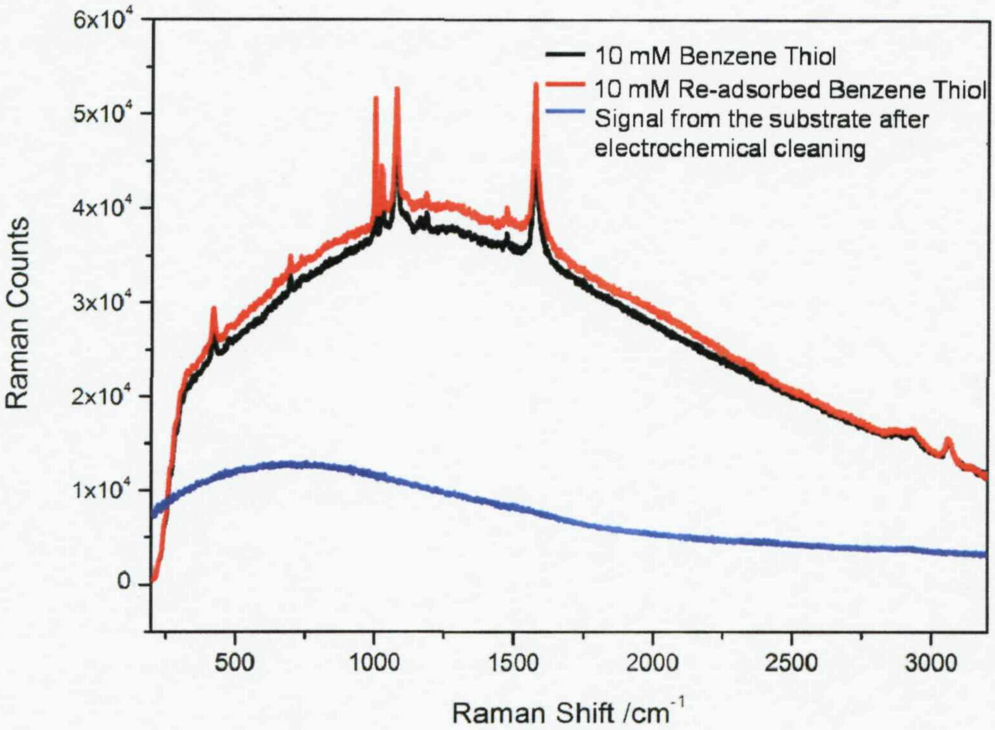

Figure 4 **SER spectra obtained from 10 mM BT adsorbed to a 600 nm ¾ d sculpted substrate (Black line), the spectrum obtained from the same substrate after the surface was electrochemically cleaned (Blue line), and the spectrum of a fresh layer of 10 mM BT after the surface had been cleaned. All spectra were recorded using a single 10 s accumulation with an extended scan, using 633 nm excitation.**

When the species had been desorbed, the surfaces were then sonicated in DMF for 30 minutes, to ensure all trace impurities had been removed before reusing them. Storing the substrates after they have been used is also not a problem, as shown in the following section.

2.3 Shelf life

The standard shelf life of other SERS substrates is still problematic, with the longest shelf life seen to date being < 9months [10]. In contrast the shelf life for gold sculpted substrates is at least 3 years. Figure 5 shows a spectrum obtained from a 600 nm ¾ *d* substrate in January 2005, and a spectrum obtained from the same substrate in January 2008. The substrate was simply electrochemically cleaned as described above and sonicated in DMF followed by re-exposure to a 10 mM BT solution to re-form the monolayer and the spectra are shown in Figure 5.

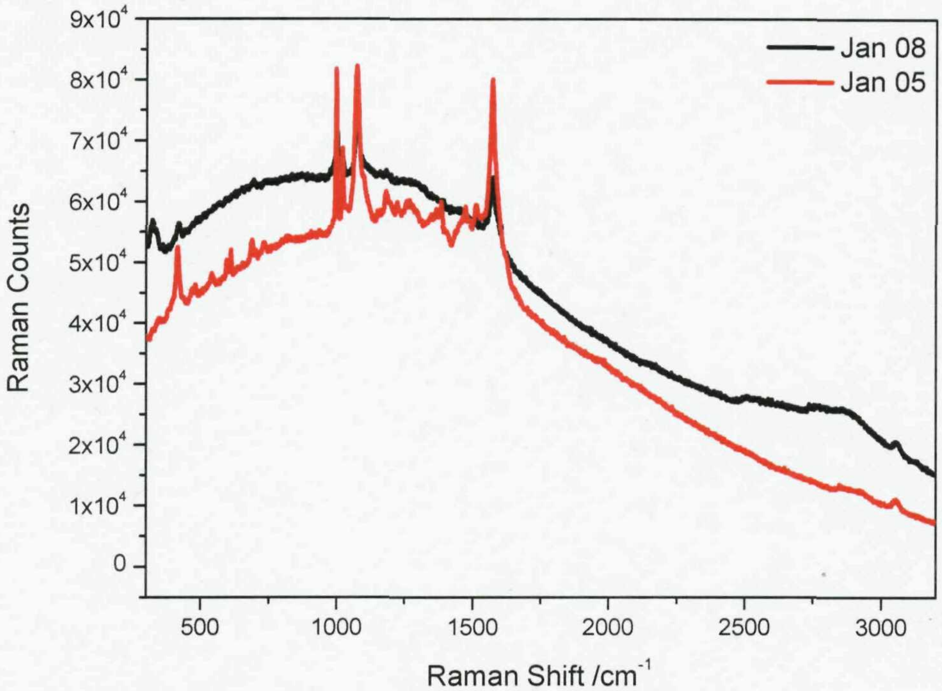

Figure 5 **SER spectra obtained from a 10 mM solution of BT adsorbed onto a 600 nm ¾ *d* nanostructured substrate. The red spectrum was obtained in Jan 2005 and the black spectrum was acquired in Jan 2008, both with a single 10 s extended scan accumulation on a Renishaw Raman 2000 system.**

A slight decrease in the peak intensity of the BT peaks was found after 3 years. However, the remarkable finding is that there is still a signal observed after 3 years, and therefore it has surpassed any other reported SERS substrates' shelf life.

2.4 Signal variation with sample imperfections.

The surface roughness factor of a substrate is defined as the ratio of the real surface area to the geometrical surface area, which can easily be calculated for our gold substrates by performing a cyclic voltammagram (CV) in acidic solution and measuring the charge associated with stripping of a monolayer of oxide. Figure 6 shows the comparison between a sculpted SERS substrate and flat gold, which enables the calculation of the roughness factor.

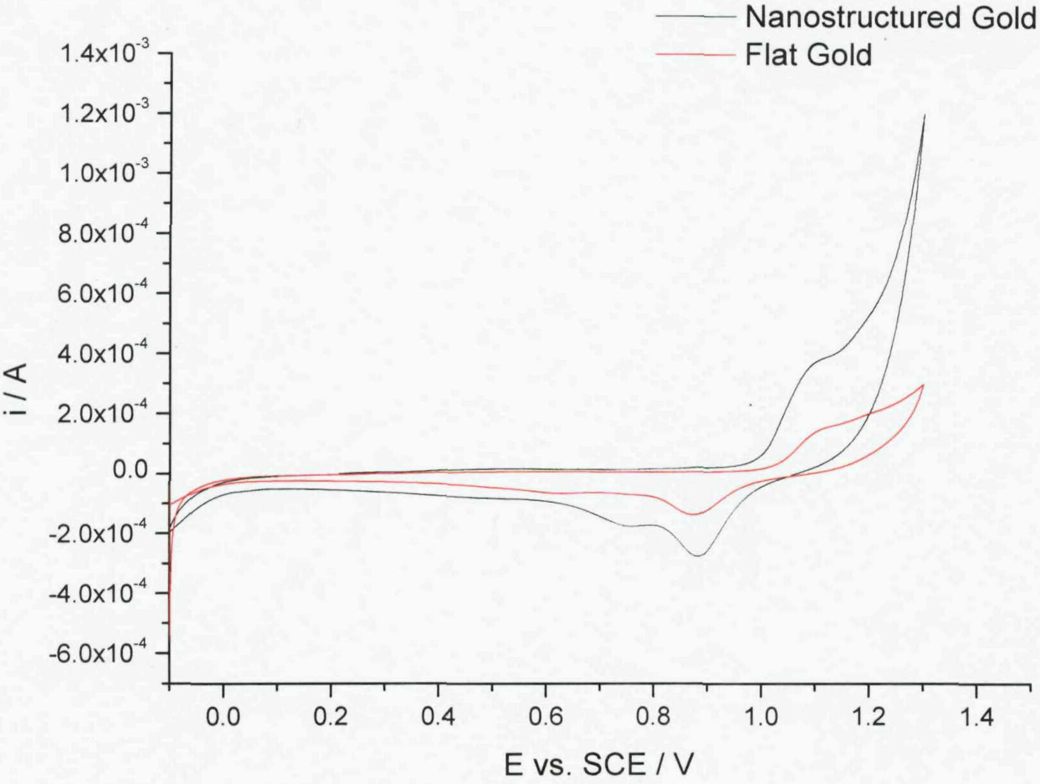

Figure 6 **Cyclic Voltammograms of a nanostructured gold electrode and an evaporated gold electrode, vs SCE in 50 mM H_2SO_4. Potential scanned from –0.1 to 1.5 vs SCE / V. Scan rate of 100 mVs^{-1}. The nanostructure was made from a 600 nm sphere size template with a film height of 300 nm (½D). The shaded region indicates the location of the oxide region used for calculation.**

The increase in surface area was found to be 1.6 and can be fully accounted for by the shape of the sculpted surface. From this value, it can be assumed that the metal is relatively smooth, however there will always be areas where the plating fails slightly, and slightly rough surfaces are observed. However, by comparison the roughness factor of an ORC roughened substrate such as those used originally by Fleischmann was found to be 10, which is due to the irregularity at the atomic scale on the substrate.

It was thought that the slight imperfections found on the sculpted surfaces, from the plating technique, could account for the slightly anomalously shaped backgrounds within the spectra. The theory was tested by choosing these rough areas, with aid of Renishaw's SEM-Structural Chemical Analyser (SEM-SCA).

2.4.1 Experimental set up

Each sample had a monolayer of BT adsorbed onto the surface prior to measurements taking place, and Raman spectra were collected before the SEM images were collected, preventing damage to the adsorbate layer by the electron beam and the build up of carbon on the surface. The Raman spectra were acquired using a 785 nm diode laser, which was introduced into the SEM chamber through a fibre optic cable. It was possible to correlate SEM images and the image acquired whilst looking through the top of the fibre optic arm using features on the surface, as shown in Figure 7.

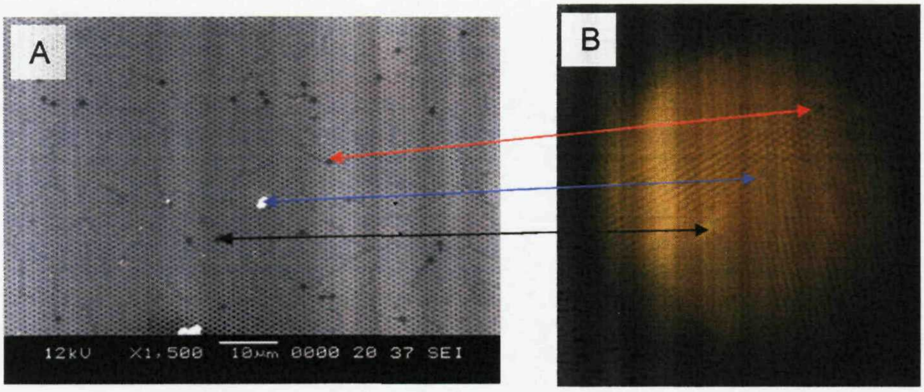

Figure 7 **(A) SEM image and (B) optical image showing correlation between points within the SEM – Structural Chemical Analyser (SEM – SCA).**

2.4.2 Results

Disordered areas of 350 nm and 600 nm void samples were purposely located using the SEM and SER spectra were collected from these areas as well as well ordered areas. The results are shown in Figures 8 and 9 respectively; the blue circle on the

SEM image indicates the region on which the laser was focused for the Raman spectra.

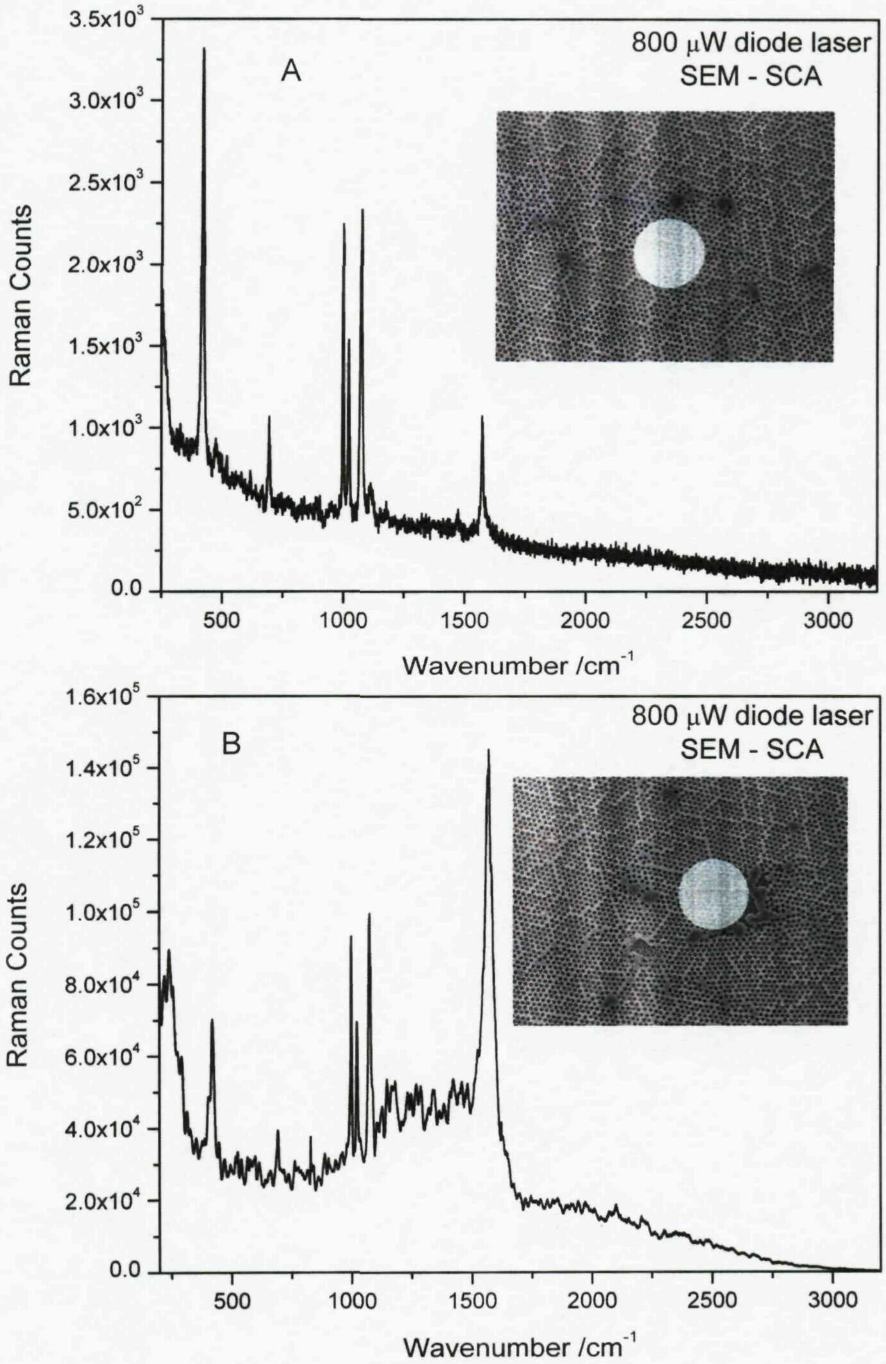

Figure 8 **SEM images and SER spectra obtained from the same points within a 350 nm sample ¾ *d*, for a well ordered region (A) and a poorly ordered area (B). The SEM images were collected using an accelerating voltage of 15 keV, and the magnification is 10,000. The Raman spectra were collected using a 785 nm laser fiber optic probe, with a laser power of < 1mW.**

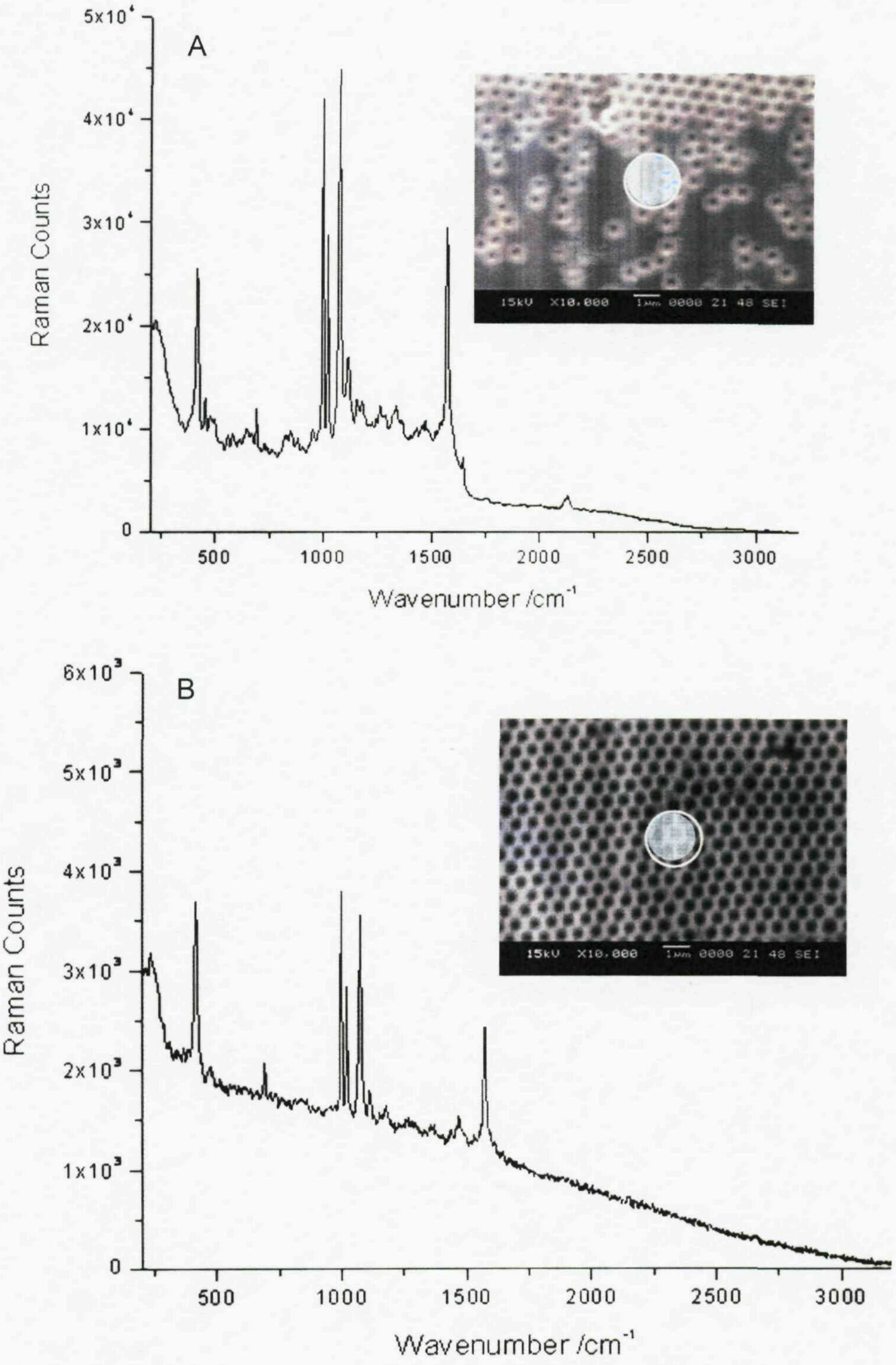

Figure 9 **SEM images and SER spectra obtained from the same points at a 600 nm ¾ *d* sample, for a poorly ordered area (A) and a well ordered region (B). The SEM images were collected using an accelerating voltage of 15 keV, and the magnification is 10,000. The Raman spectra were collected using a 785 nm laser fiber optic probe, with a laser power of < 1mW.**

The key things to notice from Figures 8 and 9 is that when the substrate is well ordered and closely packed the SER spectrum is on a smooth background. However, whenever there is any irregularity in the structure (Fig 8B) or the region illuminated is not characteristic of the ordered structure (Isolated or few voids) (Fig 9B), the spectra have a different shaped background.

When the substrate is well packed, the metal is very smooth and it is simply the plasmon modes contributing to the SER signal. If the laser spot hits a disordered region, as shown in Figures 8 and 9, the signal increases due to the additional roughened surface, the molecules on the surface are also ordered in a more random fashion and so the peaks become broader, however, this needs further investigation to understand why there is such a large increase in signal.

When a region that was not templated was located in the SEM-SCA the spectra obtained was of much lower intensity than when there was a combination of voids and disordered region, Figure 10.

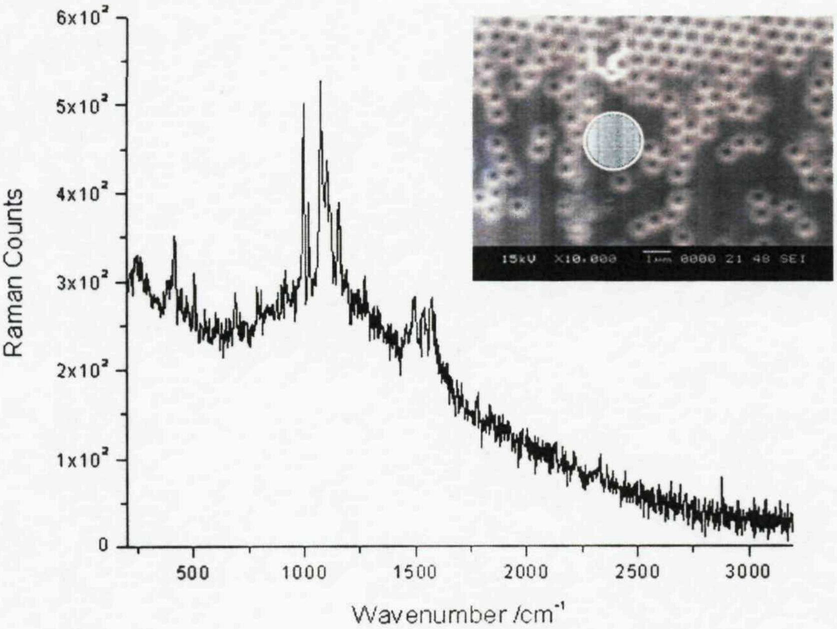

Figure 10 **SEM image and SER spectrum obtained from the same points om a 600 nm ¾ *d* sample, from an area without the template. The SEM images were collected using an accelerating voltage of 15 keV, and the magnification is 10,000. The Raman spectra were collected using a 785 nm laser fiber optic probe, with a laser power of <1mW.**

The background seen in the spectrum in Figure 10 is the same shape as that in Figure 9 B; however the intensity is 2 orders of magnitude lower. This, firstly, shows that the laser must be hitting the voids to create an enhancement in Raman signal, and secondly, the unusual shaped background arises from the gold surface not being smooth. There may be minor peaks and troughs in the surface, which are similar to the ORC substrate, which are creating additional/weaker plasmon modes. The origins of the background will be discussed further in a subsequent section of this chapter.

The variation in signal depending on whether the laser is focused on irregularities in the structure accounts for the variation in signal obtained from the sculpted substrates.

This chapter has, so far, concentrated on the properties of sculpted SERS substrates; however there is another substrate which is also based upon colloid templates, namely the MFON substrate developed by Van Duyne as introduced in Chapter 1 [11]. This substrate is essentially the inverse structure to our substrate, and can be prepared simply by evaporating metal over the top of the spheres as opposed to the electrodepositing through the template.

3. Silver sculpted SERS substrates.

Silver is the most commonly used metal for the preparation of SERS active substrates. This is due to the fact that it is one of the coinage metals, along with gold and copper, and has it also is highly reflective which yields strong surface plasmons. The MFON made by Van Duyne and colleagues is silver, and tuning the plasmon resonances to generate the greatest SERS signal has been achieved successfully. A similar structure to the MFON can easily be prepared using the polystyrene template prepared to make void surfaces, however rather than electrodepositing metal through the template; silver was evaporated over the top, yielding the desired structure.

3.1 Preparation

The colloidal crystal, or dot structure, was prepared by evaporating a 150 nm layer of silver of the top of a 600 nm polystyrene sphere template. 600 nm was chosen as this is the closest sphere size available to the MFON structures, which contain 562 nm particles [12]. The comparative void, or 'anti-dot', structure was also prepared using a 600 nm polystyrene sphere template, and silver was electrodeposited through the template to a film thickness of 0.75 *d*. This was achieved using the method that was described in Chapter 2. Finally, an electrochemically roughened surface was also prepared using the method described by Tian [13], and described in Chapter 2, for a comparison in enhancement between all three surfaces.

3.2 Roughened, dot and anti-dot surfaces

Scanning Electron Microscope (SEM) images for the surfaces are shown in Figure 11.

Figure 11 **Scanning electron microscope images of an electrochemically roughened surface (A), an anti-dot (600 nm ¾ *d*) (B) and a dot MFON type substrate (C) (prepared using a 600 nm polystyrene sphere template with a 150 nm layer of silver evaporated over the surface.) The images were obtained using a Philips XL30 ESEM, with an accelerating voltage of 30 kV and a magnification of 10,000.**

The image shown in Figure 11A is from an electrochemically roughened surface, with irregular peaks and troughs on the surface. Figure 11B shows a 600 nm void substrate grown to ¾ *d* and Figure 11C shows a regularly ordered hexagonally close packed dot structure, with only minor imperfections. The substrates were submerged in 5 mM BT for 30 minutes and then rinsed in ethanol and left to dry for 15 minutes. The SER spectra from these substrates were collected using a 633 nm excitation on a Renishaw Raman 2000 system. The SER spectra are shown in Figure 12

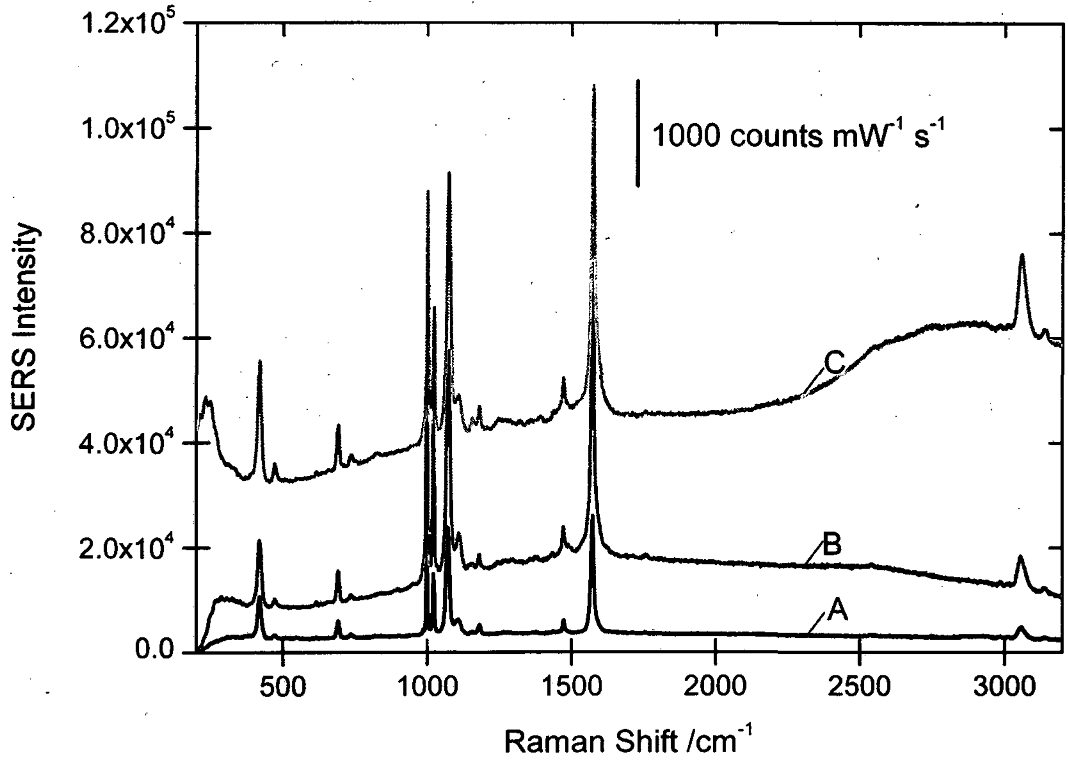

Figure 12 **SER spectra of 5 mM BT adsorbed onto an electrochemically roughened Ag surface (A), an anti-dot Ag 600 nm ¾ *d* substrate (B) and a dot structure consisting of a 600 nm template covered in 150 nm Ag. All spectra were obtained using a Renishaw RM 2000 system with 633 nm excitation, and a single 10 s accumulation.**

The spectra shown in Figure 12 are all plotted on the same scale so they are directly comparable. The SERS from the dot and anti-dot structures are both an order of magnitude more intense than the electrochemically roughened surface, with the dot and anti-dot substrates both having similar intensities.

The plasmon modes that have been described for gold nanovoid structures also occur in Silver structures [14]. However the optical properties of the dot structures are simpler. A normal incidence reflection spectrum from the dot surface is shown in Figure 13.

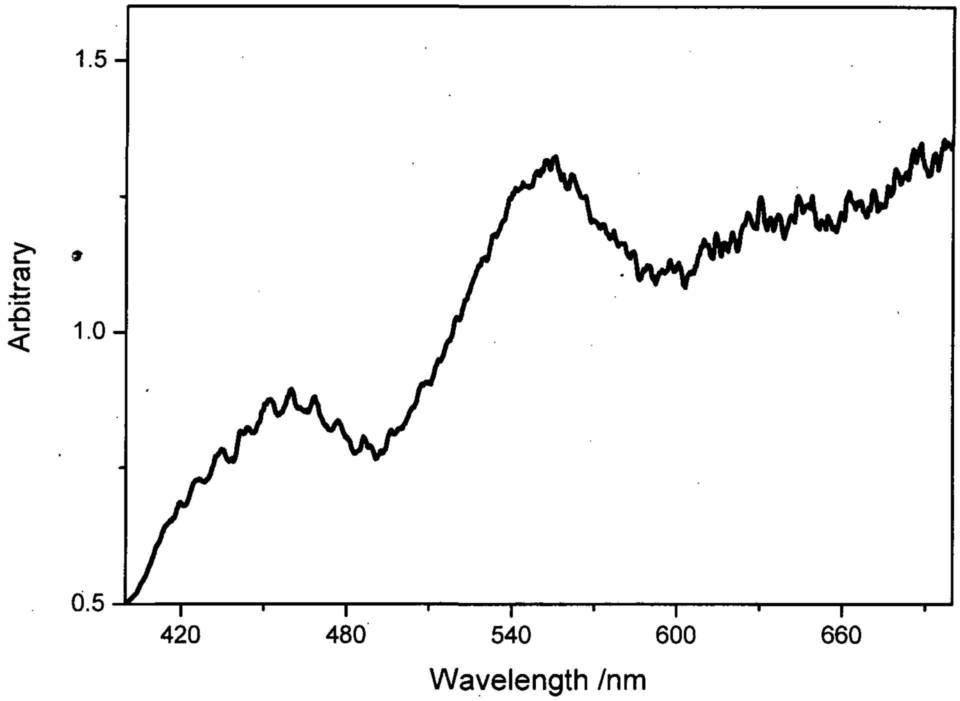

Figure 13 **Normal incidence reflection spectrum from a silver substrate consisting of a 600 nm sphere template covered in 150 nm silver.**

The spectrum shown is one of 10 collected from different spots of the substrate, and is indicative of the response across the entire sample. There is a broad absorption feature which stretches across the visible region of light. This absorption is due to a plasmon mode that is propagating the surface of the sphere, as per the MFON substrate [15], and is why the substrate produces strong SER signals. However, the SER signals obtained from the dot sample is not as reproducible as that previously seen for the well ordered void structures. Five different spectra observed from different points of the substrate are shown in Figure 14.

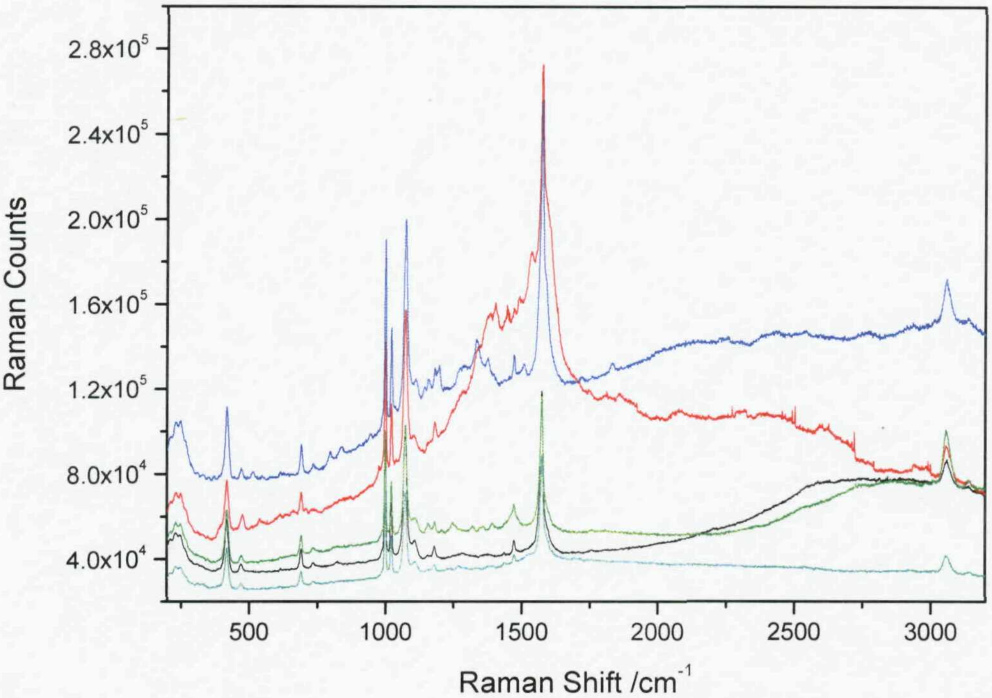

Figure 14 **SER spectra of BT adsorbed onto a substrate comprising a 600 nm polystyrene template covered with 150 nm silver. Each spectrum was acquired with a single 10 s accumulation with a Renishaw Raman 2000 system, using 633 nm excitation.**

The spectra shown in Figure 14 show a variation in terms both peak heights, but also of background seen in the spectra. However, from this comparison between the three substrates it is seen that the dot and anti-dot substrates both show a larger enhancement than the originally used roughened silver substrate [16]. The dot structure shows a larger variation in signal from spot to spot than the antidote (or void) structure.

Silver surfaces oxidize quickly which yields them SERS inactive. The silver metal film over nanosphere type of surface are not as stable as the gold void structures as eventually the nanosphere will degrade yielding the substrate SERS inactive. For these reasons the gold void surface was found to be the most stable surface tested, and will, therefore, be used in future.

4 Spectral Background

As clearly seen in all the SER spectra presented within this thesis, a broad background is present whenever a SERS spectrum for an adsorbate is obtained using our sculpted SERS substrates. The background has been a problem throughout this project. Such backgrounds were also observed for electrochemically roughened gold surfaces, and therefore we do not believe it to be a particular property of the sculpted surfaces. In fact many authors in the past either, only collected SERS spectra over a limited range and therefore did not recognize the contribution to the background, or they removed it from the data by fitting a smooth baseline correction to the data.

Abel and Fischer attributed the background seen from silver colloids as a charge transfer between the Fermi level of the metal and the excited energy levels of the SERS active molecule [17]. However, numerous papers have been published which address the photoluminescence (PL) of metals [18, 19] and it has been found that the PL from metal surfaces contributes to SERS signals [20-22]. This section of the thesis will examine the photoluminescence of gold, and how it relates to the SERS background, observed at different excitation wavelengths, from the sculpted surfaces.

4.1 Photoluminescence.

Photoluminescence is the emission of radiation which is induced by the optical excitation of a sample using an external source of light (usually a laser). The PL of gold, silver and copper was first reported by Mooradian in 1969 [18], and the details of excitation and recombination mechanism were presented. Since this initial paper, theoretical work [23] has shown that that photoluminescence of noble metals can be viewed as an excitation of electrons from occupied *d* bands into states above the Fermi level. At which point there are electron-phonon and hole-phonon scattering processes which lead to energy loss, and finally photoluminescent recombination of the electron into the bulk metal [19]. Shown schematically in Figure 15.

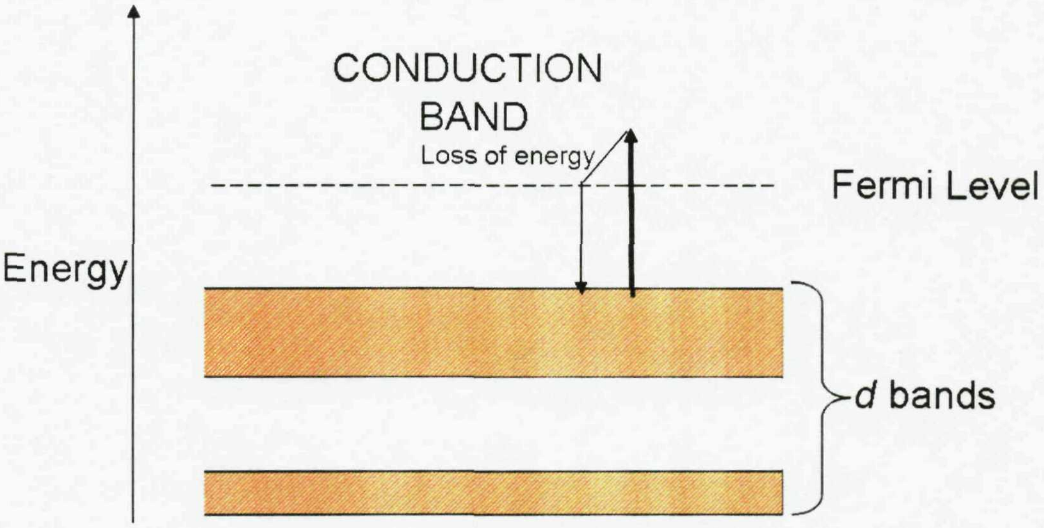

Figure 15 **The excitation of an electron from the *d* band into the conduction band within gold followed by a loss of energy leading to photoluminescent recombination of the electron into the bulk metal.**

There have been thousands of papers published over the last 3 decades which study the PL of various surfaces including roughened [24], gold nanoparticles [19, 25], and other nanostructured surfaces [26, 27] including semi conductors, and it has been found that there is a strong correlation between PL and SERS, as mentioned previously.

4.2 SERS background changes from varying incident laser wavelength.

Early studies from the sculpted SERS substrates showed that a very large background with very little SERS enhancement of BT was observed when 514 nm excitation was utilized in conjunction with the sculpted gold substrates. Therefore only two samples (350 nm and 600 nm) were tested using this excitation. These two samples will be shown in this section showing how the backgrounds change with the 4 different incident laser wavelengths. Due to the varying surface morphologies of each substrate, one film thickness on each substrate was chosen

(¾ *d*) for a comparison between the SERS background observed at different excitation wavelengths. The raw spectrum from each wavelength for the 350 nm sample is shown in Figure 16.

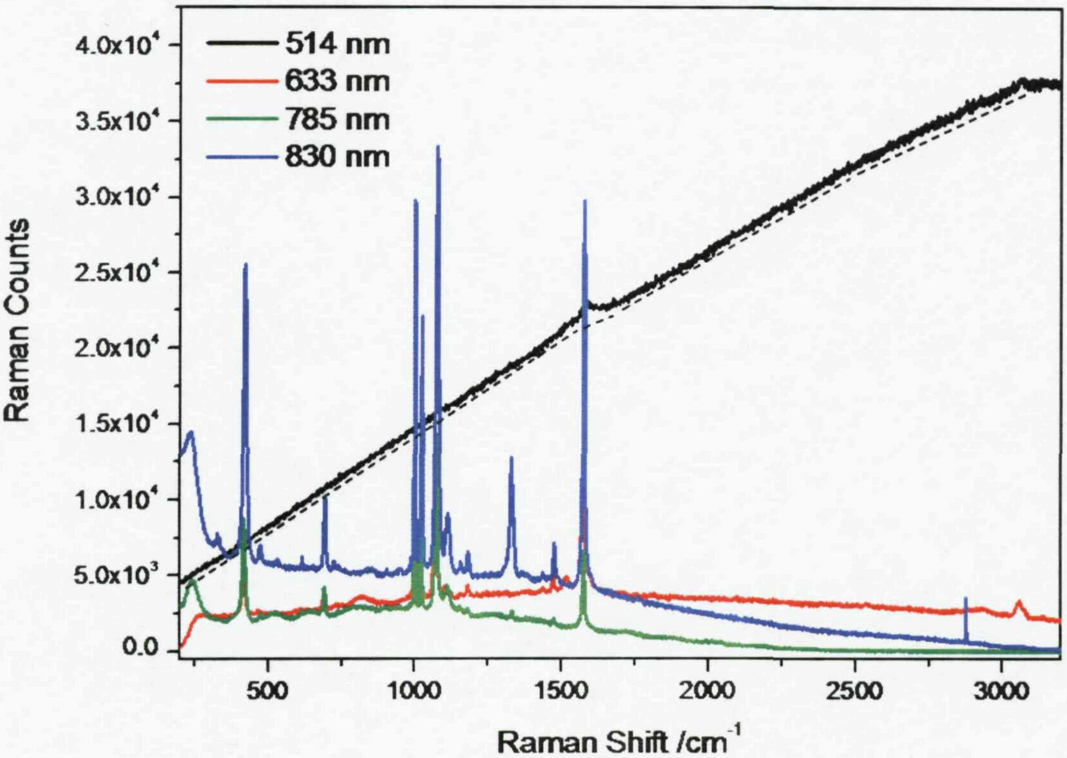

Figure 16 **SER spectra of 10 mM BT adsorbed onto a 350 nm ¾ *d* sculpted void surface. The spectra were acquired using four different excitation wavelengths, each with a single 10 s accumulation using an extended scan. The spectra were acquired using a Renishaw Raman 2000 system for 633 nm excitation, and a Renishaw InVia for the other wavelengths. Each spectrum is uncorrected for laser wavelength at this point. The black dotted line indicates how the backgrounds were plotted.**

From simply observing the raw spectra in Figure 16, it can be seen that the backgrounds change dramatically with laser wavelength. For each spectrum the background was extracted and replotted in 17 as a function of Raman photon energy in eV.

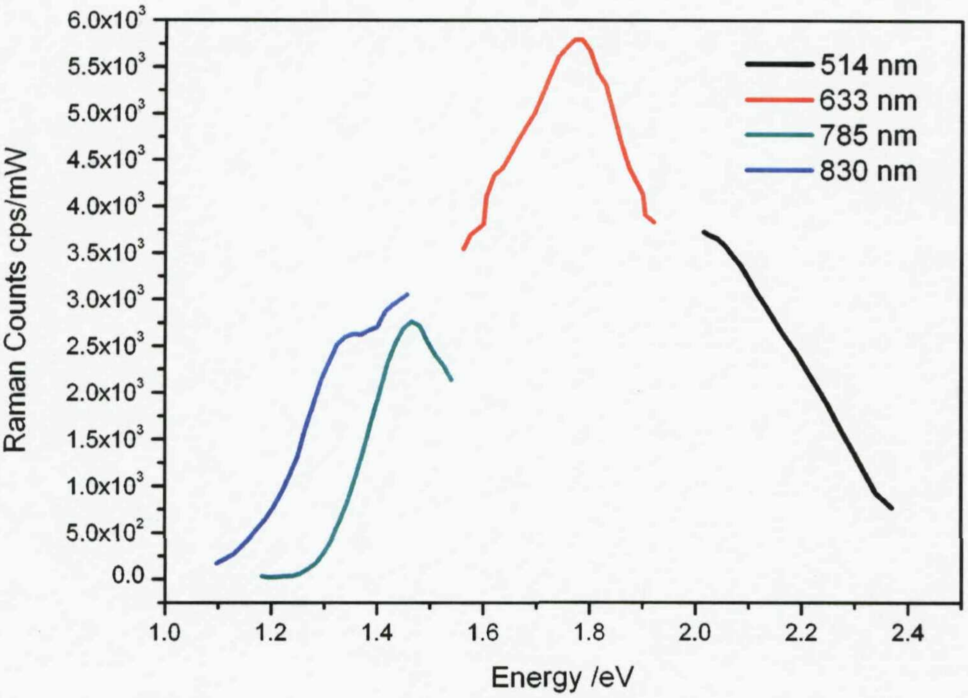

Figure 17 **The background energies from 4 different excitation laser wavelengths (514 nm, 633 nm, 785 nm and 830 nm) upon a 350 nm ¾ *d* sculpted SERS substrate plotted as eV against Raman Counts.**

The plot in Figure 17 shows that there is a broad peak in the background that reaches a maximum at approximately 1.8 eV. There is a slight discrepancy between the overlapping energy at 785 nm and 830 nm. However they are both showing the same trend of decreasing Raman counts with decreasing energy.

The broad peak in the background data can be compared to the plasmon resonance of the sample, shown in Figure 18. The film thickness of interest is marked by a white line. There is a clear correlation between the energy at which the background reaches a maximum as shown in Figure 17 and the energy at which the absorbance of the substrate is greatest.

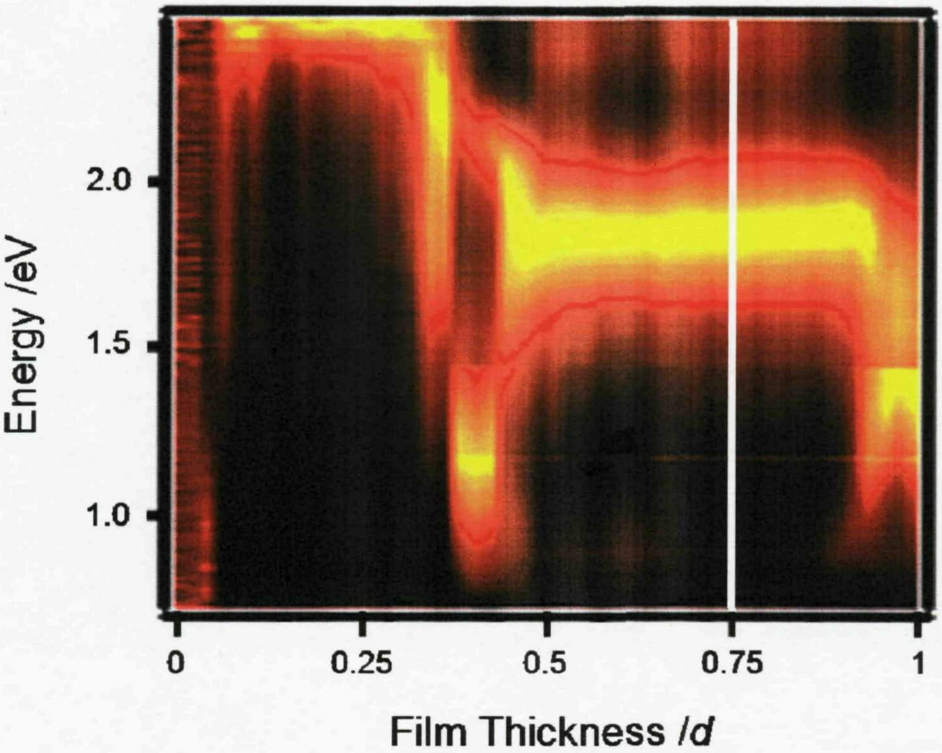

Figure 18 **Angular resolved reflectance spectra as a function of film thickness (*d*) for a 350 nm void sample. The white line across the figure indicates the ¾ *d* thickness used to plot figure 17. Black is the lowest energy and yellow is the highest energy.**

The way that the data from the background has been presented for the 350 nm sculpted surface was repeated for a 600 nm substrate with a film thickness of ~ 0.85 *d*. The background distribution against energy is presented in Figure 19, with the angular resolved reflection spectra, showing the plasmon modes presented in Figure 20.

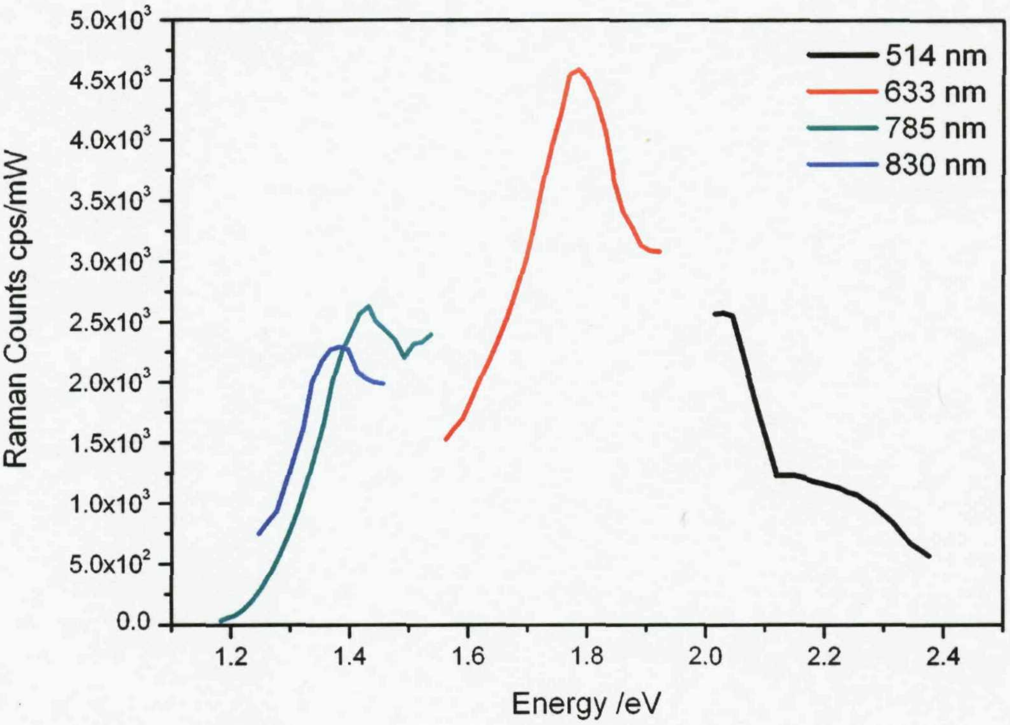

Figure 19 **The background energies from 4 different excitation laser wavelengths (514 nm, 633 nm, 785 nm and 830 nm) upon a 600 nm ¾ *d* sculpted SERS substrate plotted as eV against Raman Counts.**

A broad PL feature with a maximum at approximately 1.8 eV is also observed from the 600 nm 0.85 *d* substrate; however, there is also an extra feature that arises at 1.45 eV which correlates to a plasmon mode seen in Figure 20. The film thickness is marked with a white line.

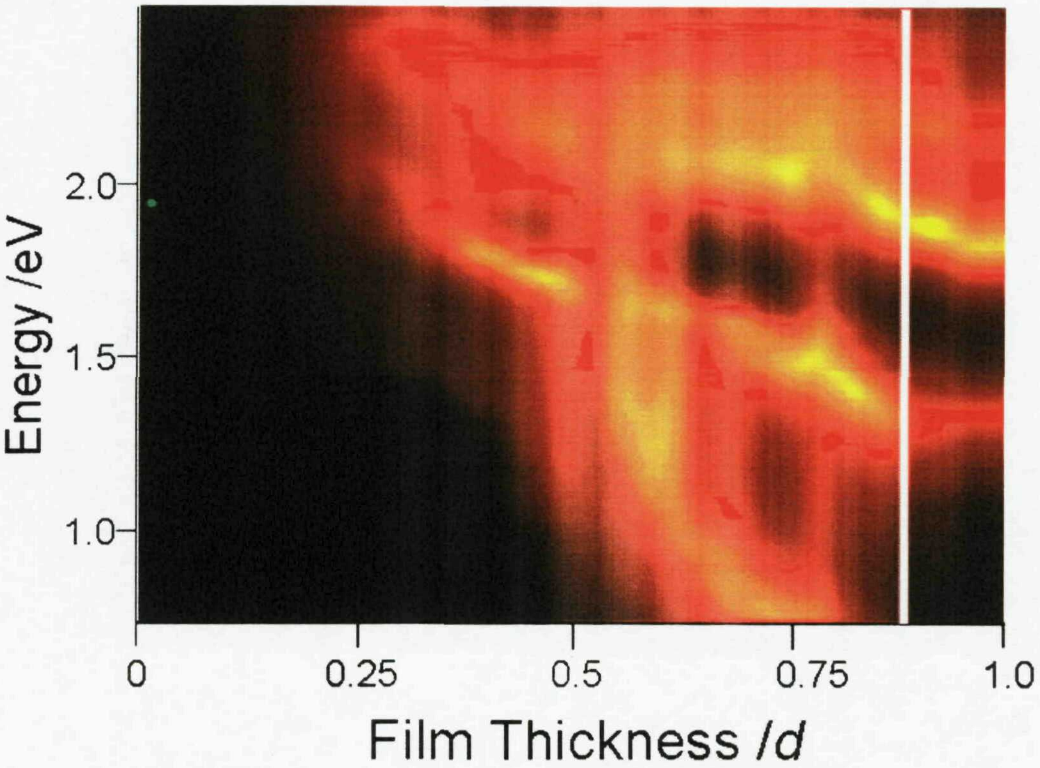

Figure 20 **Angular resolved reflectance spectra as a function of film thickness (*d*) for a 600 nm void sample. The white line across the figure indicates the ¾ *d* thickness used to plot figure 19. Black is the lowest energy and yellow is the highest energy.**

There is a very strong relationship between the plasmon modes and the features within the SERS backgrounds seen from both the 350 nm (Figure 17) 600 nm (Figure 19) substrates, and the shoulder seen in the background at 600 nm correlates to a lower energy, less intense plasmon mode. From these two examples it is clear that the broad continuous background shifts with incident laser excitation and correlates with the plasmon modes, which in turn correlates to the PL. The surface plasmons yield a strong electromagnetic field on the surface, which in turn leads to a higher level of photoluminescence.

Understanding the background of the SERS spectra obtained within this project was not the main objective when analyzing the data. However, from these initial results, it can be seen the sculpted substrates show a background that can be explained in terms of PL. However, further work is required to fully understand the role of the molecule in the emission, and how changing the potential of the surface or the electron 'richness' of the molecule effects the size of the background. At this point in the research the correlation looks promising and could lead to another way of controlling the enhancements obtained from the substrates.

5 Conclusions

The results presented within this chapter have shown the properties of the sculpted substrate developed within this project. If has been shown that the surface morphology is reproducible between void diameters, as are the spectra obtained from them. A standard deviation of 10 % was found when 68 spectra were acquired from 1 sample with the sample film thickness, and a variation of 13% has been found between surfaces [9], and has been attributed to imperfections within the sample. The surfaces can also, unlike most other SERS substrates, be used more than once, simply by electrochemically stripping the molecule from the surface and re-adsorbing another when the surface is clean.

The substrate was also compared to the very well known MFON substrate, via the preparation of an inverse structure, by evaporating silver over the top of the spheres in stead of through them. It was seen that the sculpted dot and anti-dot structures performed well in terms of a higher enhancement than the traditionally roughened surface. However, the shelf life of the Van Duyne MFON structure has been shown to be < 9 months, due to the degradation of the spheres from under the metal. However the sculpted void surface has a shelf life of more than 3 years (in gold), although this will be less for silver due to oxidation at the surface.

The background seen in all SERS measurements was briefly discussed in terms of photoluminescence from the substrate. When there is a plasmon mode on the substrate it is seen that there is an overall increase in the background of the SERS signal, across multiple wavelengths. This corresponds well with the literature on SPP's and PL upon nanostructured surfaces. However, further work is required to fully understand the dependence upon film thickness and any molecular interaction.

6 References

1. Dick, L.A., A.D. McFarland, C.L. Haynes, and R.P. Van Duyne, J. Phys. Chem. B, 2002. **106**: p. 853.
2. Faulds, K., R.E. Littleford, D. Graham, G. Dent, and W.E. Smith, Anal. Chem., 2004. **76**: p. 592.
3. Griffith Freeman, R., K.C. Grabar, K.J. Allison, R.M. Bright, J.A. Davis, A.P. Guthrie, M.B. Hommer, M.J. Jackson, P.C. Smith, D.G. Walter, and M.J. Natan, Science, 1995. **267**(1629).
4. Haes, A.J., C.L. Haynes, A.D. McFarland, G.C. Schatz, R.P. Van Duyne, and S. Zou, MRS Bulletin, 2005. **30**: p. 368.
5. Hulteen, J.C., D.A. Treichel, M.T. Smith, M.L. Duval, T.R. Jenson, and R.P. Van Duyne, *Nanosphere lithography: Size tunable silver nanoparticle and surface cluster arrays.* J. Phys. Chem. B, 1999. **103**: p. 3854.
6. Mulvaney, S.P., L. He, M.J. Natan, and C.D. Keating, J. Raman. Spectrosc., 2003. **34**: p. 163.
7. Tessier, P.M., O.D. Velev, A.T. Kalambur, J.F. Rabolt, A.M. Lenhoff, and E.W. Kaler, J. Am. Chem. Soc., 2000. **122**: p. 9554.
8. Xia, Y., Y. Yin, Y. Lu, and J. Mclellan, Adv. Funct. mater., 2003. **13**(12): p. 907.
9. Cintra, S., M.E. Abdelsalam, P.N. Bartlett, J.J. Baumberg, T.A. Kelf, Y. Sugawara, and A.E. Russell, Faraday Discussions, 2006. **132**: p. 191-199.
10. Zhang, X.Y., J. Zhao, A.V. Whitney, J.W. Elam, and R.P. Van Duyne, Journal of the American Chemical Society, 2006. **128**(31): p. 10304-10309.
11. Hulteen, J.C., D.A. Treichel, M.T. Smith, M.L. Duval, T.R. Jenson, and R.P. Van Duyne, J. Phys. Chem. B, 1999. **103**: p. 3854.
12. Dick, L.A., A.D. McFarland, C.L. Haynes, and R.P. Van Duyne, *Metal Film over Nanosphere (MFON) Electrodes for Surface Enhanced Raman Spectroscopy (SERS): Improvements in Surface Nanostructure Stability and Suppression of Irreversible Loss.* J. Phys. Chem. B, 2002. **106**: p. 853.
13. Tian, Z., B. Ren, and D. Wu, J. Phys. Chem. B, 2002. **106**(37): p. 9463.

14. Bartlett, P.N., J.J. Baumberg, S. Coyle, and M.E. Abdelsalam, Faraday Discuss., 2004. **125**: p. 117.
15. Van Duyne, R.P., Faraday Discuss., 2005. **132**: p. 1.
16. Fleischmann, M., P.J. Hendra, and A.J. McQuillan, Chem. Phys. Lett., 1974. **26**(2): p. 163-166.
17. Abel, H.B. and F. Fischer, Physica Status Solidi B-Basic Research, 1991. **167**(2): p. 741-751.
18. Mooradian, A., Phys. Rev. Lett., 1969. **22**: p. 185.
19. Wilcoxon, J.P., J.E. Martin, F. Pasapour, B. Wiedenman, and D.F. Kelley, J Chem. Phys., 1998. **108**(21): p. 9137.
20. Chen, C.K., A.R.B. de Castro, and Y.R. Shen, Phys. Rev. Lett., 1981. **46**(2): p. 145.
21. Chen, C.K., T.F. Heinz, D. Ricard, and Y.R. Shen, Phys. Rev. B., 1983. **27**(4): p. 1965.
22. Itoh, T., V. Biju, M. Ishikawa, Y. Kikkawa, K. Hashimoto, A. Ikehata, and Y. Ozaki, Journal of Chemical Physics, 2006. **124**.
23. Apell, P., R. Monreal, and S. Lundqvist, Phys. Scr., 1988. **38**: p. 174.
24. Boyd, G.T., Z.H. Yu, and Y.R. Shen, Physical Review B, 1986. **33**(12): p. 7923-7936.
25. Nappa, J., G. Revillod, J.P. Abid, I. Russier-Antoine, C. Jonin, E. Benichou, H.H. Girault, and P.F. Brevet, Faraday Discuss., 2004. **125**: p. 145.
26. Girlando, A., W. Knoll, and M.R. Philpott, Solid State Communications, 1981. **38**(10): p. 895-898.
27. Bouhelier, A., M.R. Beversluis, and L. Novotny, Appl. Phys. Lett., 2003. **83**(24): p. 5041.

Chapter Six: Applications of sculpted SERS substrates.

Throughout this thesis theory has been applied to predict the performance of the sculpted SERS substrates, however, little work has been presented which shows the potential of these substrates in applications such as chemical sensors. In the last 10 years SERS has seen a growth in research and work carried out by Kneipp and Kneipp has shown that the sensitivity of SERS can be improved to the point that single molecules can easily be detected [1, 2]. Van Duyne has reported the detection of sucrose *in situ* in a rat [3], and SERS is being used for drug detection and DNA detection purposes at the University of Strathclyde [4-7].

From the results presented in Chapters 4 & 5, it is clear that it is possible that the sculpted substrate developed in this thesis may provide a means of overcoming the limitations of SERS and may enable extension to a wider range of applications, with *in situ* electrochemical experiments being the initial target for application driven research. Work will be presented in this Chapter showing how the sculpted substrates can be used as electrodes for *in situ* electrochemical experiments, and the advantages over other electrochemical SERS substrates available.

1 In Situ SERS substrates

SERS is a technique that is ideally suited to *in situ* studies of electrode reactions and the electrode/electrolyte interface, and was initially discovered in such a way [8] . There are several reasons for this. The technique is highly surface selective – only molecules close to the metal surface, within ~ 20 nm [9, 10], experience the surface enhancement. Most electrolyte solutions do not interfere with the Raman spectra obtained from the visible region of the spectrum used to make the measurement. The technique allows molecular characterisation of the species or intermediates at the electrode surface through the assignment of their unique Raman spectra, with the ability to assign bands below 100 cm^{-1}. Also, because of the low Raman cross-section of water the technique is ideally suited to measurements of electrodes in aqueous solutions without significant interference from the bulk solvent.

However, electrochemical SERS has suffered the same drawback that has hampered the development of this technique, irreproducible substrates. Thus considerable effort has been put into the optimisation of the roughening procedure for ORC electrodes by various groups, the magnitudes of the enhancement varies significantly (by a factor of 10 or more) from place to place across the surface, the magnitude of the enhancement is not stable (it can change with time and can be destroyed at some potentials) [11]. The roughened surfaces also make quantitative studies very difficult. Reproducibility from electrode to electrode or even at different points on the same electrode is poor, there is a large uncertainty about the precise surface area of the electrode, and the location of the molecules that give rise to the SERS signal is uncertain .

There has been a lot of research into developinga SERS substrate that can be used as an *in situ* electrode, as introduced in Chapter . Tian *et al.* have optimised electrochemical roughening techniques and combined these with the improvements in Raman instrumentation (the use of a confocal microprobe geometry, holographic notch filters and a CCD detector) to obtain SERS from catalytically and electrochemically relevant metals such as Ni, Pt and Rh [12-14] or used templated arrays of metal nano-wires [12, 15]. However, the roughening approach yields irreproducible substrates, and spectra.

Weaver *et al.* [16] developed the technique of coating SERS active gold surfaces, prepared by electrochemical roughening, with thin (2 to 5 monolayers thick) continuous layer of Pt or other metals of interest. In this “borrowed SERS” approach the signal for the overlying metal borrows the SERS enhancement from the substrate; a procedure that works provided the metal overlayer is kept very thin (2 to 5 monolayers thick). This approach can be used to obtain SERS for molecules at Pt, Pd and Rh electrodes, however, there is come controversy about whether there are pinholes in the overlayer which give rise to the enhancement.

Nanostructured SERS substrates (introduced in Chapter 1) have been used in recent years to try and overcome the problems seen with electrochemically roughened electrodes. However, colloids are unsuitable for electrochemical applications because they do not provide a continuous electrode surface, whereas, photonic crystals have proven difficult or costly to fabricate. One nanostructured substrate which has improved electrochemical SERS, is the use of the MFON structures described by Van Duyne [11] and introduced in Chapter 1. Van Duyne and colleagues have shown that these silver surfaces give a significant *in situ* surface enhancement, and show good stability [11], whilst improving the potential window for electrochemical SERS experiments. Clearly there is scope for improved electrochemical SERS substrates that can be used to study electrode reactions a variety of different metal surfaces.

The results in previous chapters from the sculpted substrate introduced in this thesis have shown that there is control over the enhancement obtained from the surface, by monitoring the plasmon modes, and that the enhancement can be tuned to a specific wavelength or molecule. Also, that the reproducibility and stability of the surface is second to none. Therefore, two initial experiments were performed to show their potential as electrochemical SERS substrates. The detection of pyridine and carbon monoxide will be presented in the following sections of this chapter.

2 Detection of Pyridine in Solution.

In the first example pyridine will be used as a probe molecule. Pyridine has a similar structure to benzene, however one carbon is replaced by nitrogen, which can bond to a metal, gold in this case, surface through the lone pair. The spectrum of neat pyridine is presented in Figure 1, with the assignment of peaks in Table 1.

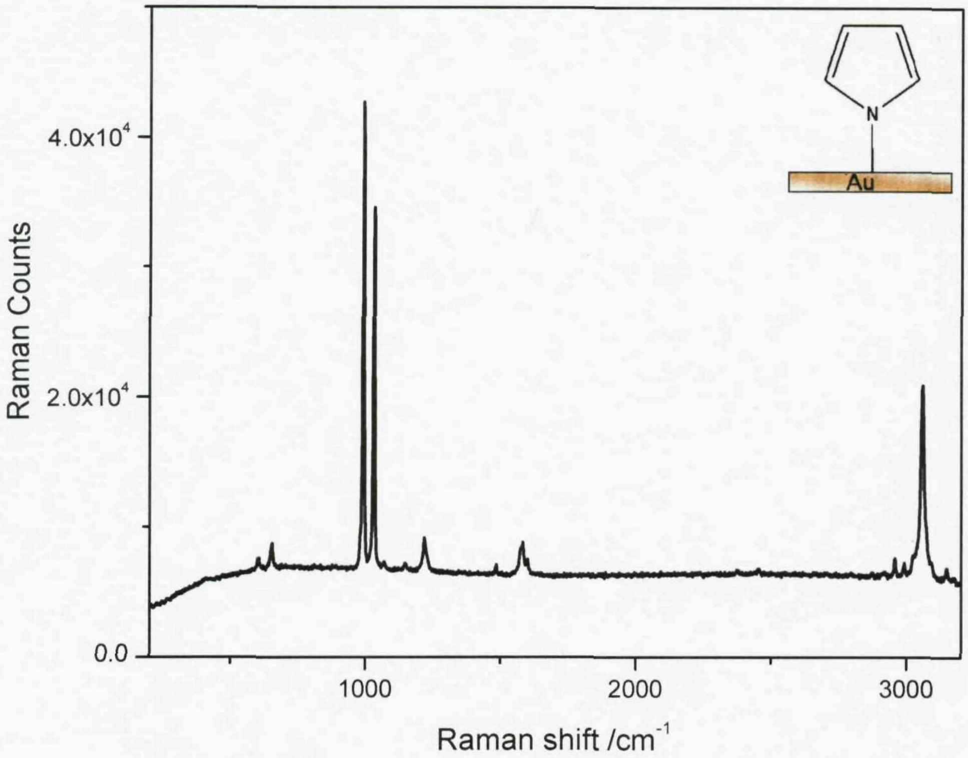

Figure 1 **Raman spectrum of neat pyridine, obtained using a 633 nm excitation wavelength, with a Renishaw Raman 2000 system. The spectrum was acquired with a single 10 s extended scan, using ~2 mW power in non-confocal mode.**

Table 1 **Peak assignments for the Raman spectrum of pyridine.**

Wavenumber /cm^{-1}	Assignment
652.5	ν(C – N)
990.9	a_1, ν(C – H)
1030.2	a_1, ν(C – C – C)
1217	a_1, ν(C – H)
1581	a_1, ν(C – C – C)
3058.6	a_1, ν(C – H)

A solution of 0.05 M pyridine in 0.1 M KCl was prepared as an electrolyte, and spectra were collected using a Renishaw Raman 2000 system, in an *in situ* electrochemical cell, as described in Chapter 2. All spectra were collected with an integration time of 60 s for 3 accumulations. The electrochemical SER spectra of pyridine at potentials 0.2 to -1.6 V vs. MMSE are presented in Figure 2.

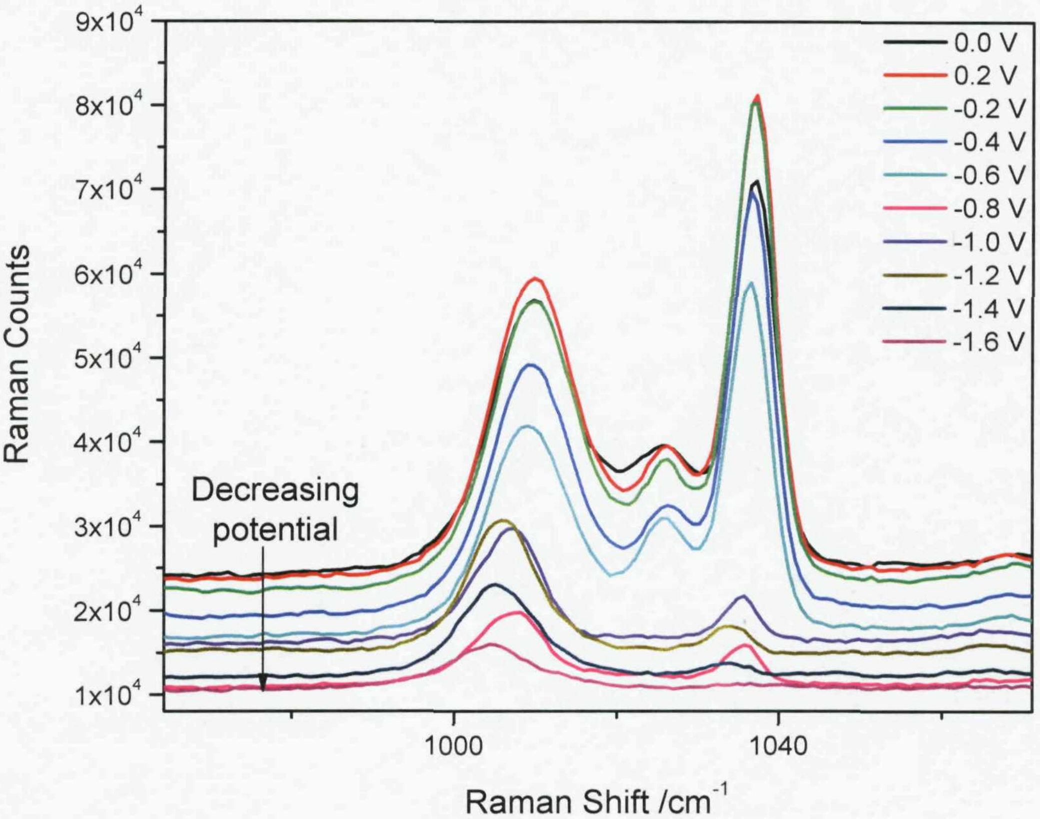

Figure 2 **Electrochemical SER spectra of pyridine recorded as a function of potential. Each spectrum was collected using an extended scan with 3 x 60 s accumulations. All potentials are shown vs. MMSE. The substrate was a 600 nm ¾ *d* gold surface.**

The gold surface was stable under these electrochemical conditions and the SER spectra are consistent with the published spectra for pyridine at silver [8, 17, 18] and gold [19, 20] electrode surfaces. There is a shift in the peaks in relation to the spectrum of neat pyridine. The two bands at 1012 and 1030 cm^{-1} have been assigned to symmetric ring breathing modes and occur at frequencies close to those for pyridine in aqueous solution. The band at 1026 cm^{-1} has been assigned to pyridine chemisorbed at the metal surface through the nitrogen lone pair. Between 0.2 and -0.6 V, as the potential is taken more negative the overall intensity of the band at 1010 cm^{-1} decreases whilst that at 1037 cm^{-1} remains approximately constant, neither band shifts significantly in position. However, between -0.6 and -0.8 V there is a significant change in the appearance of the spectra, the bands at 1010 and 1037 cm^{-1} shift to lower wavenumber and decrease in intensity while the band at 1026 cm^{-1}, attributed to chemisorbtion of the pyridine at the gold surface, disappears. These changes are consistent with a change in the bonding of the pyridine to the gold surface, as shown in Figure 3, in agreement with that reported for pyridine on silver [8, 17], although for the gold surface this occurs at a potential about 0.6 V negative of that on silver. The signal from the pyridine molecule is lost when the potential was reduced to -1.6 V, which is attributed to the desorption of the pyridine.

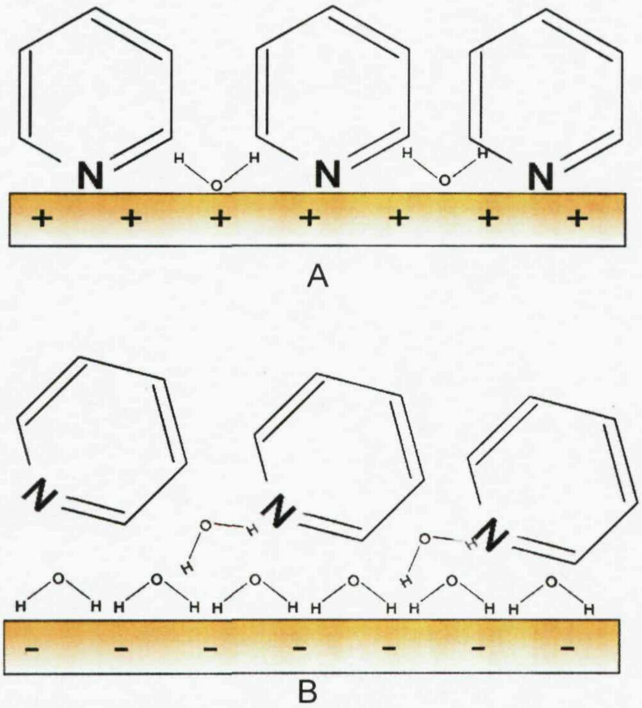

Figure 3 **Diagram showing how pyridine changes it's reorientation at the surface of the gold electrode when the potential changes from +0.2 V vs. MMSE (A) to -0.6 V vs MMSE (B).**

2.1 Irreversible loss of signal.

A recurrent problem which has hampered the application of SERS to electrochemistry over the last 30 years has been the irreversible loss in enhancement on cycling to extreme potentials. Although there have been some recent improvements in the stability of substrates [11] the situation is still far from ideal.

From Figure 2, it can be seen that when the potential reaches -1.6 V vs. MMSE the SER signal from pyridine has significantly reduced. Figure 4 shows the spectra obtained at 0 V at the start of the experiment, and the equivalent spectrum when the potential is returned to 0 after being cycled to an extreme cathodic current. Clearly the substrate suffered from a loss of signal, similar to that which hampers the success of other SERS substrates. However, upon inspection with the optical microscope we found that there were bubbles trapped on the electrode surface. When the electrode was tapped to shake off the bubbles and the surface was rewet the original spectrum, of adsorbed pyridine was recovered, as shown in Figure 5. The difference between these two spectra is most likely to be a slight change in the position on the sample or focussing after tapping the electrode.

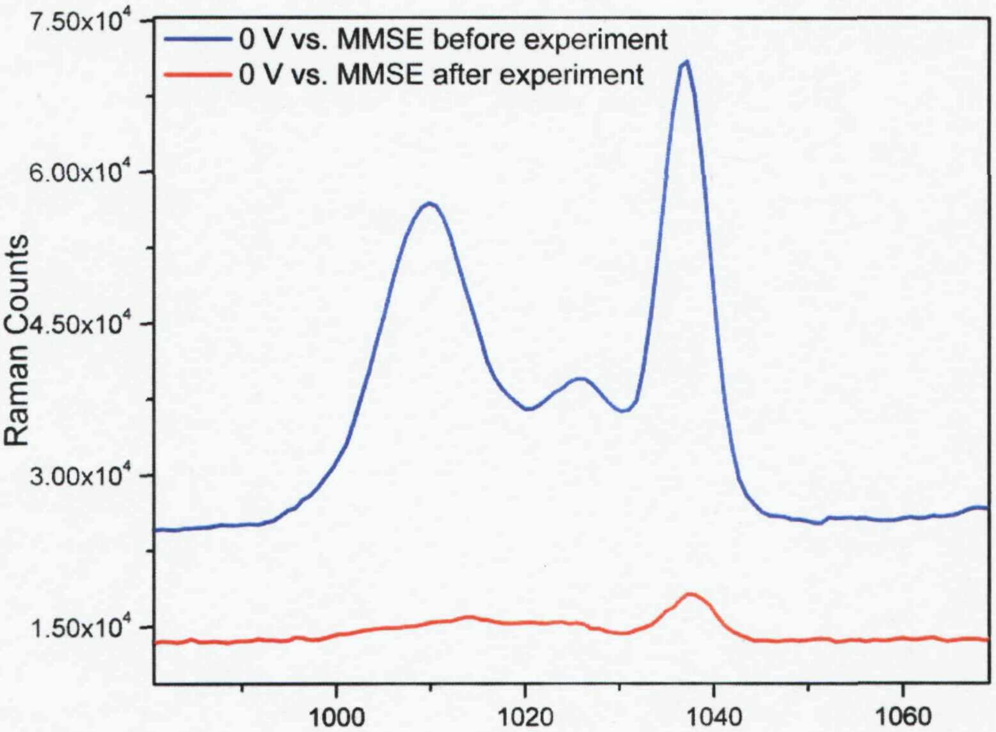

Figure 4 **Comparison between the SER spectra of pyridine obtained at 0 V at the start of the experiment (blue) and after cycling the electrode to -1.6 V (red). Both spectra were obtained from the same point on the electrode with 3 x 60 s extended scans.**

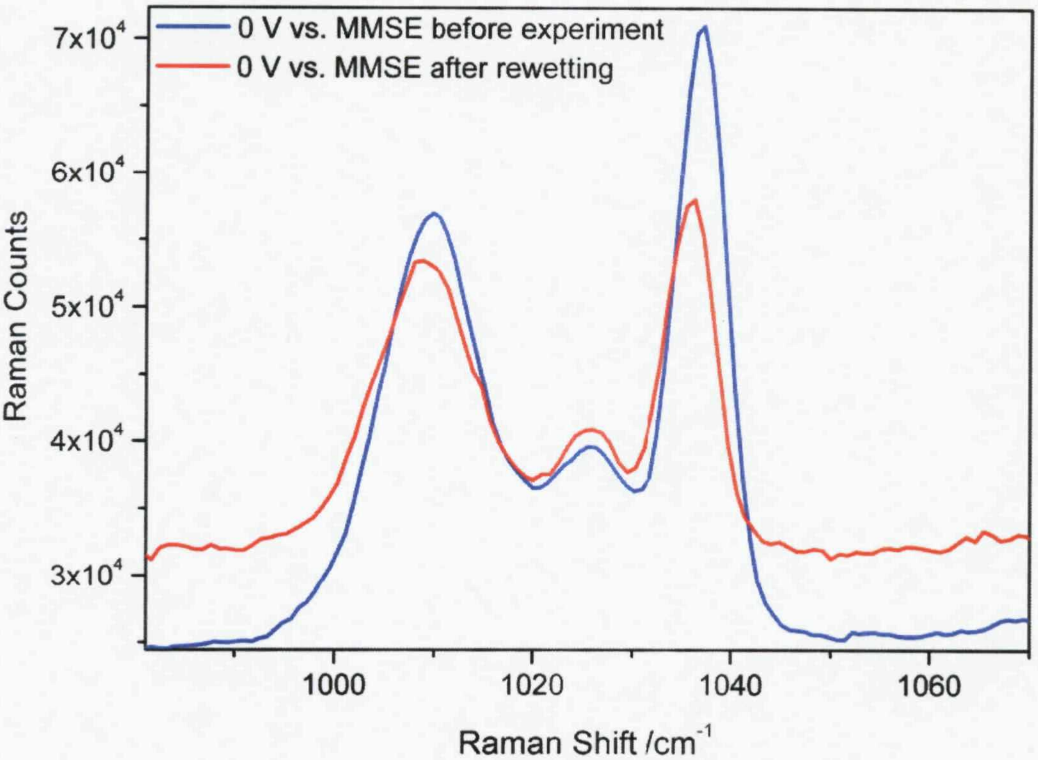

Figure 5 **SER Spectra of pyridine at 0 V in the original experiment and after the substrate had been rewet with electrolyte. Each spectrum was obtained with 3 x 60 s extended scans.**

The fact that the signal at the sculpted substrate is nearly recoverable without the need to clean or re-prepare the surface is attributable to the mechanism of enhancement. In the case of the sculpted substrate the enhancement comes from the bulk of the structure as explained in Chapters 3 & 4, rather than from the presence of special surface features. SERS substrates prepared by ORC roughening rely on such special surface features, which are easily destroyed at extreme potentials and do not re-form when the potential returns to a more reasonable value.

The widened electrochemical window that the sculpted SERS substrate can reach allows more extreme potential dependence to be carried out using SERS in the future. The next example of how the sculpted SERS substrate can be used as *in situ* electrodes is the detection of carbon monoxide.

3 Detection of Carbon Monoxide using Platinum nanostructures.

Palladium and platinum are important catalytic metals, and it would be highly advantageous to be able to use surface enhanced Raman spectroscopy (SERS) to study reactive species and intermediates on their surfaces. Up to this point in the thesis only the coinage metals have been deposited through or over the polystyrene templates, however it is also possible to deposit other metals such as Pt, Pd, Co and Ni [21-24] and it has been reported that SERS can be obtained using sculpted Pt and Pd surfaces, with typical enhancements of 1800 and 500, respectively [25]. SERS of carbon monoxide, an important poison of catalyst surfaces, is investigated and the potential dependence of the spectra reported.

3.1 CO absorption on Platinum.

Carbon monoxide is a known poison for fuel cell catalysts as it adsorbs to the metal in an irreversible manner, blocking binding sites important in the electrocatalytic reactions. The adsorption and stripping of carbon monoxide is easily monitored using Cyclic Voltammetry (CV). Figure 6 shows the standard CV of a rough polycrystalline Platinum surface, obtained in an electrolyte solution of 1 M H_2SO_4. A standard three electrode cell was used with Pt wire as the counter electrode and a mercurous sulphate reference electrode.

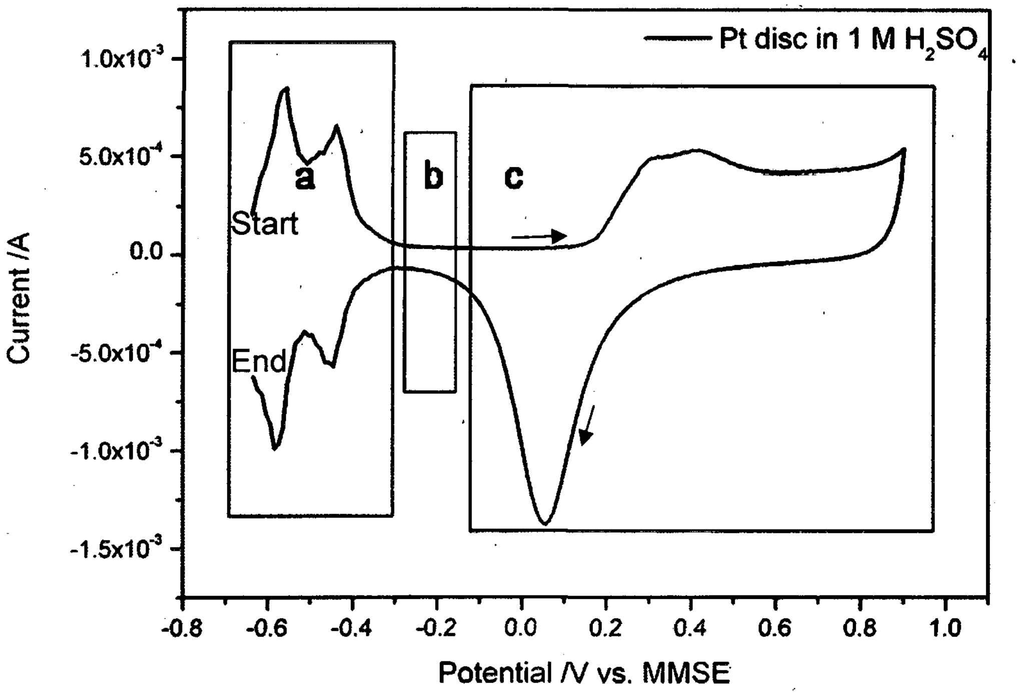

Figure 6 **Cyclic Voltammogram of 1 cm^2 Pt disc electrode in deaerated 1 M H_2SO_4. The sweep rate was 100 mVs^{-1}.**

The features of the CV can be split into three distinct regions: The hydrogen region (a), where desorption of hydrogen occurs in the forward scan, and adsorption occurs in the backward scan. The double layer region (b) arises due to the segregation of charge which occurs at the interface between the working electrode and the electrolyte. Region c is the oxide region, in the forward scan oxide layers form on the platinum surface which are then stripped on the backward scan.

When a monolayer of CO is adsorbed onto a Pt surface there is a very noticeable change in the CV. The CV shown in Figure 7 shows the result after a 1cm^2 diameter Pt disc electrode, held at -0.5 V vs. MMSE was submerged in a 1 M H_2SO_4 solution which was purged in CO for 45 minutes, and then with N_2 for 45 minutes so that a monolayer of CO was left on the surface. The CV in Figure 7 shows the CO that was adsorbed to the surface being irreversible stripped.

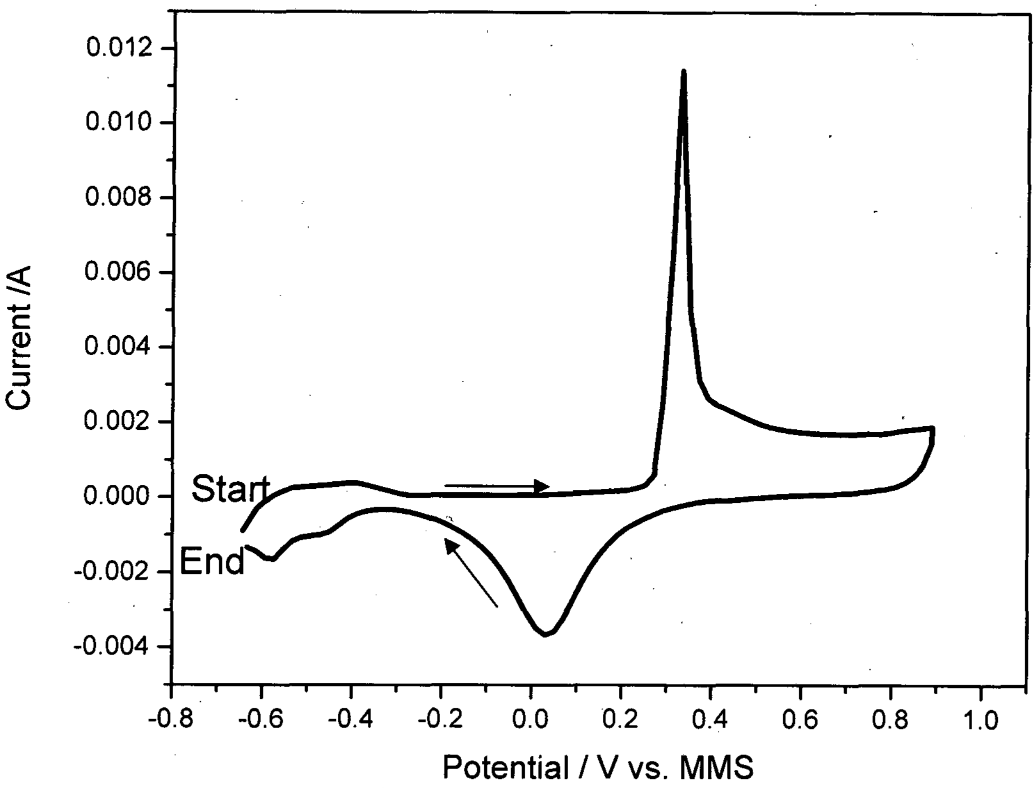

Figure 7 **Cyclic Voltammograms of a 1 cm^2 Pt disk electrode in 1 M H_2SO_4 before and after CO adsorption. The electrode was held at -0.5 V vs. MMS for 45 minutes prior to the CV being acquired at 100 mVs^{-1}**

The monolayer of adsorbed CO blocks the surface for any other electrochemical reactions as evidenced by the suppression of the hydrogen features in the forward scan of the CO covered electrode.

3.2 CO on Pt detection using vibrational spectroscopy

Carbon monoxide adsorbed on metal surfaces was detected using infrared spectroscopy in the late 1950s by Eischens *et al* [26, 27], publications followed looking at how the peak intensity and positions shift to higher wavenumbers with increasing surface coverage [28, 29]. There were also observations of the CO stretch shifting, by ~30 cm^{-1} to higher wavenumber with changing potential, by Bewick [30, 31], Kumimatsu [32-34], Pons [35] and Weaver [36]. The shift in wavenumber has been accredited to two things [37]: The change in bond strength with electrode potential, and the effect of the electric field on the double layer region on the molecule, which has been termed the electrochemical Stark effect.

The detection of the C≡O bond and the shift of band positions with changing potential have commonly been reported in the infrared. However, monitoring the adsorption of CO with SERS has the advantage that the Pt – C bond can be monitored as well as the C≡O bond, which is the more bond important in terms of catalyst performance. However, it is only in relatively recent times that any Pt SERS substrates have been prepared, in order to utilise SERS to monitor this interaction.

3.2.1 Detection of CO on Pt using SERS

Weaver and co-workers developed a Pt SERS surface by using a deposition method to prepare a platinum-coated gold electrode [38], which exhibited well-resolved SERS spectra of adsorbed carbon monoxide via the electromagnetic long-range effect of the SERS-active substrate gold. This deposition procedure was further developed, and they claimed a pinhole-free ultrathin film of platinum coated onto gold, yielding optimal SERS properties with little or no chemical/spectral interferences from the underlying gold substrate [39].

Recent studies by Tian and co-workers have found that the enhancement factors of Raman scattering for other transition metals (Pt, Ru, Rh, Pd, Fe, Co, Ni, and their alloys), varies from 10-fold to 103-fold depending on the nature of the metal and the surface roughening procedures [15, 40, 41]. Several typical organic or inorganic adsorbates, including CO, adsorbed onto the highly roughened platinum electrodes from aqueous solutions have been examined, and particularly useful information reflecting the metal-adsorbate interaction can be well resolved, enabling further probing of the nature of the molecule-platinum surface interaction occurring in the electrochemical system. Further work from Tian's group has seen the development of nanostructured Pt and Pd electrodes [42-46], where nanocubes and other nanoparticles have been produced, giving rise to more reproducible enhancements.

Our group has shown that sculpted Pt and Pd SERS substrates can be developed, using the same technique that is employed for gold. Typical enhancement factors of 1800 and 500, respectively, have been obtained from BT on each surface [25], and a Pt surface will now be presented for the detection of CO *in situ.*

3.2.2 Detection of CO on a sculpted SERS substrate

A monolayer of CO was adsorbed onto a 600 nm ¾ *d* Pt sculpted SERS substrate by bubbling CO through an electrochemical cell containing 1 M H2SO4, where the working electrode (the SERS substrate) was held at a potential of -0.15 V vs. SCE for 45 minutes. The counter electrode was Pt gauze and the reference electrode was SCE. The CO was initially stripped from the surface to confirm that the CO was adsorbed using this procedure. A CO stripping peak similar to that seen in Figure 7 was observed, thereafter CO was readsorbed by bubbling CO through the solution for an additional 45 minutes whilst holding the potential at -0.15 V vs. SCE, and SER spectra were acquired at varying potentials in the saturated solution.

Spectra were collected using a cell similar to that described in Chapter 2, with the slight modification that a Teflon rod was attached to the SERS electrode and screwed into the base of the cell. This allowed full control over the distance between the quartz cover slip and the electrode. Work by Ren *et al* has shown that the SERS signal drops exponentially with solution thickness [47] and they found that the optimal distance between the electrode and the window was 200 μm. The electrode was moved to the correct distance using the focus control of the microscope to measure the distance between the quartz window and the surface of the electrode. The potential was controlled using a μAutolab III potentiostat.

The spectra obtained from varying potentials for the Pt – C region are shown in Figure 8, and the corresponding spectra from the C≡O region are shown in Figure 9.

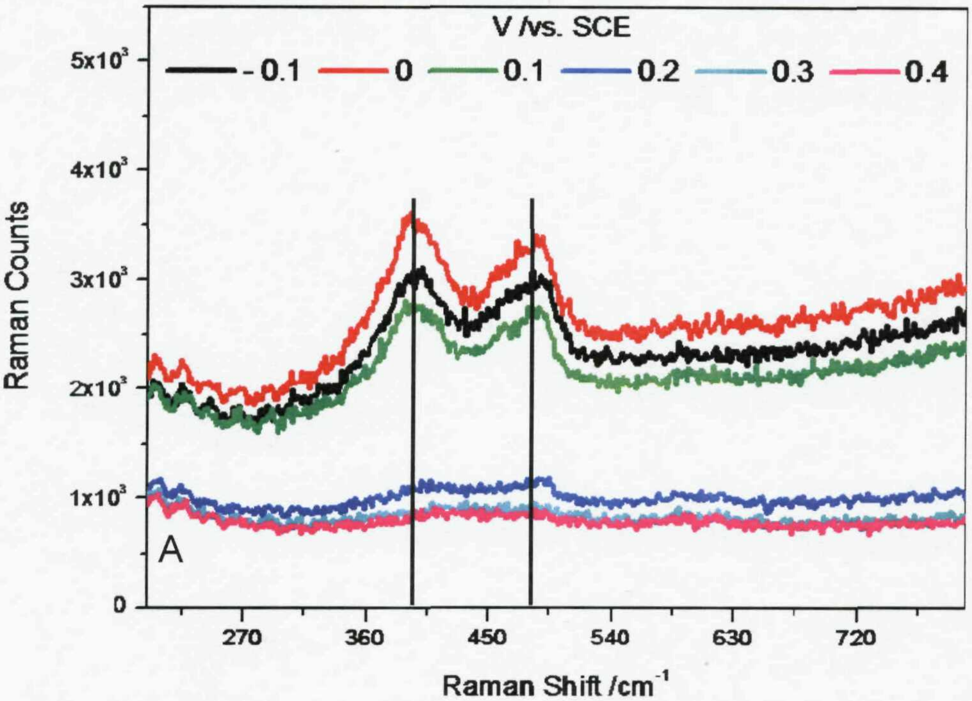

Figure 8 **Potential dependent SER spectra of the Pt – C bond, in the Carbon Monoxide spectrum, adsorbed onto a nanostructured Pt 600 nm ¾ *d* electrode in 1 M H_2SO_4 that was saturated with CO. The spectra were acquired using a long working distance x50 objective on a Renishaw Raman 2000 system with 633 nm excitation. Each spectrum was acquired using a single 60 s extended scan.**

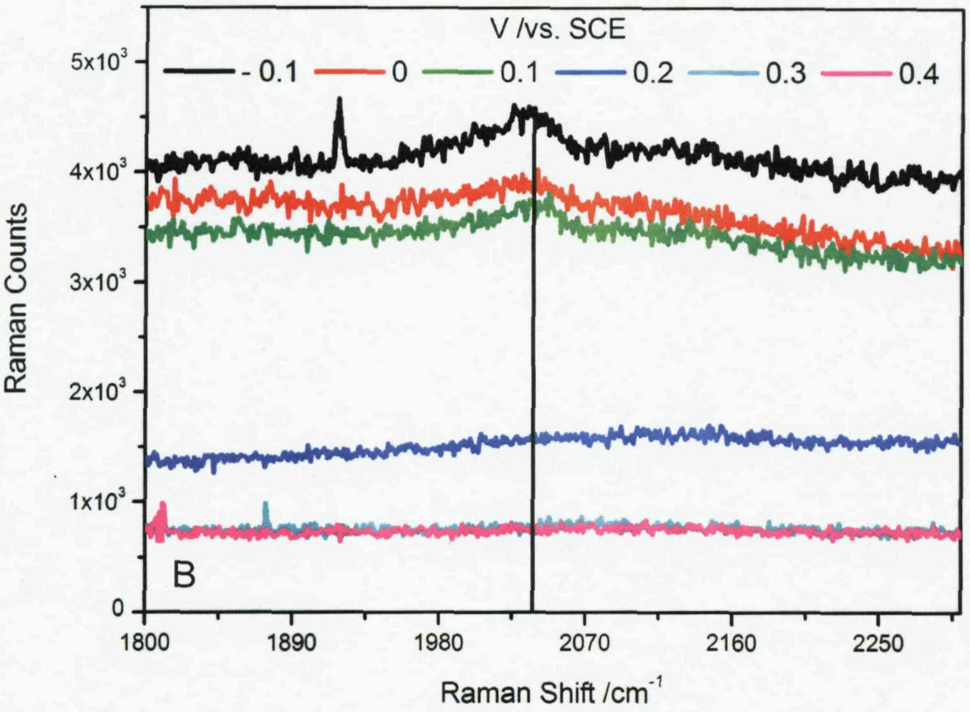

Figure 9 **Potential dependent SER spectra of Carbon Monoxide adsorbed onto a nanostructured Pt 600 nm ¾ *d* electrode in 1 M H_2SO_4 that was saturated with CO. The spectra were acquired using a long working distance x50 objective on a Renishaw Raman 2000 system with 633 nm excitation. Each spectrum was acquired using a single 60 s extended scan.**

The peak positions of CO on Pt are consistent with those seen in the literature [47, 48]. There were two key regions within the extended scan that were of interest the bands at ~ 400 and 490 cm^{-1} (Figure 8) which correspond to the Pt - C bond, and ~ 2040 cm^{-1} (Figure 9) which corresponds to the C≡O bond. The presence of both peaks in the Pt – C region indicates that the CO is bound to the Pt surface both terminally (to one Pt) and at bridging sites (2 Pt atoms) sites [38].

There is a shift in the peak positions from 485 and 397 cm^{-1} at -0.1 V to 493 and 404 cm^{-1} at 0.3 V vs. SCE, respectively. There is also a shift in the peak position of the C≡O between these the potentials of -0.1 V and 0.2 V, from 2030.4 to 2036.4 cm^{-1} respectively, the signal from C≡O disappeared after this potential, as observed in Figure 9. The positive shift in wavenumber with increasing potential, for both bands, is consistent with literature and has been attributed to both the weakening of the bond between the platinum and the carbon monoxide, and more importantly to the electrochemical Stark effect [37, 49].

From Figure's 8 & 9 it can be seen that the C≡O band is lower in intensity than that of the Pt – C band, which is in contrast to that observed in the IR spectra and previously reported SERS spectra in the literature. The reason for this can be explained by examining the reflectance spectra from the sample, shown in Figure 10.

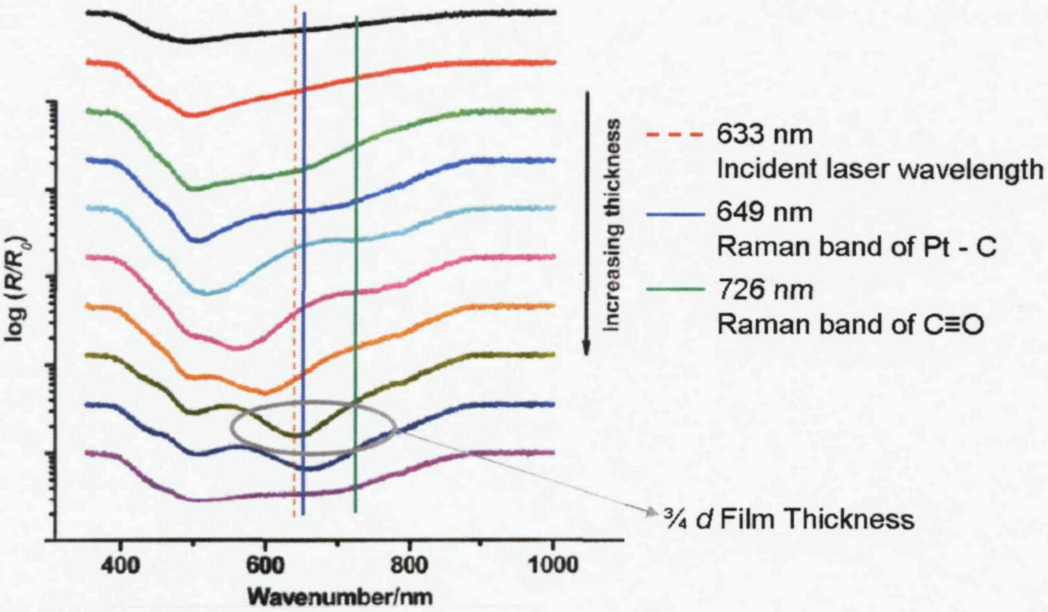

Figure 10 **Reflectance spectrum of a 600 nm Pt sculpted SERS substrate with increasing film thickness. The red dotted line corresponds to the energy of the incident laser, and the blue and green solid lines correspond to the out going Raman bands of the Pt – C and C≡O bonds respectively. The grey circle indicates the reflection spectrum observed at ¾ *d* film thickness.**

The reflection spectra shown in Figure 10are from a fully graded sample [25]. At ¾ *d* film thickness, the thickness used to acquire the CO spectra, there is a plasmon mode that encompasses the in-coming laser wavelength at 633 nm. It also overlaps well with the out- going Raman band for the Pt – C bond (due to tha shift in both bands a Raman shift of 450 cm^{-1} was used) as indicated by the blue line, whereas the band for C≡O (the green line) is not. This accounts for the variations between the signals seen for CO.

The results from this initial study have shown that the plasmon resonance modes from platinum sculpted surfaces can be applied to monitor the Pt – adsorbate bonds. Work has also been done on the development of palladium structures which could also be used for catalytic applications [25].

4 Conclusions.

The studies introduced in this chapter have shown that the sculpted SERS substrates can be used as electrodes for *in situ* studies. The electrodes do not suffer from irreversible loss of signal at extreme potentials, due to the controlled way that the surfaces are produced, and the SERS signal from pyridine returned after the electrode was rewet.

This chapter has also introduced the development of Pt sculpted surfaces. The SERS spectra obtained from a monolayer of CO was consistent with the literature, and the shift in the peak positions were observed, which have been attributed to the weakening of the Pt – C bond and the electrochemical Stark effect. Differences in the intensities of Raman peaks were seen from C≡O and the Pt – C bonds. This was due to the methods of enhancement, which corresponds well to that seen on gold substrates – the largest enhancement is seen when the in-coming laser excitation and the out-going Raman band both overlap well with a plasmon mode of the substrate.

Using the sculpted SERS substrates as electrodes for in situ experiments opens up many avenues of research for the future. Sculpted surfaces can easily be produced from metals such as Pt, Pd, Ni, Rh and others, even alloys, may follow which allows the monitoring of catalytic reactions using SERS. The substrates are predicted to be as robust in other metals as they are in gold, which would make them ideal electrodes for future studies.

5 References

1. Kneipp, K., H. Kneipp, I. Itzkan, R.R. Dasari, and M.S. Feld, Chemical Physics, 1999. **247**(1): p. 155-162.
2. Kneipp, K., H. Kneipp, R. Manoharan, I. Itzkan, R.R. Dasari, and M.S. Feld, Bioimaging, 1998. **6**(2): p. 104-110.
3. Stuart, D.A., J.M. Yuen, N.S.O. Lyandres, C.R. Yonzon, M.R. Glucksberg, J.T. Walsh, and R.P. Van Duyne, Analytical Chemistry, 2006. **78**(20): p. 7211-7215.
4. Cunningham, D., R.E. Littleford, W.E. Smith, P.J. Lundahl, I. Khan, D.W. McComb, D. Graham, and N. Laforest, Faraday Discussions, 2006. **132**: p. 135-145.
5. Smith, W.E., K. Faulds, and D. Graham, Surface-Enhanced Raman Scattering: Physics and Applications, 2006. **103**: p. 381-396.
6. Faulds, K., W.E. Smith, and D. Graham, Analyst, 2005. **130**(8): p. 1125-1131.
7. Faulds, K., W.E. Smith, D. Graham, and R.J. Lacey, Analyst, 2002. **127**(2): p. 282-286.
8. Fleischmann, M., P.J. Hendra, and A.J. McQuillan, Chem. Phys. Lett., 1974. **26**(2): p. 163-166.
9. Gersten, J. and A. Nitzan, *Electromagnetic theory of enhanced Raman scattering by moleculkes adsorbed on rough surfaces.* J. Chem. Phys., 1980. **73**: p. 3023-3037.
10. Murray, C.A. and D.L. Allara, *Measurement of the molecule-Ag separation dependence of SERS.* J. Chem. Phys., 1982. **76**: p. 1290-1303.
11. Dick, L.A., A.D. McFarland, C.L. Haynes, and R.P. Van Duyne, J. Phys. Chem. B, 2002. **1006**: p. 853.
12. Tian, Z.-Q., B. Ren, and D.-Y. Wu, *SERS: from noble to transition metals and rough surfaces to ordered nanostructures.* J. Phys. Chem. B, 2002. **106**: p. 9463.
13. Zhong, Q.L., X.C. Wang, L. Zhang, X.H. Zhang, J. Xiang, B. Ren, and Z.Q. Tian, Acta Chimica Sinica, 2003. **61**(12): p. 1960-1964.

14. Tian, Z.-Q., B. Ren, and B.W. Mao, *Extending surface Raman spectroscopy to tramsition metal surfaces for practical applications. 1. Vibrational properties of thiocyanate and CO adsorbed on electrochemically activated Pt surfaces.* J. Phys. Chem. B, 1997. **101**: p. 1338.

15. Cao, P.G., J.L. Yao, B. Ren, R.A. Gu, and Z.Q. Tian, J. Phys. Chem. B, 2002. **106**(7283).

16. Zou, S. and M.J. Weaver, *Potential-dependant metal-adsorbate stretching frequencies for CO on transition-metal electrodes, chemical bonding versus electrostatic field effects.* J. Phys. Chem., 1996. **100**: p. 4237.

17. Jeanmaire, D.L. and R.P. Vanduyne, J. Electroanal. Chem., 1977. **84**(1): p. 1-20.

18. Yang, X.M., D.A. Ajito, D.A. Tryk, K. Hashimoto, and A. Fujishiima, J. Phys. Chem, 1996. **100**: p. 117.

19. Brolo, A.G., D.E. Irish, and J. Lipkowski, J. Phys. Chem. B, 1997. **101**: p. 3906.

20. Yamada, H. and Y. Yamamoto, Chem. Phys. Lett, 1981. **77**: p. 520.

21. Bartlett, P.N., J.J. Baumberg, P.R. Birkin, M.A. Ghanem, and M.C. Netti, Chem. Mater, 2002. **14**: p. 2199.

22. Bartlett, P.N., P.R. Birkin, and M.A. Ghanem, Chem. Commun., 2000: p. 1671.

23. Bartlett, P.N., P.R. Birkin, M.A. Ghanem, and C.S. Toh, J. Mater. Chem., 2001. **11**: p. 849.

24. Bartlett, P.N., T. Dunford, and M.A. Ghanem, J. Mater. Chem., 2002. **12**: p. 3130.

25. Abdelsalam, M.E., S. Mahajan, P.N. Bartlett, J.J. Baumberg, and A.E. Russell, Journal of the American Chemical Society, 2007. **129**(23): p. 7399-7406.

26. Eischens, R.P. and W.A. Pliskin, Advan. Catalysis., 1958. **10**: p. 1.

27. Eischens, R.P., S.A. Francis, and W.A. Pliskin, J. Phys. Chem, 1956. **60**: p. 194.

28. O'Neill, C.E. and D.J.C. Yates, ibid, 1961. **65**: p. 901.

29. Garland, C.W., ibid, 1959. **63**: p. 1423.

30. Beden, B., C. Lamy, A. Bewick, and J. Kumimatsu, Electronal. Chem., 1982. **121**: p. 343.
31. Beden, B., A. Bewick, and C. Lamy, J. Electroanal. Chem, 1983. **148**: p. 147.
32. Kumimatsu, J., J. Electrochem. Comm., 1983. **145**: p. 219.
33. Kumimatsu, K., H. Seki, W.G. Golden, J.G. Gordon II, and M.R. Philpott, Surf. Sci., 1985. **158**: p. 596.
34. Kumimatsu, K., K. Shimazu, and H. Kita, J. Electroanal. Chem, 1988. **256**: p. 371.
35. Ashley, K. and S. Pons, Chem. Rev., 1988. **88**: p. 673.
36. Weaver, M.J., Appl. Surf. Sci., 1993. **67**: p. 147.
37. Lambert, D.K., Electrochimica Acta., 1996. **41**(5): p. 623.
38. Leung, L.W.H. and M.J. Weaver, J. Am. Chem. Soc., 1987. **109**: p. 5113.
39. Zou, S.Z., and M.J. Weaver, J. Anal. Chem., 1998. **70**: p. 2387.
40. Cao, P.G., J.L. Yao, B. Ren, R.A. Gu, and Z.Q. Tian, Chem. Phys. Lett, 2000. **316**: p. 1.
41. Tian, Z.Q., B. Ren, and D.Y. Wu, J. Phys. Chem. B, 2002. **106**: p. 9463.
42. Liu, Z., Z.L. Yang, L. Cui, B. Ren, and Z.Q. Tian, Journal of Physical Chemistry C, 2007. **111**(4): p. 1770-1775.
43. Tian, N., Z.Y. Zhou, S.G. Sun, L. Cui, B. Ren, and Z.Q. Tian, Chemical Communications, 2006(39): p. 4090-4092.
44. Lu, L., G. Sun, H. Zhang, H. Wang, S. Xi, J. Hu, Z.Q. Tian, and R. Chen, J. Mat. Chem., 2004. **14**: p. 1005.
45. Hu, J., Y. Zhang, J.F. Li, Z. Liu, B. Ren, G. Sun, Z.Q. Tian, and T. Lian, Chem. Phys. Lett, 2005. **408**: p. 354.
46. Tian, Z.Q., B. Ren, and D.Y. Wu, J. Phys. Chem. B, 2002. **106**(37): p. 9463.
47. Ren, B., G.K. Liu, X.B. Lian, Z.L. Yang, and Z.Q. Tian, Analytical and Bioanalytical Chemistry, 2007. **388**(1): p. 29-45.
48. Li, J.F., Z.L. Yang, B. Ren, G.K. Liu, P.P. Fang, Y.X. Jiang, D.Y. Wu, and Z.Q. Tian, Langmuir, 2006. **22**(25): p. 10372-10379.
49. Leung, L.W.H., A. Wieckowski, and M.J. Weaver, J. Phys. Chem, 1988. **92**(24): p. 6985.

Chapter Seven: Conclusions and Future Work

1 Conclusions.

The overall aim of this thesis was to understand the sculpted SERS substrates that have been developed over the last three years, and to facilitate a deeper understanding of how they increased Raman signals. Also, to demonstrate the unique properties of the substrates and how they could be used in the future. To achieve this aim a series of samples were produced with varying void diameter and film thickness, and the SERS signals of benzene thiol obtained, with three different excitation laser wavelengths. The optical properties have also been studied, in parallel to this project, by colleagues in the School of Physics. This has led to a thorough understanding of the plasmon modes occurring at the surfaces, and the modes have been modelled on molecular orbitals.

The results shown in Chapter 4 showed that strong SERS signals were obtained with enhancement factors of 10^8 being achieved with 633 nm excitation. However, the signals varied dramatically with varying surface morphology and incident laser wavelength, showing that one surface geometry was not the optimum substrate across multiple wavelengths. It was seen that there was a correlation between positions of strong SERS signals and the plasmon modes, especially when the in - coming laser excitation and out-going Raman signals both overlapped well with a plasmon mode of the substrate. It was also seen that the plasmon mode that is based upon a *P* orbital consistently gave rise to strong SERS signals, especially within the 350 nm void surface, the $^1P_+$ which is the 'bonding' type of plasmon mode gave rise to the largest signals. This mode is centred at the rim of the substrate, and the smaller rim of the 350 nm sample gives rise to a stronger electric field across the void, hence showing larger SERS signals.

The substrate properties were discussed in Chapter 5, and it was shown that the substrate is unique in terms of reproducibility and robustness. The reproducibility is 10% on the same sample and 13% between samples [1]. The variation arises from slight imperfections on the substrate, as well as some variation when multiple or single voids were sampled (Chapter 5). The substrates can also be used more than once, simply by electrochemically stripping the molecule from the surface, and then re-adsorbing a molecule on the clean surface. The substrates also perform for longer than any other substrate with a shelf life of more than 3 years.

Chapter 5 also discussed the origins of the background seen on every SERS spectrum. It was widely been attributed to a photoluminescence from the metal surface. When the shapes of the different backgrounds from 4 different laser wavelengths were plotted versus eV, it was clear that the highest background corresponded to the plasmon modes at that point of the surface. The photoluminescence of gold surfaces have been shown to correlate with surface plasmon polaritons, and photoluminescence emission spectroscopy is used to study plasmons [2-4]. Therefore, the background can be attributed to a photoluminescent emission from the gold. However, further work is required to monitor how the background changes when different electron withdrawing/donating adsorbates are used, and also how it varies with potential in an electrochemical environment.

Although this thesis has demonstrated an understanding of how the sculpted SERS substrates work the applications of the substrates is an area that needs further work. Chapter 6 demonstrated how the substrates make ideal electrodes for the study of electrochemical reactions, as they can be used at more extreme potentials without suffering from irreversible loss of signal. The unique way that the surfaces can be tuned for a given molecular vibration could also lead to many avenues of further work.

2 Further Work

There are two main directions that this project could progress: Firstly to develop a deeper understanding of how the substrates work i.e. whether the voids must be interconnected. Secondly, further applications of the substrates.

2.1 Deeper understanding of substrates.

A preliminary experiment was done to try and isolate the cavities of the structure by preparing a double templated substrate. This involved preparing a 900 nm template, and electrodepositing gold up to 0.25 *d*. The spheres were then dissolved and the structured surface was used to assemble 600 nm spheres. The smaller spheres sat in the dishes created by the larger spheres, and gold was then electrodeposited around the smaller spheres, creating isolated voids. The voids were located using Renishaw's SEM-SCA and spectra of 10 mM BT was acquired using 785 nm excitation. The result is shown in Figure 1.

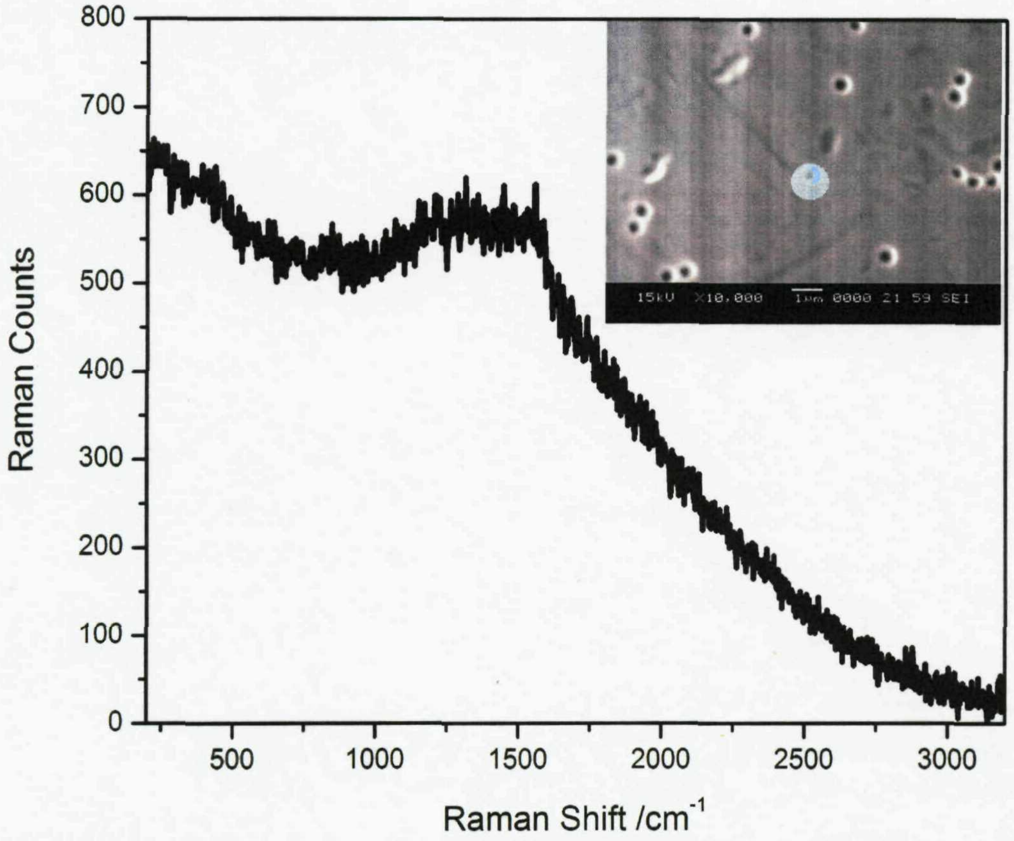

Figure 1 **Spectra obtained from a single gold void, indicated in the SEM image. The spectrum was acquired using 785 nm excitation at < 1 mW power with 4 x 10 s accumulations. The scan range was 3200 to 200 cm^{-1}, and the point at which the laser was focused is indicated by the blue spot on the SEM image.**

It was seen that very little SERS signal was acquired from a single void, which implies that the substrate must have interconnected voids to yield a good SERS signal; however, further work is required to optimise the preparation of such substrates.

Another way to isolate plasmon modes was to prepare structures which essentially blocked the plasmon modes within the void or on the surface of the void. This was done by preparing a gold substrate as normal, and electrodepositing a 100 nm layer of nickel over the top surface before removing the spheres. Then the opposite structure was also prepared which had a gold top surface. However, there were problems getting an even film over the top surface, but the technique could be promising if this avenue of research was taken further.

2.2 Further applications of the substrates

As shown in Chapter 6 the sculpted substrates make ideal electrodes, which enable us to monitor electrochemical reactions with SERS, and an example of detecting the Pt – C bond in CO on Pt SERS substrates was shown. However, there are numerous other areas of research that could utilise this technique in the future.

The area of electrocatalysis requires the metal – adsorbate bond to be measured as it is fundamental to the performance of the metal as a catalyst. However, no *in situ* spectroscopic technique has been able to detect the bonds, due to several imiting factirs: the interference of water in the IR spectra, the low energy bands at $< 1000\ \text{cm}^{-1}$ are inherently difficult to detect simultaneously with the mid IR. However, SERS overcomes this problem, and it is possible to detect the metal-adsorbate bond using Pt sculpted SERS substrates. Further work could extend to the detection of oxidation of alcohols in acidic and alkaline solutions, as well as the hydrogen and oxidation reactions at the metal surfaces. Also, the technique is not limited to Pt, we have already shown that Pd surfaces can also be used for SERS [5], and future development could yield Pt alloys, which have yet to be used as SERS substrates.

The substrates are not simply limited to electrochemical cells, there is also potential to utilise the plasmon modes that are localised in the centre of the void, which have yet to be fully utilised thus far. An initial experiment was performed using a custom made heating/gas cell, described in Chapter 2. The substrate was placed into the cell which was sealed and then filled with nitrogen. Spectra were collected from the substrate and from flat gold and the results are shown in Figure 2.

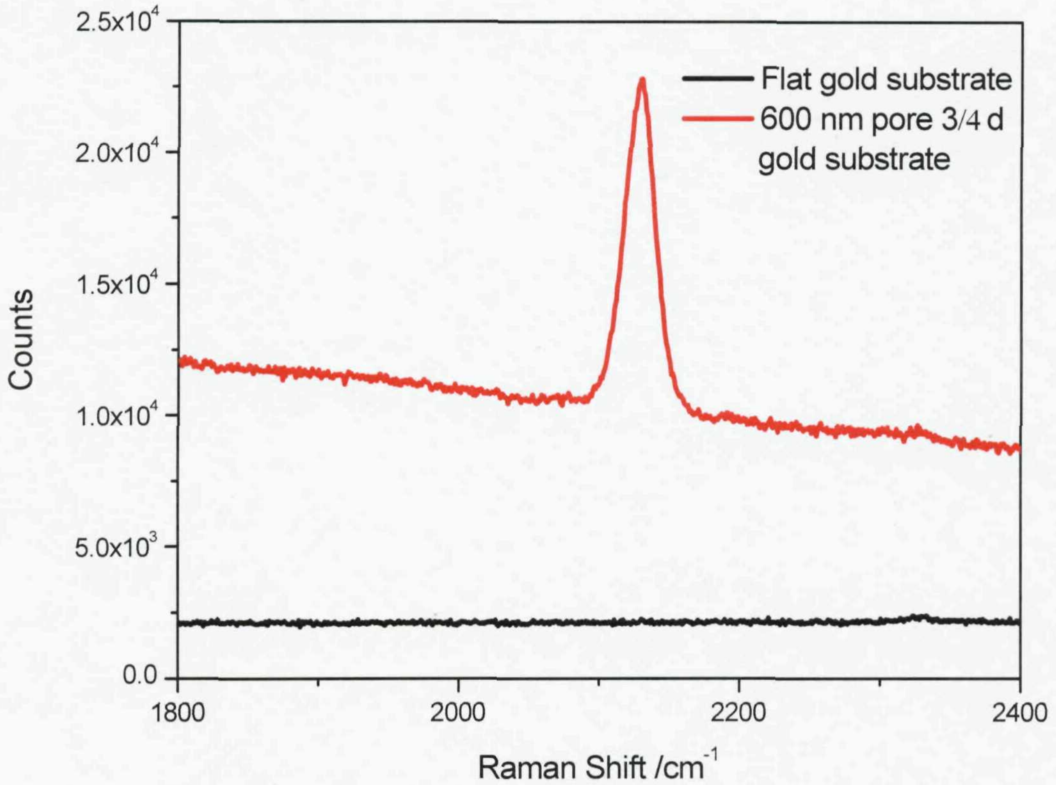

Figure 2 **SERS spectra of 4 atm N2, using a 600 nm ¾ d gold sculpted substrate (red line), in comparison to no pressure of gas (black line). Each spectrum was obtained using 5 x 60 s static scans, using 633 nm excitation.**

There was a clear enhancement of the Raman spectra of the gas from the nanostructured substrate, in comparison to the flat gold. This enhancement was also seen to change with pressure of nitrogen, as shown in Figure 3

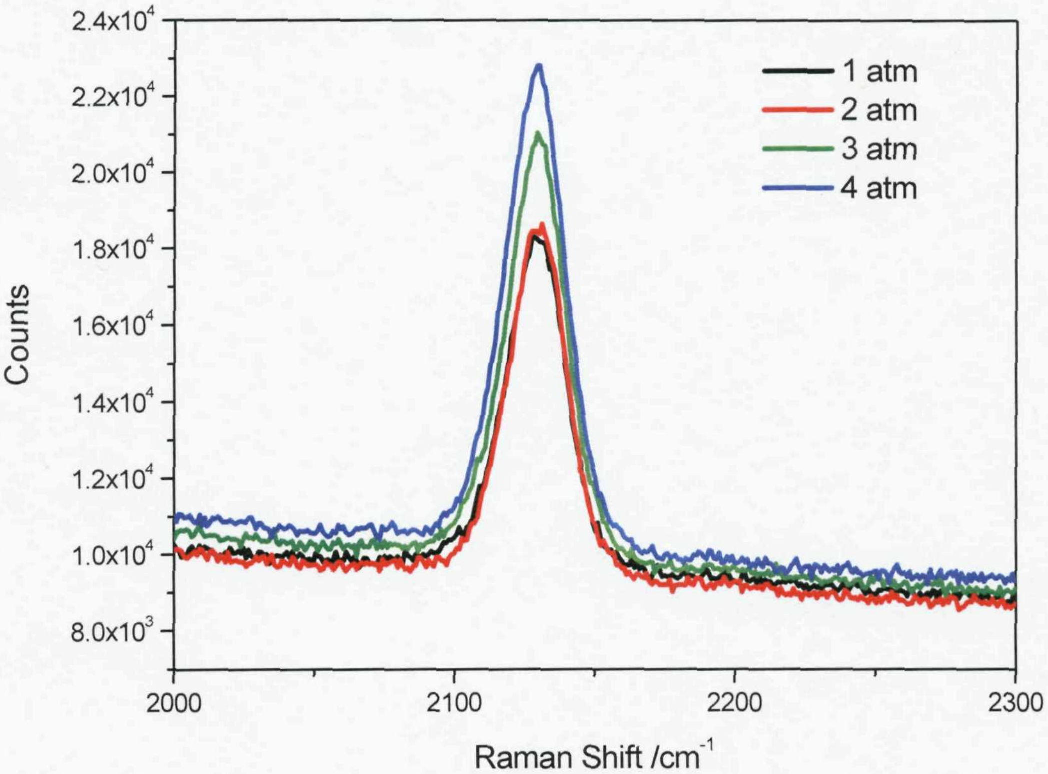

Figure 3 **SERS spectra of a gaseous species upon a 600 nm ¾ d substrate. Each spectrum was acquired using 5 x 60 s static scans with 633 nm excitation.**

Upon examination of the band position of the peak, it was discovered that the band was seen at ~ 2130 cm^{-1}, whereas the expected band for the nitrogen stretch is seen at 2300 cm^{-1}. Therefore it was concluded that the peak was not due to nitrogen, but rather to some impurities that could be in the gas line. However, this result does show that the plasmon mode that is centered in the dish (*D* modes, discussed in Chapter 3 & 4) can also be utilized in further SERS studies.

3 References

1. Cintra, S., M.E. Abdelsalam, P.N. Bartlett, J.J. Baumberg, T.A. Kelf, Y. Sugawara, and A.E. Russell. Faraday Discussions, 2006. **132**: p. 191-199.
2. Burgess, D.S. Nanophotonics, 2006. **March**.
3. Girlando, A., W. Knoll, and M.R. Philpott. Solid State Communications, 1981. **38**(10): p. 895-898.
4. Bouhelier, A., R. Bachelot, G. Lerondel, S. Kostcheev, P. Royer, and G.P. Wiederrecht. Phys. Rev. Lett., 2005. **95**: p. 267405.
5. Abdelsalam, M.E., S. Mahajan, P.N. Bartlett, J.J. Baumberg, and A.E. Russell. Journal of the American Chemical Society, 2007. **129**(23): p. 7399-7406.